Durability of Ceramic Matrix Composites at Elevated Temperatures: Experimental Studies and Predictive Modeling

by

Howard G. Halverson

Dissertation submitted to the Faculty of the

Virginia Polytechnic Institute and State University

in partial fulfillment for the requirements of the degree of

Doctor of Philosophy

in

Engineering Mechanics

W.A. Curtin, Chair

K. L. Reifsnider

J. J. Lesko

S. L. Kampe

L. G. Kraige

May 8, 2000

Blacksburg, Virginia

Keywords: Ceramic Matrix Composite, Stress-Rupture, Micromechanics, Creep, High Temperature

Durability of Ceramic Matrix Composites at High Temperatures:

Experimental Studies and Predictive Modeling

by

Howard G. Halverson

(ABSTRACT)

In this work, the deformation and strength of an oxide/oxide ceramic matrix composite system under stress-rupture conditions were studied both experimentally and analytically. A rupture model for unidirectional composites which incorporates fiber strength statistics, fiber degradation, and matrix damage was derived. The model is based on a micromechanical analysis of the stress state in a fiber near a matrix crack and includes the effects of fiber pullout and global load sharing from broken to unbroken fibers. The parameters required to produce the deformation and lifetime predictions can all be obtained independently of stress-rupture testing through quasi-static tension tests and tests on the individual composite constituents. Thus the model is truly predictive in nature. The predictions from the model were compared to the results of an extensive experimental program. The model captures the trends in steady-state creep and tertiary creep but the lifetime predictions are extremely conservative. The model was further extended to the behavior of cross-ply or woven materials through the use of numeric representations of the fiber stresses as the fibers bridge matrix cracks. Comparison to experiments on woven materials demonstrated the relationship between the behavior of the unidirectional and cross-ply geometries. Finally, an empirical method for predicting the durability of materials which exhibit multiple damage modes is examined and compared to results of accurate Monte Carlo simulations. Such an empirical method is necessary for the durability analysis of large structural members with varying stress and temperature fields over individual components. These analyses typically require the use

of finite element methods, but the extensive computations required in micromechanical models render them impractical. The simple method examined in this work, however, is shown to have applicability only over a narrow range of material properties.

Acknowledgements

- My advisor, Dr. Bill Curtin, for helping me through many of the subtleties of the behavior of ceramic matrix composites and for supporting me financially and professionally for so many years.
- Dr. Ken Reifsnider and Dr. Jack Lesko, for serving on my committee and for much advice through the years. These two always had a word of encouragement for me, no matter how unhappy I was with my results.
- Dr. Glenn Kraige and Dr. Steve Kampe for taking time out of their busy schedules and serving on my committee.
- Dr. Scott Case for so many things I've lost count. He was always willing to listen to me rant and rave about CMCs, testing, simulations, or whatever else had me up in arms and for that I am especially thankful.
- Shelia Collins, Bev Williams, Paula Lee, and Melba Morrozoff. Somehow, no matter how often I waited until the last minute, these people always managed to save me and keep everything running smoothly.
- The people who have shared the lab in 102 Norris with me over the past six years: Sneha Patel, Nikhil Verghese, Dave Haeberle, Michael Hayes, Art Callaham, Kyle Garcia, Rich Plunkett, Mehran Elahi, Kin Liao, and Jen Elmore. We had a lot of fun over the years, and I think a few of us even managed to get some work done while we weren't paying attention.
- The rest of the MRG students for all their help, advice, and suggestions.
- My parents, Howard and Evelyn. Now they can ask "Are you looking for a job?" instead of "Are you writing your dissertation?"
- Dr. Martha Jaskowiak at NASA Glenn Research Center, Rich Goettler at McDermott and Dave Stinton at Oak Ridge for providing financial support.

Table of Contents

(ABSTRACT) ii
Acknowledgements iv
Table of Contents v
List of Figures viii
List of Tables xiii
Nomenclature xiv
Chapter 1 Introduction 1
Chapter 2 Literature Review 4
2.1 Tensile Damage Mechanisms and Models 4
2.2 Time-Dependent Mechanisms and Models 13
2.3 Properties of Nextel 610 Fibers and Composites 18
2.3.1 Strength Properties 18
2.3.2 Creep Properties 20
2.3.3 Composite Properties 22
Chapter 3 Composite Stress-Rupture Modeling 27
3.1 Fiber Behavior 27
3.1.1 Fiber Tensile Behavior 27
3.1.2 Fiber Time-Dependent Behavior 37
3.2 Composite Behavior 41
3.2.1 Tensile Strength 41
3.2.2 Time-Dependent Strength 44
Chapter 4 Experimental Methods 54
4.1 Material System 54
4.2 Mechanical Testing 56
4.2.1 Quasi-Static Testing 56
4.2.2 Hysteresis Loop Testing 59
4.2.3 Stress-Rupture Testing 59

4.3 Microscopy 60
Chapter 5 Experimental Results and Discussion 62
5.1 As-Received Specimens 62
5.1.1 Fiber Volume Fraction and Matrix Porosity 62
5.1.2 Matrix Cracking 66
5.2 Quasi-Static Tension Tests and Discussion 69
5.2.1 Quasi-Static Tension Test Results 69
5.2.2 Hysteresis Loop Testing 77
5.2.3 Discussion of Quasi-Static Experiments 78
5.3 Time-Dependent Testing 87
5.3.1 Stress-Rupture Testing 87
5.3.2 Residual Strength Testing 93
5.3.3 Discussion of Stress-Rupture testing 95
5.4 Application of the Stress-Rupture Methodology 97
5.4.1 Steady-State Creep Rate 98
5.4.2 Stress-Rupture Lifetime 100
5.4.3 Tertiary Creep 105
5.4.4 Residual Strength 106
5.4.5 Summary of Comparisons of Model and Experiment 108
Chapter 6 Woven and Crossply Composites 109
6.1 Approach 109
6.2 Growth of Cracks in Crossply/Woven materials 113
6.3 Modeling of ‘Through’ Cracking 120
6.4 Summary 124
Chapter 7 Combining Damage Mechanisms 127
7.1 Fiber Creep as a Damage Mechanism 127
7.2 Simulations and Analysis 128
7.3 Summary 137
Chapter 8 Conclusions and Future Work 139

8.1 Conclusions 139
8.1.1 Stress-Rupture Modeling 139
8.1.2 Woven and Cross-ply Composites 140
8.1.3 Analytic Representations of Stress-Rupture Under Combined Damage Mechanisms 140
8.2 Questions Raised and Future Work 141
8.2.1 Stress-Rupture Modeling 141
8.2.2 Woven and Cross-ply Composites 142
8.2.3 Analytic Representations of Stress-Rupture Under Combined Damage Mechanisms 142
References 143
Vita 151

List of Figures

Figure 1. The strength of continuous fiber ceramic composites as compared to traditional materials [1] 2
Figure 2. Crack deflection vs. crack penetration criteria [4] 5
Figure 3. Stress transfer at the fiber/matrix interface 6
Figure 4. Matrix crack progression in a SiC/CAS composite 12
Figure 5. Deformation mechanism map for 32 μm grain size silver [30] 14
Figure 6. Nextel 610 fiber strength retention at elevated temperatures [47] 21
Figure 7. Stress-rupture of Nextel 610 fibers [49] 21
Figure 8. Larson-Miller plot of alumina fibers [50] 22
Figure 9. Four-point flexural strength of Nextel 610/alumina composites [52] 23
Figure 10. Strength of Nextel 610/DIMOX Al_2O_3 composites After aging a) 10 hours, b) 100 hours [53] 24
Figure 11. Stress-strain curves for GEN IV composite 25
Figure 12. Stress-rupture lifetime of GEN IV composite 25
Figure 13. Creep deformation of GEN IV composite 26
Figure 14. Fiber stress as a function of distance away from a matrix crack 31
Figure 15. Probability of fiber failure as a function of matrix modulus at an applied stress of $\tilde{T} = 1$ 34
Figure 16. Average failure location for a single fiber as a function of matrix contribution 35
Figure 17. Fiber stress profile when two matrix cracks interact 36
Figure 18. Probability of failure as a function of crack spacing 36
Figure 19. Probability of failure of a fiber under a constant load 39
Figure 20. Effect of matrix modulus on fiber lifetime 40
Figure 21. Effect of Weibull modulus, *m*, on composite lifetime ($\beta = 5$, $\alpha = 1$) 48
Figure 22. Effect of β on composite lifetime ($m = 5$, $\alpha = 1$) 48
Figure 23. Effect of α on composite lifetime ($m = 5$, $\beta = 5$) 49

Figure 24. Effect of α on composite lifetime (m = 5, β = 5) 49
Figure 25. Effect of crack spacing on composite lifetime (m = 5, β = 5) 50
Figure 26. Change in fiber far-field stress due to creep deformation 52
Figure 27: High temperature oven used for experimental study 57
Figure 28. Specimen 23-4 cross section for fiber volume fraction measurement 63
Figure 29. Poor fiber distribution in specimen cross-section 63
Figure 30. Microstructure of the woven materials 66
Figure 31. Schematic of a woven composite [66] 67
Figure 32. Surface of a virgin unidirectional specimen 67
Figure 33. Initial matrix damage for a specimen with 29% fiber volume fraction 68
Figure 34. Longitudinal matrix cracking in virgin specimen 68
Figure 35. Crack patterns in a virgin woven specimen 69
Figure 36. Sample unidirectional stress-strain curves 70
Figure 37. Sample stress-strain curves for woven specimens 70
Figure 38. Tensile modulus as a function of temperature 71
Figure 39. Tensile failure strain as a function of temperature 72
Figure 40. Tensile strength as a function of temperature 72
Figure 41. Fracture surfaces of room temperature quasi-static specimens 73
Figure 42. Fracture surfaces of elevated temperature quasi-static specimens (1093°C) ... 74
Figure 43. Fracture surface of specimen tested at room temperature 74
Figure 44. Fracture surface of a woven specimen tested in quasi-static tension at 1093°C. 75
Figure 45. Fiber fracture surfaces for a specimen tested in quasi-static tension 75
Figure 46. Matrix damage under room temperature quasi-static loading 76
Figure 47. Matrix damage under 950°C quasi-static test 76
Figure 48. Cracking in a woven specimen which demonstrates fiber failure in the plane of the crack. 77
Figure 49. Hysteresis loop testing 78

Figure 50. Stress-strain curves at 1093°C for specimens with varying fiber volume fractions 81
Figure 51. Effect of fiber volume fraction on elastic modulus at 1093°C 82
Figure 52. Inverse tangent modulus plot at room temperature 84
Figure 53. CAT model compared to room temperature data (σ_c = 167 ksi) 85
Figure 54. CAT model compared to experimental data at 1093°C (σ_c = 139 ksi) 86
Figure 55. Stress-rupture testing for 50% fiber volume fraction specimens 88
Figure 56. Strain rates during two stress rupture tests at 1050°C 88
Figure 57. Steady-state strain rate during stress-rupture 89
Figure 58. Failure strain in stress-rupture 89
Figure 59. Stress-rupture behavior at 1093°C 90
Figure 60. Steady-state strain rate at 1093°C 90
Figure 61. Fracture surfaces of specimens tested in stress rupture at 1093°C 91
Figure 62. Fracture surface of specimen tested in stress-rupture at 950°C 91
Figure 63. Matrix damage in stress-rupture at 950°C 92
Figure 64. Matrix damage in stress-rupture at 1050°C 92
Figure 65. Fiber fracture surfaces in stress-rupture at 950°C 92
Figure 66. Fiber fracture surface under stress-rupture at 1093°C 93
Figure 67. Residual strength testing at 1050°C and 25 ksi applied stress 94
Figure 68. Modulus change due to stress-rupture testing 94
Figure 69. Larson-Miller plot of fibers compared to experimental composite data 96
Figure 70. Composite Monkman-Grant plot compared to fiber data. Fiber data from Reference [71]. 97
Figure 71. Strain rates found by setting α = 0.75 99
Figure 72. Initial strain rates in stress-rupture compared to predictions based on quasi-static properties 99
Figure 73. Comparison of experimental data to fitted behavior 100
Figure 74. Comparison between model and experiment 102
Figure 75. Effect of annealing on stress-rupture lifetime of Nextel 610 fiber [72] 104

Figure 76. Effect of altering normalized timescale on the comparison between model and experiment 105
Figure 77. Fiber stress as a function of time 106
Figure 78. Comparison of composite creep rate with experimental data 107
Figure 79. Predicted and measured residual strength values 107
Figure 80. Schematic of bridged cracks 110
Figure 81. Predicted matrix cracking stress as a function of initial crack length in the unidirectional oxide/oxide materials 113
Figure 82. Multi-planar fracture in SiC/SiC composite [79] 114
Figure 83. Crack penetration into 0° ply 115
Figure 84. Critical stress required for crack advance from 0° ply into 90° ply for SiC/SiC materials 116
Figure 85. Schematic of analysis of crack growth 117
Figure 86. Crack penetration into 90° ply under stress-rupture conditions 118
Figure 87. Crack penetration into 0° ply under stress-rupture conditions 119
Figure 88. Fiber damage across 0° tow in stress-rupture 119
Figure 89. Crack shape of a crack penetrating through many 0° and 90° plies 121
Figure 90. Critical stress required for crack advance as a function of crack size in a crossply composite 122
Figure 91. Stress as a function of position in 0° ply 122
Figure 92. Stress concentration at 0°/90° ply interface 123
Figure 93. Rupture life for unidirectional composites at 1093°C 125
Figure 94. Stress-rupture of the woven materials derived from the behavior of the unidirectional materials 126
Figure 95. Remaining strength for two damage mechanisms at two stress levels. 130
Figure 96. Sequence effects in stress-rupture 132
Figure 97. Wear-out model for combined damage mechanisms at constant stress level 134
Figure 98. Wear-out model for combined damage mechanisms with sequence effect 134

Figure 99. Accuracy of wear-out model as a function of slow crack growth exponent, β 137
Figure 100. Residual strength from both model and numeric simulation 138

List of Tables

Table I: Properties as Reported by 3M 19
Table II: Weibull Properties at Room Temperature of Nextel Fibers 19
Table III: Weibull Parameters of Nextel 610 Fiber after High Temperature Exposure [42] 20
Table IV : Panel Properties as Reported by MTI 55
Table V: Test Matrix 57
Table VI. Fiber volume fraction from density measurements and optical technique 64
Table VII. Optically measured properties of the woven material 65
Table VIII. Quasi-static tension test results 71
Table IX. Panel specific modulus calculations 80
Table X: Matrix modulus calculated from tension tests 82
Table XI. Fiber stress rupture data 100
Table XII. Parameters used in stress-rupture analysis 101
Table XIII. Parameters used in the analysis of crack growth composites 115
Table XIV. Parameters used for analysis and simulation 129
Table XV. Wear-out model parameters 131
Table XVI. Comparison of wear-out model to Miner's Rule 136
Table XVII. Wear-out model exponent, α, as a function of slow crack growth exponent, β 136

Nomenclature

a	crack size
α	"matrix contribution" parameter
B	matrix creep coefficient
β	exponent in slow crack growth law
C	coefficient in slow crack growth law
c_0	normalizing distance in bridging law
δ	matrix slip length
δ_c	fiber characteristic length
ε	strain
$\dot{\varepsilon}$	strain rate
E_c	composite modulus
E_f	fiber modulus
E_m	matrix modulus
F	Larson-Miller constant
f	fiber volume fraction
γ	exponent in "wear-out" model
η	"bridging stiffness" parameter
K_{Ic}	critical mode I stress intensity factor
l_0	fiber Weibull length
l_s	fiber slip length
$\langle L \rangle$	mean fiber pullout length
$\mathfrak{L}$	inverse tangent modulus
m	fiber Weibull modulus
n	matrix creep exponent
ν	Poisson's ratio
r	fiber radius
σ_{app}	global applied stress
σ_c	fiber characteristic strength
σ_f	fiber stress
σ_i	fiber initial strength
σ_m	matrix stress
σ_0	ACK matrix cracking stress
σ_r	remaining strength
σ_{ult}	composite ultimate strength
p_f	probability of fiber element failure
p_s	probability of fiber element survival
q	probability of fiber failure
Q	Larson-Miller critical value
ρ	damage parameter
τ	interface frictional stress
$\hat{\tau}$	stress rupture lifetime
t	time
T	fiber stress at matrix crack
$\tilde{T}$	fiber stress at matrix crack (normalized)
Y	crack geometric factor
z_0	half-crack spacing

Chapter 1 Introduction

In the competitive modern economy, increases in fuel efficiency can make the difference between profitability and disaster. For many applications, such as heat exchangers and turbine engines, increases in fuel efficiency can be accomplished by increasing the operating temperature. As temperatures increase, the demands on traditional metallic materials soon begin to outstrip their capability. Aware of this, engineers have proposed ceramics as potential replacements for metals.

Ceramics have excellent stiffness-to-weight and strength-to-weight ratios when compared to traditional metals. These attractive properties can also be maintained to extremely high temperatures, which makes them attractive materials for use in engines, power plants, and other similar environments. However, ceramics are brittle materials, which means that even microscopic flaws can greatly reduce the strength of the component and that the resulting failure process involves very little energy. The brittleness of monolithic ceramics has made them unsuitable for many applications.

However, the inherent brittleness of ceramic materials can be overcome by the use of fiber reinforcements. Although the ceramic matrix may still fracture, the reinforcements bridge the cracks keeping the material intact. The fibers can also debond and slide through the matrix, dissipating energy. At the same time, they retain the attractive high temperature properties of ceramics (see Figure 1).

In order to use ceramic matrix composites (CMCs) with confidence, designers and engineers must be able to predict their response to the applied loads and the environment. While the static tensile strength mechanisms of ceramic matrix composites are reasonably well understood, their time-dependent properties, such as creep deformation and strength, are not. As a result, ceramic composites have made only limited inroads in the

commercial market. An important first step in giving designers the confidence to use CMCs is to obtain an understanding of the damage mechanisms that exist in CMCs and their effects on stress-rupture lifetime and deformation.

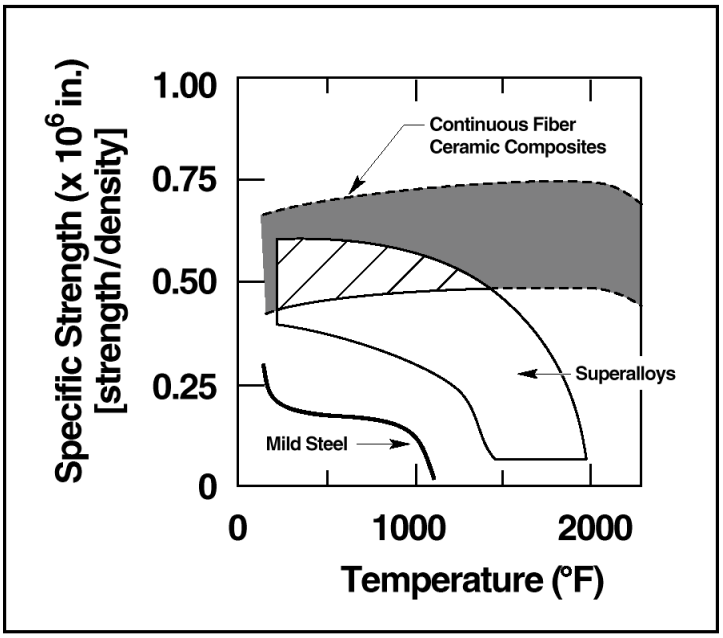

Figure 1. The strength of continuous fiber ceramic composites as compared to traditional materials [1]

In this work, the stress-rupture life, creep deformation, and the associated damage modes for a Nextel 610[1] (99% Alumina) Fiber / Alumina-Yttria Matrix CMC[2] are examined. In addition to the mechanical characterization of properties such as lifetime, stiffness, and deformation, microscopic examination of the tested specimens is conducted. This examination reveals information about the specific damage modes and their progress with time. This system should not be affected by many of the environmental effects (e.g.

[1] 3M Corporation, Minneapolis, Minnesota

[2] Manufactured by McDermott Technologies, Inc. Lynchburg, VA

oxidation) that plague other CMC systems in the air environment, allowing for a more complete examination of other damage modes.

The results are compared to existing models of CMC behavior to ascertain their applicablility and accuracy to the material system. These models are either empirical or concerned with single damage mechanisms and are generally not sufficient for predictions where multiple damage mechanisms are involved.

The ultimate goal is two-fold: firstly to understand the relationships between damage mechanisms which occur during creep and secondly to accurately model the effect of these mechanisms on time-dependent specimen strength and deformation.

The remainder of this dissertation is organized as follows. In the second chapter recent literature regarding the damage mechanisms that exist in CMCs, current life prediction methodologies, and experimental results on similar materials are presented. The analytical procedure proposed for fiber-dominated stress rupture of composites is presented in the third chapter. Detailed information on the experimental techniques used to obtain relevant mechanical data is given in the fourth chapter. The collected data is discussed in the fifth chapter and compared to the predictions of the model. The behavior of crossply material under stress-rupture conditions in the context of the proposed model is discussed in the sixth chapter. A method of accounting for multiple damage mechanisms in fiber-dominated stress rupture is presented in the seventh chapter. The eighth and final chapter is a summary of the important results and proposes new research topics which will extend this work.

Chapter 2 Literature Review

Ceramic composites can be considered as a system of three constituents: fiber, matrix, and the fiber/matrix interface. Each can be damaged and/or fail under quasi-static loading. When time-dependent loads are applied, there are additional damage modes which must be considered. The major damage modes expected to occur in the composite during the experimental effort and previous work on oxide/oxide materials similar to the one tested as part of this research will be discussed in this section.

2.1 Tensile Damage Mechanisms and Models

Consider the unidirectional composite, where fibers run in only one direction, parallel to the applied load. Upon initial loading, the composite exhibits linear elastic behavior, where, on average, the deformations and strains in the fibers and the matrix are equal along the length of the composite. The stress carried by the two constituents and the composite are then given by

$$\frac{\sigma_{fiber}}{E_{fiber}} = \frac{\sigma_{matrix}}{E_{matrix}} = \frac{\sigma_{composite}}{E_{composite}}, \tag{1}$$

where the composite modulus is given by the rule of mixtures,

$$E_{composite} = fE_{fiber} + (1-f)E_{matrix}. \tag{2}$$

Here f is the fiber volume fraction, E is the elastic modulus of the material, and σ is the stress carried by the material. The Poisson's ratios of the fibers and matrix are assumed to be identical.

In most fiber-reinforced CMCs, the strain-to-failure of the fibers is greater than that of the matrix material. Therefore, as the applied load is increased, cracks form in the matrix and rapidly propagate across the cross-section. When the crack approaches an unbroken fiber,

it can either penetrate the fiber, breaking it, or it can be deflected along the fiber/matrix interface. The latter process allows the cracks to pass around the fibers, leaving the fibers bridging the crack and holding the composite together. He and Hutchinson [2] and Ahn et al. [3], have studied the conditions under which the crack is deflected at the interface rather than penetrating the fiber. Ahn et al. found that the elastic properties of the fiber and matrix, the toughness of the interface, and the fiber volume fraction are the most important parameters. The maximum ratio of interface toughness to fiber toughness to ensure crack deflection for a range of fiber volume fractions (Vf in this figure) and values of the first Dundurs' Parameter, α, is shown in Figure 2.

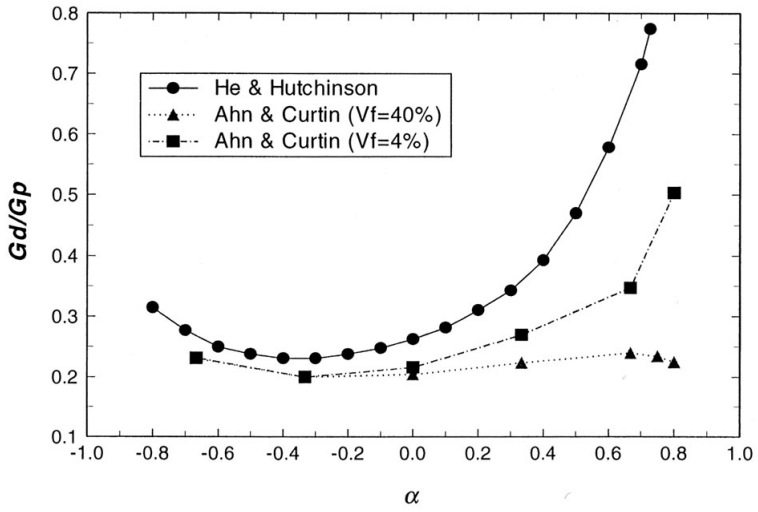

Figure 2. Crack deflection vs. crack penetration criteria [4]

If the matrix does fail and fibers bridge the resulting crack, the stresses carried by the fibers and the matrix are no longer independent of position. At a matrix crack the entire applied load must be carried by the fibers, while away from the crack, stress is transferred back into the matrix via a constant shear stress, τ, as illustrated in Figure 3 for the single fiber cell model. This shear stress is assumed to arise from compression at the fiber/matrix interface and the corresponding frictional resistance to sliding. In order to maintain equilibrium in the cross-section, the average axial fiber stress must be

$$\sigma_f = \frac{\sigma}{f} - \frac{2\tau z}{r}. \tag{3}$$

where z is the distance from the crack plane, r is the fiber radius, and σ is the global applied stress.

The matrix stress as a function of position is then obtained from equilibrium

$$\sigma_m = \frac{f}{(1-f)} \frac{2\tau}{r} z. \tag{4}$$

If the bond between the fiber and the matrix is purely frictional, then the original 'far-field' matrix stress given by Equation (1) will be reached at a distance δ from the matrix crack, where δ is given by

$$\delta = \frac{r\sigma}{2\tau} \frac{E_m}{E_c} \frac{(1-f)}{f}, \tag{5}$$

for this model. At δ, strain compatibility between the fibers and the matrix is regained, and the constituent stresses are given by

$$\sigma_f = \sigma_{app} \frac{E_f}{E_c}, \ \sigma_m = \sigma_{app} \frac{E_m}{E_c}. \tag{6}$$

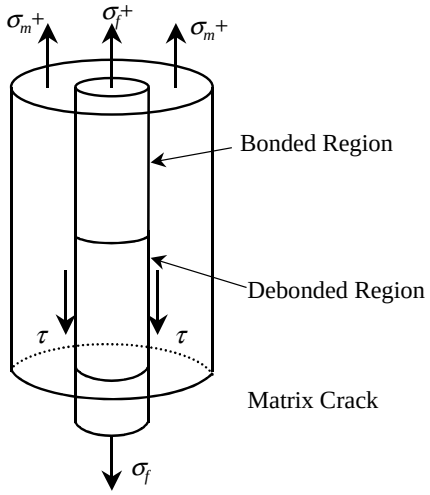

Figure 3. Stress transfer at the fiber/matrix interface

The recovery of matrix stress implies that the matrix can crack multiple times along the length of the composite. As the matrix stress in the slip region around a matrix crack will be less than the original stress which resulted in the formation of the matrix crack over a distance δ from the matrix crack, no further cracks can form in this region. This region, extending a distance δ from the matrix crack is called the *matrix slip length*, as the fiber is slipping through the matrix in this region.

In materials where the interface bonding is not purely frictional, the slip zone is followed by a bonded region as one moves away from the matrix crack. In the bonded region the interface remains intact, accommodating the relative displacements of the fiber and matrix through elastic deformation. In this case the length of the slip zone is [5]

$$l = r\frac{1-f}{f}\frac{\sigma-\sigma_i}{2c_3\tau}, \tag{7}$$

This expression is similar to Equation (5), except that the applied stress is modified by a stress σ_i. This is the global stress required to propagate a debond along the fiber length and is related to the fracture toughness of the interface. Therefore the slip zone of a bonded fiber is shorter than that of a frictionally constrained fiber. The parameter c_3 is a function of the elastic moduli of the fibers and matrix.

The first determination of the value of the matrix cracking stress under a purely frictional interface was conducted by Aveston, Cooper, and Kelly (ACK) [6]. They used an energy approach to determine the critical stress which would cause a matrix crack to form across the cross-section of the composite. That critical stress is

$$\sigma^* = \left[\frac{6\tau\Gamma_m f^2 E_f E_c}{(1-f)E_m^2 r}\right]^{1/3}, \tag{8}$$

where Γ_m is the toughness of the matrix. According to the ACK theory, when the stress reaches σ^*, cracks with a spacing between x and $2x$ will form simultaneously over the

length of the composite. The composite strain at which cracking occurs may be greater than the strain-to-failure of the unreinforced matrix; the fibers suppress crack formation.

Marshall, Cox, and Evans (MCE) [7] considered the propagation of the matrix crack across the cross section using a stress intensity approach and showed that the solutions were of the same form as the ACK energy approach. Furthermore, they demonstrated that the ACK stress was a limiting stress for large initial cracks and that as the size of the initial crack decreased, the stress required for propagation increased.

Experimental evidence overwhelmingly demonstrates that matrix cracks form over a range of applied stresses in the same specimen and have variations in their spacing (e.g. [8, 9]). Thus, an accurate theory for the evolution of matrix cracks must include some statistical description of matrix flaw size distribution. Stochastic formation of multiple matrix cracks has been discussed by Curtin et al. [10, 11]. One of the key results of this work was the development of expressions for the evolution of matrix cracks which showed that the final average crack spacing, $\overline{x}_f$, was given by the expression

$$\overline{x}_f = \Lambda \delta_R , \tag{9}$$

where Λ is a nondimensional parameter which depends on the matrix strength properties, the thermal stress in the matrix, and the ACK critical matrix cracking stress. The parameter δ_R is a slip length associated with a characteristic stress in the matrix and is a function of the strength properties of the matrix and the interface frictional stress, τ.

The loss of load carrying capability of the matrix resulting from multiple matrix cracking can have a significant effect on the stiffness of the composite. Should the matrix damage be so severe that the matrix cannot carry any load, then the applied stress is carried only by the fibers, and the composite modulus would be

$$E_c = fE_f . \tag{10}$$

However, during a stochastic matrix cracking process there are regions where the fibers and matrix are still intact and the overall stiffness of the composite is then some intermediate value which lies between the values given by Equations (10) and (2). Kuo and Chou [12] used shear lag models to analyze the loss of stiffness of CMCs during the matrix cracking process. He et al. [13] used finite element models to solve similar problems. He et al. showed that shear lag models are fairly accurate, except in the case of interfaces which have a high resistance to debonding. In these cases, the shear lag models are very inaccurate unless the slip zone has a length of at least two fiber diameters.

When CMC's with matrix cracks undergo non-monotonic loading, the fiber stresses in the slip zone become much more complicated than those described by Equation (3) as the frictional shear stress changes sign to oppose fiber motion. Marshall [14] studied the load and unload behavior of a single fiber with frictional bonding under load, and found that the resulting hysteresis loops had parabolic shapes. Evans and colleagues [15, 16, 17] extended the work of Marshall to composites containing many fibers and interfaces which have significant fracture toughness. Evans et al. [15] showed that the shape of the hysteresis loop was dependent on only two interface properties, the interface frictional shear stress, and the interface toughness. Ahn and Curtin [11] discussed the effect of stochastic matrix cracking on the hysteresis behavior of CMCs. Hysteresis loop analysis is discussed further in Chapter 5.

The fibers also undergo progressive damage during quasi-static loading. Testing of single fibers has revealed that the distribution of fiber strengths can be described by the Weibull distribution

$$P_f\left(\sigma, l\right) = 1 - e^{-\frac{l}{l_0}\left(\frac{\sigma}{\sigma_0}\right)^m}, \tag{11}$$

which states that the probability of failure of a fiber of length l under stress σ depends on a reference length, l_0, a reference stress at that reference length, σ_0, and the Weibull modulus, m. As the fibers in the composite break, the load they previously carried must

be carried by the remaining intact fibers. The manner in which the fibers transfer stress to one another is one of the important properties in strength determination. One extreme is the *global load sharing* case, where the load previously carried by a broken fiber is transferred to all intact fibers in the plane equally, regardless of spatial location. *Local load sharing* models concentrate the load on the nearest neighboring fibers.

The stress transfer due to the interface frictional stress into a fiber away from a fiber break results in an 'ineffective length' surrounding each fiber break. In this region, the fiber carries less load than an intact fiber. As the load is increased, the fibers progressively fail due to the statistical distribution of strengths. When every fiber in a cross-section is no longer intact (i.e. the cross-section intersects an ineffective region for each fiber), the composite fails. The failure surface of the broken composite will consist of fibers of various lengths extending from the bulk matrix. The length of fiber remaining extending from the matrix (the 'pullout length') is dependent on the frictional stress. High frictional stress results in a short ineffective length, which leads to short pullout lengths, while the opposite is true for low frictional stress.

In many systems the fibers are very strong compared to the matrix, and the matrix is fully cracked before a significant fraction of fibers have failed, a condition called matrix crack saturation. This implies that the variation in stress with position as described by Equation (3) is of minor effect at stresses sufficient to cause composite failure. In this case, Curtin [18] derived an expression which accounts for the statistical distribution of fiber strength as given in Equation (11), the load sharing between broken and unbroken fibers, and stress recovery in broken fibers governed by the shear stress, τ. The expression is given by

$$\sigma_u = f\sigma_c \left(\frac{2}{m+2} \right)^{\frac{1}{m+1}} \left(\frac{m+1}{m+2} \right), \tag{12}$$

where r is the fiber radius and σ_c is a quantity known as the characteristic strength

$$\sigma_c = \left(\frac{\sigma_0^m l_0 \tau}{r} \right)^{\frac{1}{m+1}}. \tag{13}$$

This expression has been found to be accurate for many different composite systems [19]. This model also predicts the distribution of fiber pullout lengths to be

$$< L >= \frac{1}{4} \lambda \delta_c, \tag{14}$$

where $<L>$ is the mean pullout length, λ is a nondimensional function of the Weibull modulus, m, and δ_c is the characteristic length of the composite

$$\delta_c = \left(\frac{\sigma_0 r l_0^{1/m}}{\tau} \right)^{\frac{m}{m+1}}. \tag{15}$$

This model was later extended to the case of fibers which suffered damage during processing [20]. Due to the fact that pullout in this case is fairly extensive, this has been termed the 'ductile' case.

When the matrix strength is comparable to the fiber strength, the variation if fiber stress with position becomes important. Thouless and Evans [21] and Curtin [22] have derived expressions for ultimate strength and pullout lengths when a single matrix crack dominates the fiber stress field. The result for the tensile strength of the composite in this case is

$$\sigma_u = f \sigma_c e^{-\frac{1}{m+1}}. \tag{16}$$

It is seen from a comparison of Equations (12) and (16) that the single matrix crack case has a higher tensile strength. Due to the highly stress-sensitive failure statistics of ceramic fibers, pullout in this case is virtually non-existent for moderate values of m. As a result, it has been termed the 'brittle' case.

While predictions of the full stress-strain curve of a CMC has been focused mostly on the ductile case where the matrix cracks are so closely spaced that the matrix stress is not

significant [e.g. 23, 24], the brittle case is also important. The stress-strain curve for a brittle CMC has also been examined [25]. The brittle stress strain curve was determined by tracking the increased strain in the intact fibers caused by both matrix cracking and fiber failure.

In materials with off-axis fibers (for processability or in anticipation of multi-axial loading, for example), cracks will first form perpendicular to the applied load through the regions unbridged by fibers [26]. At higher stresses these cracks will penetrate the 0° plies. A schematic of the process of matrix cracking is shown in Figure 4 for a silicon carbide reinforced calcium-aluminosilicate (SiC/CAS) composite.

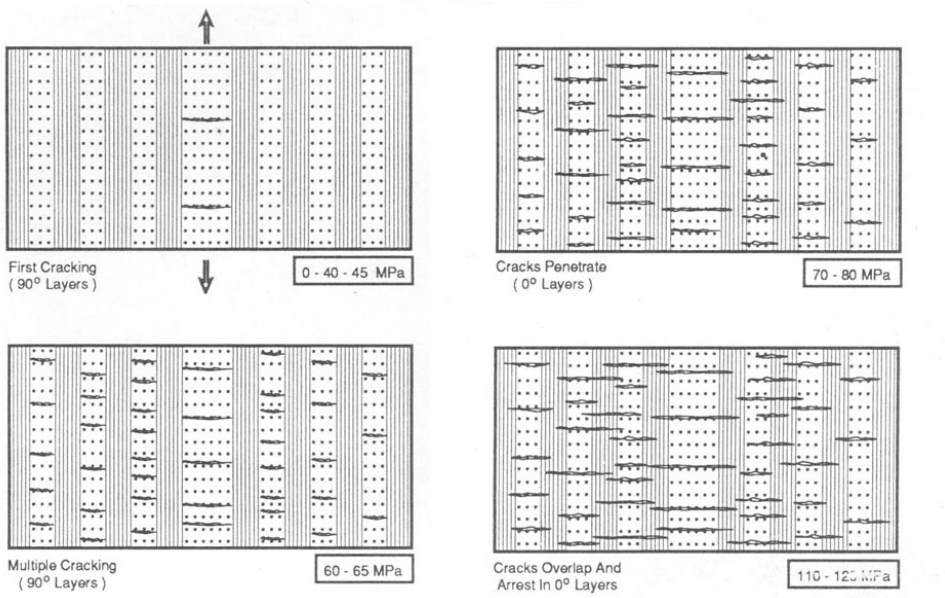

Figure 4. Matrix crack progression in a SiC/CAS composite

When the matrix cracks penetrate the plies that are bridged by fibers, stress concentrations occur at the interface between the bridged and unbridged regions. The crack opening can be directly related to the stresses on the bridging fibers, increasing the local fiber stresses. This effect has been considered by Xia, et al. [27]. They used a

finite-element model to determine the stresses. Similar work has been performed by Danchaivijit and Shetty (DS) [28, 29]. The DS bridging model relates the crack opening, *u*, to the crack surface traction, *p(u)*

$$p(u)=\frac{\eta\sigma}{2(1+\eta)}\left\{\left[1+\frac{16(1+\eta)^2 E_f f^2 \tau u}{\eta^2\sigma_\infty^2 r}\right]^{\frac{1}{2}}+1\right\},\ \eta=\frac{fE_f}{(1-f)E_m}, \qquad (17)$$

In summary, while the fibers control the ultimate failure of the composite, other failure modes cannot be ignored. The interactions between the matrix and the fibers can greatly influence the strength and toughness of the composite. This is especially true when off-axis fibers are considered. The strength of the composite can be greatly reduced by stress concentrations due to the unbridged regions.

2.2 Time-Dependent Mechanisms and Models

A stress-rupture test is one in which a constant load is applied to the component until failure occurs. Upon the initial loading to the constant stress, damage develops much as it would during a tensile test. However, further damage development is often unique to long term tests. Both deformation and strength are affected by elevated temperature loading and both can be important in applications.

The mechanisms of deformation in monolithic materials are typically described by a mechanism map, which gives the dominant deformation mechanism as a function of stress and temperature. Shown in Figure 5 is a sample deformation mechanism map for pure silver with a 32 μm grain size. The effect of grain size and applied stress on the deformation rate is different for each of the mechanisms. Both Coble and Nabarro creep are linear with applied stress, but for Nabarro creep the creep rate is proportional to (grain size)$^{-2}$ and for Coble creep the creep rate is proportional to (grain size)$^{-3}$. Other mechanisms, such as dislocation creep, are typically non-linear with applied stress.

Upon initial loading, the load carried by each of the constituents will be governed by their quasi-static behavior. However, creep deformation may lead to redistribution of the load throughout the test as the material with the faster creep rate sheds load to the material with the slower creep rate. This can lead to a very nonlinear creep deformation curve with time.

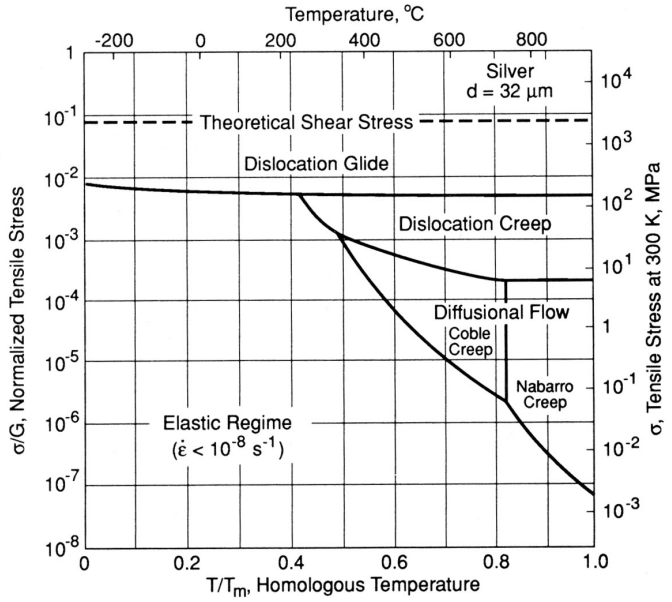

Figure 5. Deformation mechanism map for 32 μm grain size silver [30]

If the applied load is less than the matrix cracking stress, the matrix will carry load under stress rupture conditions. McLean [31], among others, has examined the deformation response of a composite under creep conditions with a load-bearing matrix. He considered a matrix which obeys power law creep

$$\varepsilon_m = \frac{\sigma_m}{E_m} + B\sigma_m^n, \tag{18}$$

(where B and n are creep law constants) containing elastic (non-creeping) fibers. The deformation of the composite as a function of time, t, is given by

$$\varepsilon(t) = \frac{\sigma}{fE_f} - \frac{(1-f)}{fE_f}\left[\left(\frac{E_c}{E_m\sigma}\right) + \frac{f(n-1)E_f E_m Bt}{E_c}\right]^{\frac{-1}{n-1}}. \tag{19}$$

As time increases, this predicts the composite strain to asymptotically approach the strain expected when the applied load is carried entirely by the fibers.

$$\varepsilon = \frac{\sigma}{fE_f}. \tag{20}$$

McLean did not perform a failure analysis for continuously reinforced composites, but instead considered a creep strain of 1% to signify the onset of fiber failure and composite failure.

Du and McMeeking [32] combined the stress analysis of McLean with Curtin's tensile strength model (Equation (12)) to more accurately account for fiber strength statistics in component failure. For this model they found the strain rate of the composite to be

$$\dot{\varepsilon} = \frac{\left\{\frac{\sigma}{\sigma_c} - f\left(\frac{E_c\varepsilon}{\sigma_c}\right)\left[1-\frac{1}{2}\left(\frac{E_c\varepsilon}{\sigma_c}\right)^{m+1}\right]\right\}}{1+\frac{f}{1-f}\frac{E_f}{E_m}\left[1-\left(1+\frac{m}{2}\right)\left(\frac{E_c\varepsilon}{\sigma_c}\right)^{m+1}\right]}\frac{B\sigma_c^n}{(1-f)^n}. \tag{21}$$

This model predicts the creep strain will become infinite with time as the fibers break, and this defines failure of the composite. Fabeny and Curtin [33] used a similar approach to solve this problem but included the effects of matrix plasticity and fibers that obey power law creep.

Another important creep effect is due to the interface frictional stress. When a fiber breaks, shear at the interface transfers stress back into the broken fiber. The shear stress can result in shear creep in the matrix which reduces the magnitude of the interfacial shear stress, resulting in longer ineffective lengths and weaker composites. This phenomenon has been examined in continuous fiber reinforced composites by Du and

McMeeking [32], and Iyengar and Curtin [34]. Iyengar and Curtin found for matrix creep exponents of 2 or 3, the shear stress, $\tau(t)$, at the interface obeys the expression

$$\frac{\sigma^2(n-1)}{4\left(\sqrt{\frac{\pi}{2f\sqrt{3}}}-1\right)f(n+1)\tau(0)^2}\left[1-\left(\frac{\tau(t)}{\tau(0)}\right)^{-n-1}\right]+\frac{2(1+\nu)E_f}{E_m}\left[1-\left(\frac{\tau(t)}{\tau(0)}\right)^{-n+1}\right]=-3^{(n+1)/2}BE_f\tau(0)^{n-1}t \quad (22)$$

where ν is the matrix Poisson's Ratio and $\tau(0)$ is the initial frictional stress. Here Iyengar and Curtin assumed that the matrix has fully relaxed in axial creep and carries no axial stress.

Matrix cracking may still occur during the initial loading to the steady stress at which the rupture test is run. Begley et al. [35] have considered the effect of matrix cracking on the creep deformation of a composite. The additional stress carried by the creeping fibers due to the matrix crack increases the creep rate over that of Equation (19). For fibers which exhibit linear creep (the creep exponent in Equation (18) is unity), the increase in creep rate is proportional to the applied stress squared. The fiber creep may also result in an increase in crack opening, which leads to an increase in the stress intensity factor at the crack tip. They examined the growth of pre-existing matrix flaws into matrix cracks due to this mechanism with the stress analysis of Marshall et al. [7].

Materials also lose strength due to stresses applied at elevated temperatures. This strength degradation typically occurs due to two major mechanisms: creep cavitation and slow crack growth [36]. Creep cavitation is the formation of voids in the ceramic at grain boundaries. With time, these voids continue to form and grow until they coalesce, forming a crack which is sufficient to cause failure. Slow crack growth involves the preferential growth of creep cavitation in the highly stressed region ahead of an existing crack tip. These voids grow until they reach a size sufficient to cause local failure, resulting in crack tip advance. Typically, creep cavitation dominates at high temperatures and/or low stresses, and slow crack growth at low temperatures and/or high stresses [37]

Creep cavitation consists of two phases: cavity nucleation and cavity coalescence. Although the stresses required for cavity nucleation are typically much higher than those seen in service [38], porosity can serve as an initiation site, reducing the required stress. For high applied stresses, the interactions between cavities is limited and failure occurs only when a sufficient number of continuous cavities are created and approximate a macrocrack. A probabilistic treatment of this condition results in the expression [39]

$$\ln\left[t_n e^{\frac{Q}{RT}}\right] = A - n\ln[\sigma] - D\sigma^2 \tag{23}$$

In this expression Q is the activation energy for cavity propagation, R is the ideal gas constant, T is the absolute temperature, t_n is the nucleation time, and A, D and n are constants depending on the mechanism of cavity propagation. At lower stresses, Monkman-Grant behavior is found to describe the failure times

$$t_f \dot{\varepsilon} = F \tag{24}$$

where F is a constant related to cavity propagation along a grain boundary.

Slow crack growth in the fibers as a failure mechanism has been considered by Iyengar and Curtin [40]. Their analysis begins with a power law for crack growth in the fiber

$$\frac{da}{dt} = CK^{\beta} \tag{25}$$

where a is the crack size, C and β are material constants, t is time, and K is the stress intensity factor at the crack tip. If fiber failure occurs when the crack tip stress intensity factor reaches a critical value, K_{Ic}, the lifetime of each fiber can be determined based on its initial strength and stress history. If the statistical distribution of initial fiber strengths is known, the number of broken and intact fibers can be determined as a function of time and applied stress. Equilibrium is used to account for the load sharing from broken to intact fibers. The equilibrium and fiber failure equations must be solved simultaneously in time

$$\tilde{\sigma}_{fiber} = \frac{1}{\tilde{\rho}}\left[1 - e^{-\tilde{\rho}\tilde{T}}\right]$$
$$\tilde{\rho}\left(\tilde{T},\tilde{t}\right) \cong \left[\tilde{T}\left(\tilde{t}\right)^{\beta-2} + \int_0^t d\tilde{t}\tilde{T}\left(\tilde{t}\right)^{\beta}\right], \quad (26)$$

where $\tilde{T}$ is a normalized stress carried by the intact fibers. Included in this model is the assumption that the matrix is completely damaged and that the fibers carry the entire applied load. If this is not the case, and the matrix does carry load and can creep, this expression may not be completely valid.

In summary, a great number of mechanisms which can cause time-dependent failure have been examined by previous investigators. However, they can be divided into three basic categories:

1 – Stress redistribution from one constituent to the other due to differing creep rates

2 – Changes in interface behavior due to creep deformation

3 – Changes in material strength due to damage

2.3 Properties of Nextel 610 Fibers and Composites

Several research groups have performed experimental studies on Nextel 610 fibers and composites containing Nextel fibers. These studies will be used to determine many of the parameters necessary for accurate use of the developed micromechanical models.

2.3.1 Strength Properties

The 3M Company provide the basic characteristics of Nextel 610 fibers as listed in Table I. Weibull properties for strength have been collected at room temperature by a number of investigators and are shown in Table II.

Table I. Properties as reported by 3M

	Nextel 610 [41]
Strength @ 1.0" Gage	360 ksi
	2500 MPa
Modulus	54 msi
	370 GPa
Diameter	12 μ
Composition	99+% Al_2O_3

Table II. Weibull properties at room temperature of Nextel fibers

	Nextel 610	
Reference	[42]	[43]
Gage Length	25 mm	40 mm
σ_0 (MPa)	3200	1770
m	11.4	6.6

The increased Weibull modulus and strength as reported in [42] as compared to [43] has been attributed to improved process control.

Das [44, 45] found that pure thermal exposure (no applied stress) at 982°C (1800°F) for up to 2000 hours did not affect the strength of Nextel 610 fiber tows, although he did notice some grain coarsening. Other researchers [46] found that 10 hour exposures at temperatures as low as 450°C had some small effect on the room temperature strength. Finally, in another series of exposure tests [43], two hours at 900°C and above reduced the tensile strength significantly. These results are shown in Table III. The decrease in these last tests was attributed to an increase in grain size. It should be mentioned that

those fibers most affected by temperature exposure were probably earlier batches, as based on the date of the publications, and later process improvements may make these data sets suspect.

The elevated temperature strengths of virgin Nextel fibers are shown in Figure 6 [47].

Table III. Weibull parameters of Nextel 610 fiber after high temperature exposure [43]

(40 mm gage length)	m	σ_0 (MPa)
900°C for 2 hours	4.85	1400
1100°C for 2 hours	4.78	1040
1300°C for 2 hours	4.79	660

2.3.2 Creep Properties

For Nextel 610 fibers tested in air, the creep rate is given by [48] (with stress in ksi)

$$\dot{\varepsilon} = 2.944\text{x}10^{15}\sigma^3 e^{\left(\frac{-Q}{RT}\right)} \quad (27)$$

where Q was determined to by 660 KJ. The creep rupture mechanisms were also examined. In many cases, the failure was due to coalescence of cavities into a large crack. Global and/or local necking also exists. This indicates that the creep is interface controlled and affected by the elongated grain structure.

The creep strength of Nextel 610 fibers has also been investigated [49, 50]. The results indicated two regimes of creep damage: slow crack growth at low stresses and temperatures and cavitation at higher stresses and temperatures. Figure 7 shows the stress

rupture data for the Nextel 610 fibers. The researchers found that the data could be collapsed into a Larson-Miller plot. This is shown in Figure 8. The two regimes of damage were distinguished by the increase in the slope of the failure curve at high values of q [51].

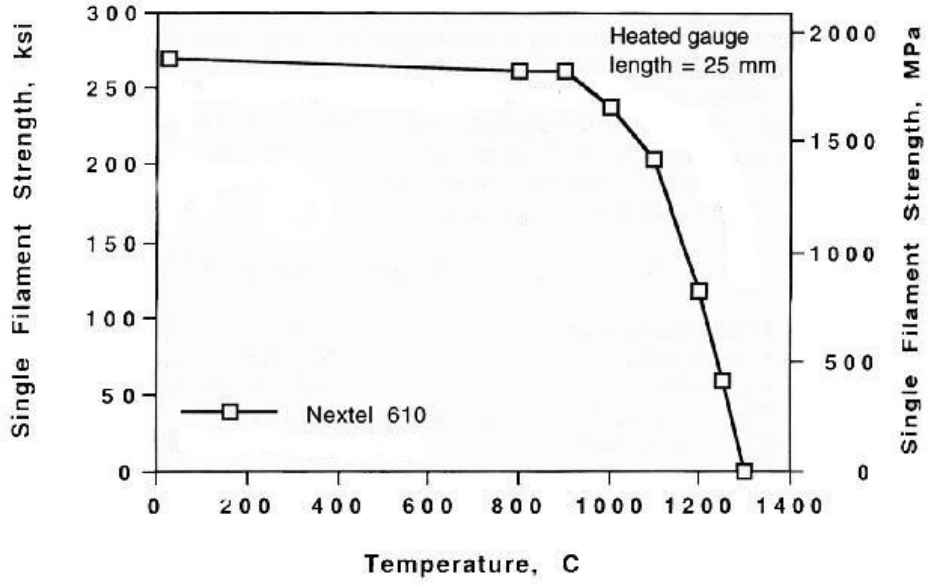

Figure 6. Nextel 610 fiber strength retention at elevated temperatures [47]

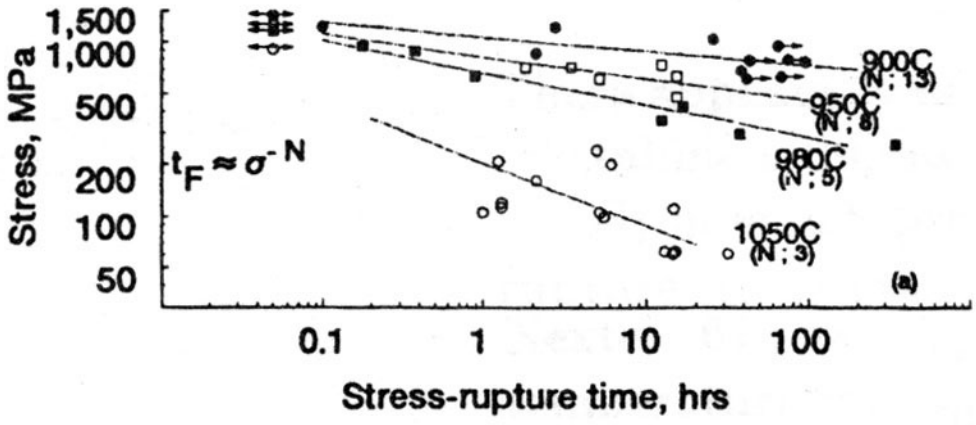

Figure 7. Stress-rupture of Nextel 610 fibers [49]

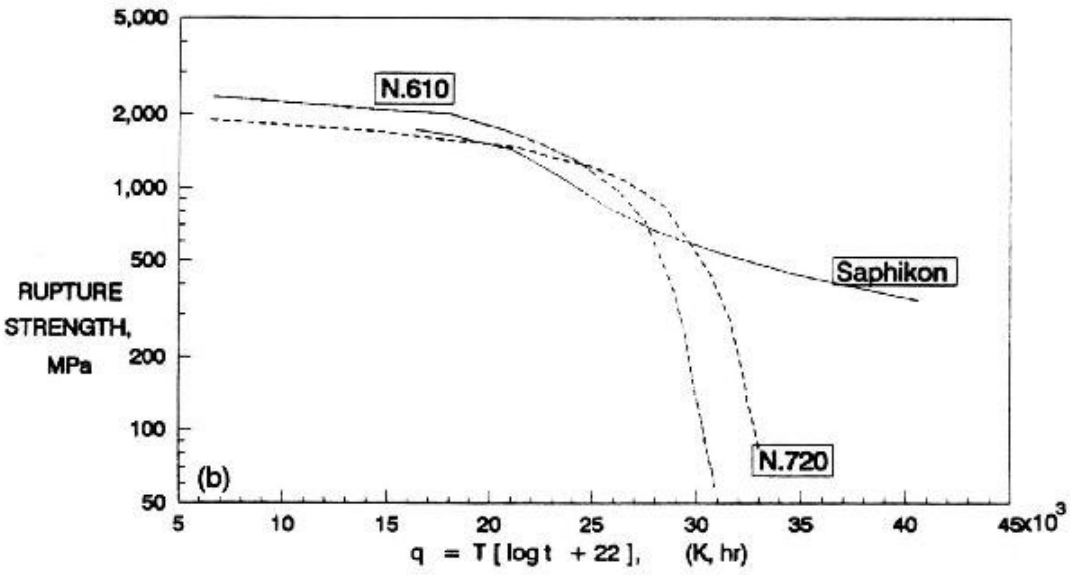

Figure 8. Larson-Miller plot of alumina fibers [50]

2.3.3 Composite Properties

Nextel 610/Al_2O_3 composites were fabricated with the DIMOX^{TM} process [52]. The fibers were coated with a BN/SiC duplex interface and woven in an 8-harness satin pattern. Total fiber volume fractions were approximately 30-35%. The average tensile strength was 230 MPa (33 ksi) with a modulus of 170 GPa (24.7 msi). Flexural strength data as a function of temperature are shown in Figure 9. The fracture toughness decreased from 17 MPa$\sqrt{m}$ at room temperature to 9 MPa$\sqrt{m}$ in air at 1000°C. Debonding occurred at the fiber-BN interface. The fracture surfaces indicated a transgranular fiber failure mode at room temperature, but intergranular failure at 1000°C. The intergranular failure mode implies that the grain boundary phases are weak at 1000°C, resulting in large reductions in fiber strength. Specimens exposed to air at elevated temperatures showed extensive weakening even at 600°C for only 10 hours as shown in Figure 10 [53]. The failure surfaces showed reduced pullout and it was

proposed that this weakening was due to changes in the interface properties. Unloading/reloading analysis of the aged specimens showed an increase in fiber residual stress with aging temperature [54].

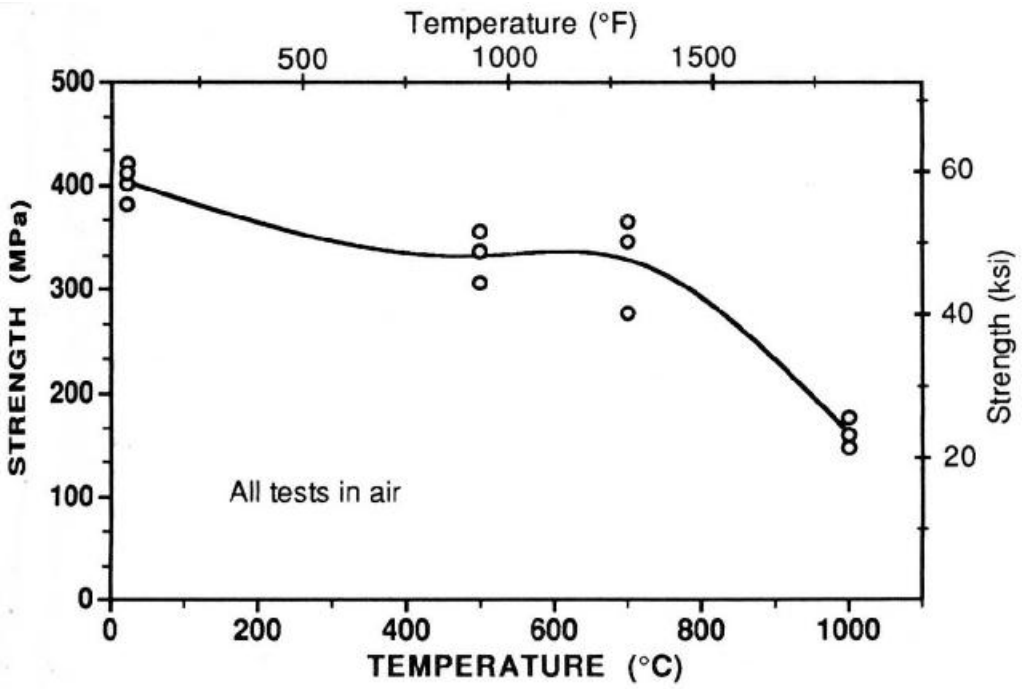

Figure 9. Four-point flexural strength of Nextel 610/alumina composites [52]

One of the most widely studied composites using Nextel 610 fibers is produced by General Electric and is called GEN IV. This composite has a porous aluminosilicate matrix to which the fibers (approximately 31 vol. %) are strongly bonded. In this material individual fibers do not debond, leading to a planar crack across a fiber tow. However, the porous matrix surrounding the tow can fail in shear allowing for an analogous failure mechanism [55, 56] involving tow pullout rather than fiber pullout.

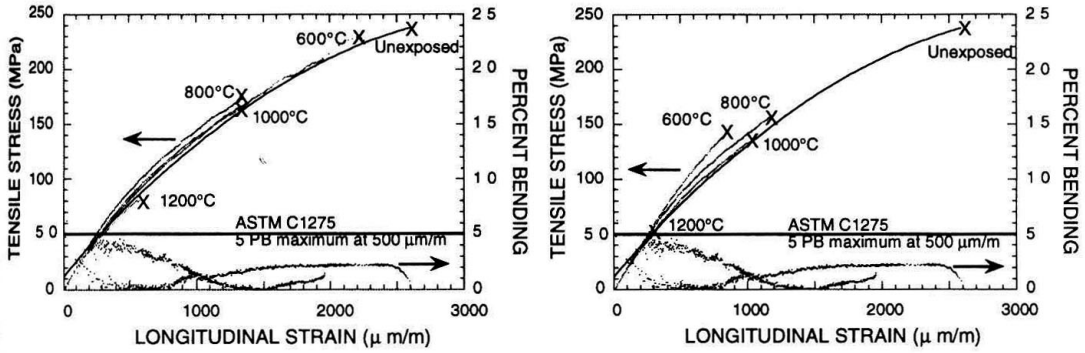

Figure 10. Strength of Nextel 610/DIMOX Al_2O_3 composites After aging a) 10 hours, b) 100 hours [53]

GEN IV has been extensively characterized by Lee et al. [57], Kramb et al. [58], Zawada [59], and Zuiker [60]. The tensile strength at room temperature is 205 MPa and at 173 MPa at 1000°C. Failure strain ranges from approximately 0.36% at room temperature to 0.29% at 1000°C. The elastic modulus was approximately 70 GPa at both temperatures. Representative stress-strain curves are shown in Figure 11, and demonstrate that the stress-strain behavior is relatively unchanged at elevated temperatures.

Stress-rupture at 1000°C and 1100°C was also run on GEN IV specimens which demonstrate significant strength reduction (Figure 12**).** Creep curves at 1100°C are shown in Figure 13**.**

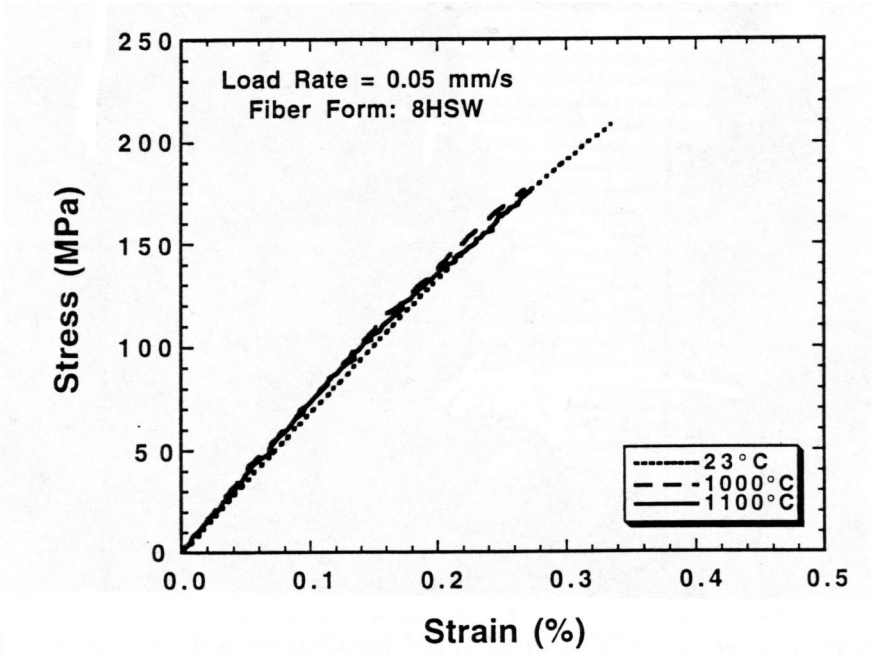

Figure 11. Stress-strain curves for GEN IV composite

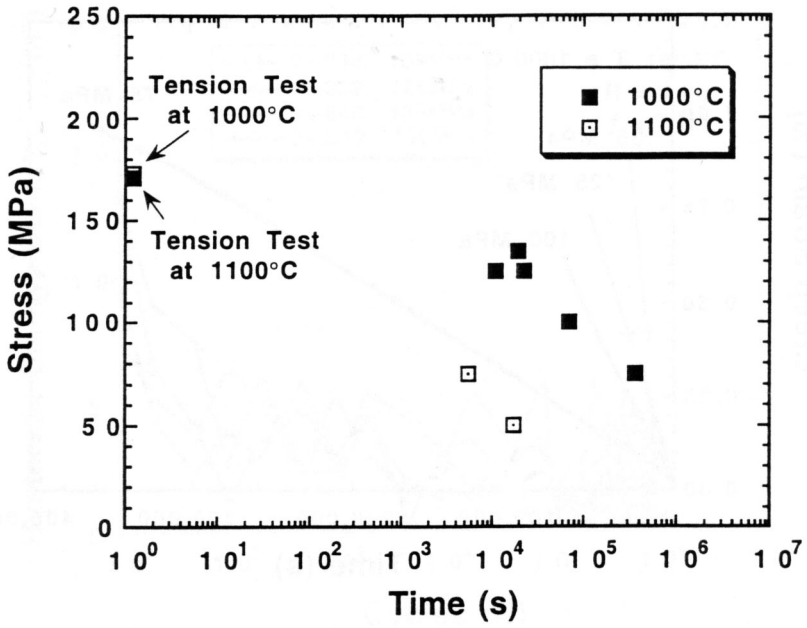

Figure 12. Stress-rupture lifetime of GEN IV composite

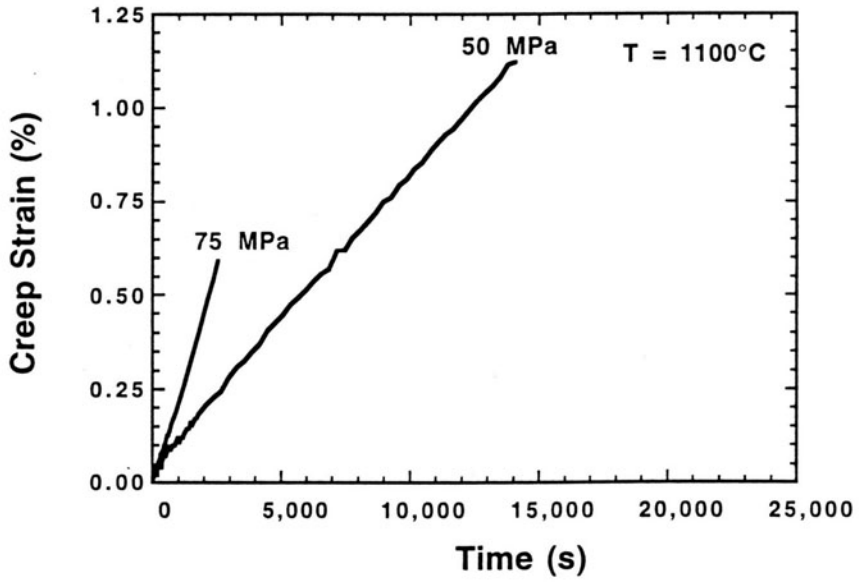

Figure 13. Creep deformation of GEN IV composite

The fracture toughness of GEN IV has also been determined to be approximately 16 MPa$\sqrt{m}$ at room temperature and 8 MPa$\sqrt{m}$ at 950°C. The specimens failed at a matrix crack which grew from the initial notch and passed through the 90° tows and the matrix-rich regions. The fiber bundles debonded from the remainder of the composite and pulled out of the matrix and had uncorrelated fiber failures at their ends. The 90° tows and matrix-rich regions often disintegrated near the fracture surface due to extensive cracking. At elevated temperatures the damage in the off-axis regions was more limited to the crack plane and the fiber breaks in the 0° tows were more correlated than at room temperature.

Chapter 3 Composite Stress-Rupture Modeling

The stress-rupture behavior of oxide composite materials is controlled by the degradation of the reinforcing fibers. Therefore, the composite failure model is based on the accumulation of fiber failure. The effects of the matrix and the interface are included in the stress analysis which governs the rate of fiber degradation. The initial focus in this section is on the behavior of a single fiber in a composite without considering the effect of other fibers. Subsequently, the behavior of the collection of fibers in the composite is considered.

3.1 Fiber Behavior

The behavior of a ceramic fiber under some time-dependent degradation mechanism is an extension of the behavior under quasi-static loading (i.e. tensile strength). Therefore, the tensile behavior of ceramic fibers is discussed first.

3.1.1 Fiber Tensile Behavior

Ceramic fibers are brittle materials, and thus their strengths are commonly described using Weibull statistics. For a material which obeys a two-parameter Weibull distribution, the probability of failure occurring in a fiber element of length δz over a stress range stress σ to $\sigma + \delta\sigma$ is given by

$$p_f(\sigma, \delta\sigma, \delta z) = \frac{m\sigma^{m-1}}{\sigma_0^m}\frac{\delta z}{l_0}\delta\sigma, \tag{28}$$

where σ_0, m, and l_0 are the Weibull properties of the fiber. The probability of survival of the fiber element is then

$$p_s(\sigma, \delta\sigma, \delta z) = 1 - p_f(\sigma, \delta\sigma, \delta z). \tag{29}$$

The probability of survival of a fiber of length *2l* with *2N* elements each of length δz_i and stress $\sigma(z)$ is then the product of the probabilities of survival of each individual fiber element

$$P_s^{'}\left(\sigma,\delta\sigma,2l\right)=\prod_{i=0}^{2N}1-p_f\left(\sigma\left(z_i\right),\delta\sigma\left(z_i\right),\delta z_i\right) \tag{30}$$

Similarly, the probability of survival of this fiber over a stress range from 0 to T divided into *M* intervals of increment $\delta\sigma_j$ is given by

$$P_s\left(T,2l\right)=\prod_{i=0}^{2N}\prod_{j=0}^{M}\left[1-p_f\left(\sigma_j\left(z_i\right),\delta\sigma_j\left(z_i\right),\delta z_i\right)\right], \tag{31}$$

where the stress, $\sigma(z)$ is a function of applied stress σ_{app}.

Recall that for small values of $P_f(\sigma,\delta\sigma,z)$,

$$\prod_{i=0}^{2N}\left[1-p_f\left(\sigma_j\left(z_i\right),\delta\sigma_j\left(z_i\right),\delta z_i\right)\right]\cong e^{-\sum_{i=0}^{2N}p_f\left(\sigma_j(z_i),\delta\sigma_j(z_i),\delta z_i\right)}, \tag{32}$$

and similarly

$$\prod_{j=0}^{M}e^{-\sum_{i=0}^{2N}p_f\left(\sigma_j(z_i),\delta\sigma_j(z_i),\delta z_i\right)}=e^{-\sum_{j=0}^{M}\sum_{i=0}^{2N}p_f\left(\sigma_j(z_i),\delta\sigma_j(z_i),\delta z_i\right)}. \tag{33}$$

Finally, replace the summations with integration (in the limit as N $\longrightarrow\infty$ and $\delta\sigma\longrightarrow 0$) and use Equation (28) to yield

$$P_s\left(\sigma_{app},2l\right)=e^{-\int_0^{\sigma_{app}}\int_{-l}^{l}\frac{m}{\sigma_0 l_0}\left(\frac{\sigma(z)}{\sigma_0}\right)^{m-1}dz\frac{d\sigma(z)}{dS}dS}, \tag{34}$$

which is the probability that the fiber survives the stress profile $\sigma(z)$ which is a result of the application of stress, σ_{app}.

The probability that failure will occur at position *z* under applied stress $\sigma(z)$, and not at any other position or stress previous is given by the product of Equation (34) and Equation (28)

$$P_f\left(\sigma_{app},2l,z\right)=\frac{m\sigma\left(z\right)^{m-1}}{l_0\sigma_0^m}e^{-\int_0^{\sigma(z)}\int_{-l}^{l}\frac{m}{\sigma_0 l_0}\left(\frac{\sigma'(z')}{\sigma_0}\right)^{m-1}dz'\frac{d\sigma'(z)}{dS}dS}\delta z\delta\sigma\left(z\right). \tag{35}$$

The probability that the fiber will fail at any point along the length of the fiber at or below the peak stress σ_{app}, denoted $q(\sigma_{app},l)$, is then given by the integral of Equation (35)

$$q\left(\sigma_{app},l\right)=\int_0^{\sigma_{app}}\int_{-l}^{l}\frac{m\sigma'\left(z\right)^{m-1}}{l_0\sigma_0^m}e^{-\int_0^{\sigma'(z)}\int_{-l}^{l}\frac{m}{\sigma_0 l_0}\left(\frac{\sigma'(z')}{\sigma_0}\right)^{m-1}dz'\frac{d\sigma'(z')}{dS}dS}dz\frac{d\sigma'\left(z\right)}{dR}dR. \tag{36}$$

In this expression, the argument of the exponent is the exact differential of the rest of the integrand, thus Equation (36) becomes

$$q\left(\sigma_{app},l\right)=1-e^{-\int_0^{\sigma_{app}}\int_{-l}^{l}\frac{m}{\sigma_0 l_0}\left(\frac{\sigma(z)}{\sigma_0}\right)^{m-1}\frac{d\sigma(z)}{d\sigma'}dzd\sigma'}, \tag{37}$$

which is the probability that a fiber of length *2l* fails at or below some applied stress σ_{app}. The integration variable has been changed from *S* to σ'

If the fiber stress is constant over the fiber length (i.e. $\sigma(z) = \sigma$'), Equation (37) can be reduced to the Weibull expression for the probability of failure

$$q\left(\sigma,l\right)=1-e^{\frac{2l}{l_0}\left(\frac{\sigma}{\sigma_0}\right)^m}. \tag{38}$$

However, in the more general case where the fiber stress depends on position, Equation (37) is more complicated. Consider the stress on a fiber near an isolated matrix crack located at position *z=0* under an applied stress, σ_{app}. As discussed in Section 2.1, at the matrix crack plane, the entire load is carried by the fiber and therefore the fiber stress is σ_{app}/f. Away from the matrix crack, stress is transferred from the fiber to the matrix through the interface frictional stress,

$$\sigma_f(z) = \frac{\sigma_{app}}{f} - \frac{2\tau|z|}{r}, \tag{3}$$

where the absolute distance is taken to account for the fact that the stress profile is symmetric away from the matrix crack. Far away from the matrix crack, the stress carried by the fiber fiber is the far-field value,

$$\sigma_{f-ff} = \sigma_{app}\frac{E_f}{E_c} \tag{6}$$

The distance at which the transition from Equation (3) to Equation (6) occurs is the distance, δ,

$$\delta = \frac{r\sigma_{app}}{2\tau f}\left[\frac{(1-f)E_m}{E_c}\right] \tag{5}$$

If Equation (3) were to describe the fiber stress over the entire fiber length, the fiber stress would reach zero at a distance l_s

$$l_s = \frac{r\sigma_{app}}{2\tau f}, \tag{39}$$

where l_s is called the *fiber slip length*.

Now the fiber stress as a function of position can be written as

$$\begin{aligned} \sigma_f(z) &= \frac{\sigma_{app}}{f}\left(1-\frac{|z|}{l_s}\right), \quad 0<|z|<\delta \\ \sigma_f(z) &= \sigma_{app}\frac{E_f}{E_c}, \qquad \delta<|z| \end{aligned}, \tag{40}$$

These parameters are shown graphically in Figure 14.

Substitution of Equation (40) into Equation (37) with a maximum applied stress σ_{app} yields the probability of failure under the stress field of Equation (40) as

$$q\left(\sigma_{app},l\right)=1-e^{-2\int_0^{\sigma_{app}}\left[\int_0^{\delta}\frac{m}{f\sigma_0 l_0}\left(\frac{\sigma'}{f\sigma_0}\right)^{m-1}\left(1-\frac{z}{l_s}\right)^{m-1}dz+\int_{\delta}^{l_s(\sigma_{app})}\frac{m}{\sigma_0 l_0}\left(\frac{\sigma'}{\sigma_0}\right)^{m-1}\left(\frac{E_f}{E_c}\right)^{m}dz\right]d\sigma'}, \tag{41}$$

where the tranformation of the stress variable from $\sigma(z)$ to the integration variable σ' has been performed separately for the two regions using

$$\begin{aligned}\frac{d\sigma(z)}{d\sigma'}&=\frac{1}{f}, \quad 0<|z|<\delta\\ \frac{d\sigma(z)}{d\sigma'}&=\frac{E_f}{E_c}, \ |z|>\delta\end{aligned} \tag{42}$$

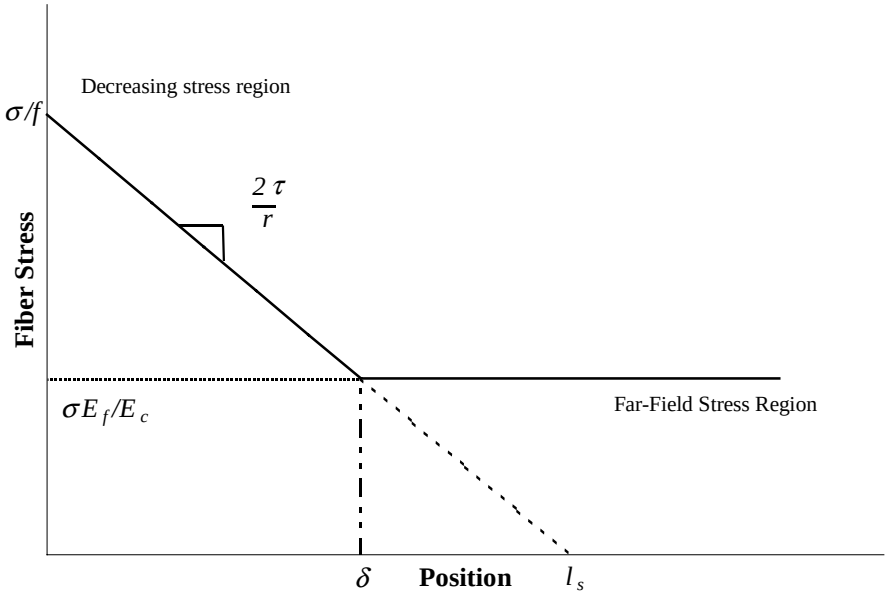

Figure 14. Fiber stress as a function of distance away from a matrix crack

The upper limit of the position integral is the slip length at the applied stress. The position integrals can be performed

$$\int_0^{\delta}\frac{m}{f\sigma_0 l_0}\left(\frac{\sigma'}{f\sigma_0}\right)^{m-1}\left(1-\frac{z}{l_s}\right)^{m-1}dz=\frac{(\sigma')^m}{2f^{m+1}\sigma_c^{m+1}}\left[1-\left(1-\frac{\delta}{l_s}\right)^m\right]=\frac{(\sigma')^m}{2f^{m+1}\sigma_c^{m+1}}\left[1-\left(\frac{fE_f}{E_c}\right)^m\right] \tag{43}$$

$$\int_{\delta}^{l_s(\sigma_{app})} \frac{m}{\sigma_0 l_0}\left(\frac{\sigma'}{\sigma_0}\right)^{m-1}\left(\frac{E_f}{E_c}\right)^m dz = \frac{m}{2f\sigma_c^{m+1}}\left(\frac{E_f}{E_c}\right)^m\left[\sigma_{app}-\sigma'\left(1-\frac{fE_f}{E_c}\right)\right]\sigma'^{m-1}, \quad (44)$$

where the *characteristic strength*, σ_c, has been introduced

$$\sigma_c = \left(\frac{\sigma_0^m l_0 \tau}{r}\right)^{\frac{1}{m+1}}, \quad (13)$$

as well as Equations (5) and (39) for the values of δ and l_s.

The expression for $q(\sigma_{app},l_s)$ is now

$$q\left(\sigma_{app},l_s\right) = 1-e^{-\int_0^{\sigma_{app}}\left\{\left[1-\left(\frac{fE_f}{E_c}\right)^m\right]\left(\frac{\sigma'}{f\sigma_c}\right)^m+m\left(\frac{\sigma'}{f\sigma_c}\right)^{m-1}\left(\frac{fE_f}{E_c}\right)^m\left(\frac{\sigma_{app}}{f\sigma_c}-\frac{\sigma'}{f\sigma_c}\left(1-\frac{fE_f}{E_c}\right)\right)\right\}\frac{1}{f\sigma_c}d\sigma} \quad (45)$$

Make the substitutions

$$\tilde{T}' = \frac{\sigma'}{f\sigma_c}\ ,\ \alpha = f\frac{E_f}{E_c} \quad (46)$$

and integrate to yield

$$q\left(\tilde{T},l_s\left(\tilde{T}\right)\right) = 1-e^{-\frac{1}{m+1}\tilde{T}^{m+1}\left[1+m\alpha^{m+1}\right]}, \quad (47)$$

which is the final result – the probability of failure of a fiber near an isolated matrix crack. The failure probability depends on three variables: 1) the applied stress, $\tilde{T}$, 2) the fiber Weibull modulus, *m*, and 3) a parameter which represents the effect of the matrix stiffness, α.

The probability of fiber failure is sensitive to stress to the power of *m*, so under a linearly decreasing stress field the majority of fibers will fail near the matrix crack plane where the fiber stresses are highest. As the stress sensitivity of the fiber increases (with increasing *m*), the region over which fiber failure occurs most readily is limited to a smaller and smaller distance from the matrix crack. At 'low' values of α, the matrix modulus is much greater than the fiber modulus and the far-field stress is attained far

from the matrix crack plane. In this case, the probability of fiber failure is accurately represented by

$$q\left(\tilde{T}, l_s\left(\tilde{T}\right)\right) = 1 - e^{-\frac{1}{m+1}\tilde{T}^{m+1}} . \tag{48}$$

At 'high' values of α, the matrix modulus is 'small' relative to the fibers, (i.e. $E_c \approx fE_f$) and the far-field stress region defined in Figure 14 is reached very close to the matrix. In this case, the fiber stress is nearly constant, and failures will occur over the entire slip length. For the case of $\alpha = 1$, corresponding to a zero matrix modulus, the probability of fiber failure is

$$q\left(\tilde{T}, l_s\left(\tilde{T}\right)\right) = 1 - e^{-\tilde{T}^{m+1}} \tag{49}$$

Thus, the value of $m\alpha^{m+1}$ in Equation (47) ranges from 0 to 1 and represents the importance of the matrix modulus on the probability of fiber failure. The effect of the matrix contribution parameter, α, on fiber failure is shown in Figure 15. The region of constant failure probability represents the regime in which Equation (48) is an accurate representation of fiber failure.

The spatial location of the break with respect to the matrix crack, called the pullout length, is an important consideration. A break within one slip length of the matrix crack will carry a reduced, but possibly still significant, load at the matrix crack plane due to stress recovery as a result of the interface frictional stress. The mean failure location, $\langle L \rangle$, as a function of applied stress is given by the expression

$$\langle L \rangle = \frac{\int_0^{\sigma_{app}} \int_0^{l_s} z P_f\left(\sigma, 2l, z\right) dz d\sigma}{\int_0^{\sigma_{app}} \int_0^{l_s} P_f\left(\sigma, 2l, z\right) dz d\sigma}, \tag{50}$$

where $P_f(\sigma,2l,z)$ is the probability of fiber failure at position z, given by Equation (35). Although the denominator is $q(\sigma_{app},l_s)$, which can be replaced by Equation (47),

evaluation of the numerator must typically be perfomed numerically. Figure 16 shows the mean failure location at an applied stress equivalent to $\tilde{T} = 1$ for a variety of values of *m* and α. As this figure indicates, for low values of α and high values of m, fiber pullout is practically nonexistent. For low values of α where the fiber stress is constant over the fiber slip length the mean pullout length approaches one-half the slip length, which is the expected value for breaks distributed randomly over the slip length.

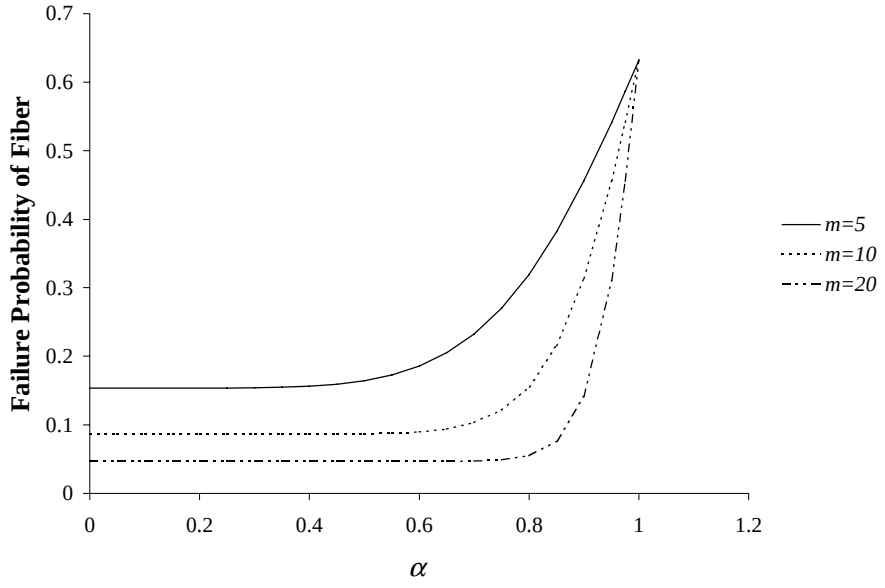

Figure 15. Probability of fiber failure as a function of matrix modulus at an applied stress of $\tilde{T} = 1$

Thus far, we have considered only the case of an isolated matrix crack. In real materials, matrix cracks typically exist with some variable spacing which depends on the properties of the constituents and the applied stress. If two adjacent cracks are spaced within two fiber slip lengths of each other, they will both affect the fiber stress as a function of position through the interface frictional stress as shown in Figure 17. In this case, the upper limit of the position integral will be limited to z_0, where z_0 is one-half the crack spacing.

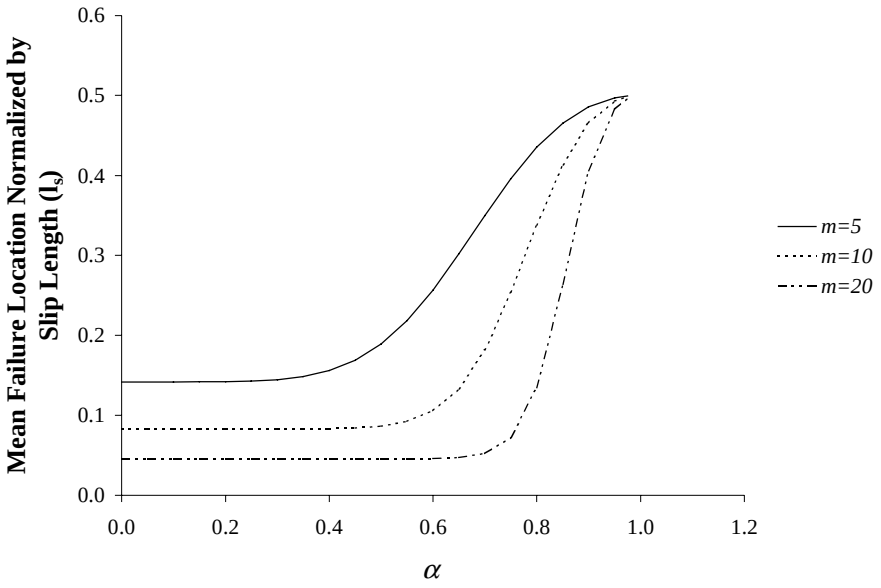

Figure 16. Average failure location for a single fiber as a function of matrix contribution

Analytically there are two possible cases, the first, which occurs when $l_s > z_0 \geq \delta(\sigma_{app})$ yields a probability of failure for the fiber of

$$P_f\left(T, z_0\right) = 1 - e^{-\left\{\frac{1}{m+1}\tilde{T}^{m+1}\left[1-\alpha^m\left((m+1)\frac{z_0}{l_s}-1-m(1-\alpha)\right)\right]\right\}} \tag{51}$$

In the second case, where $z_0 < \delta(\sigma_{app})$, the probability of failure is given by

$$P_f\left(T, z_0\right) = 1 - e^{-\frac{1}{m+1}\tilde{T}^{m+1}\left(1-\left(1-\frac{z_0}{l_s}\right)^{m+1}\right)} \tag{52}$$

As an example, the probability of failure of a fiber under an applied stress of $\tilde{T} = 1$ is shown in Figure 18 as a function of crack spacing. As with the results found for the pullout location, the fiber behavior is fairly insensitive to matrix crack spacing at high values of *m*. For narrowly spaced cracks, however, the crack spacing is important regardless of the value of *m*.

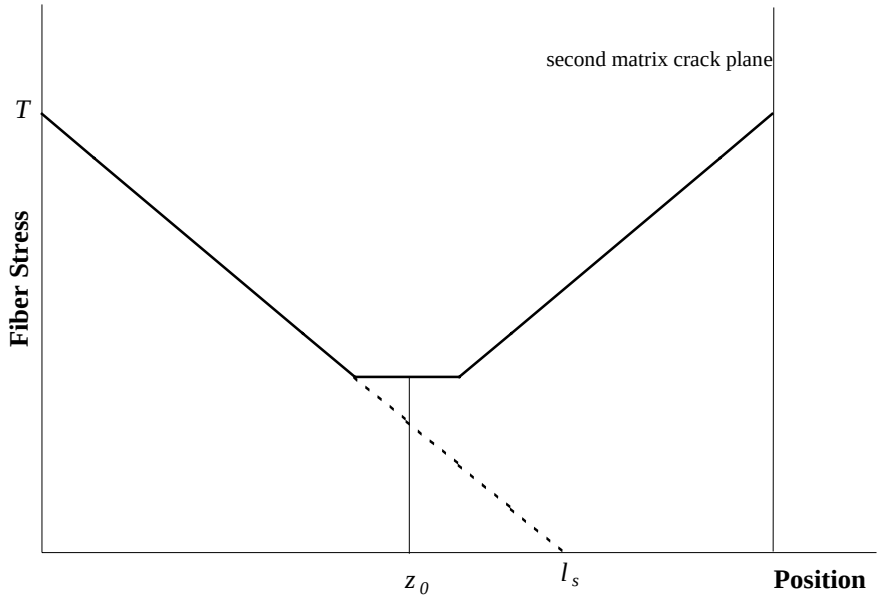

Figure 17. Fiber stress profile when two matrix cracks interact

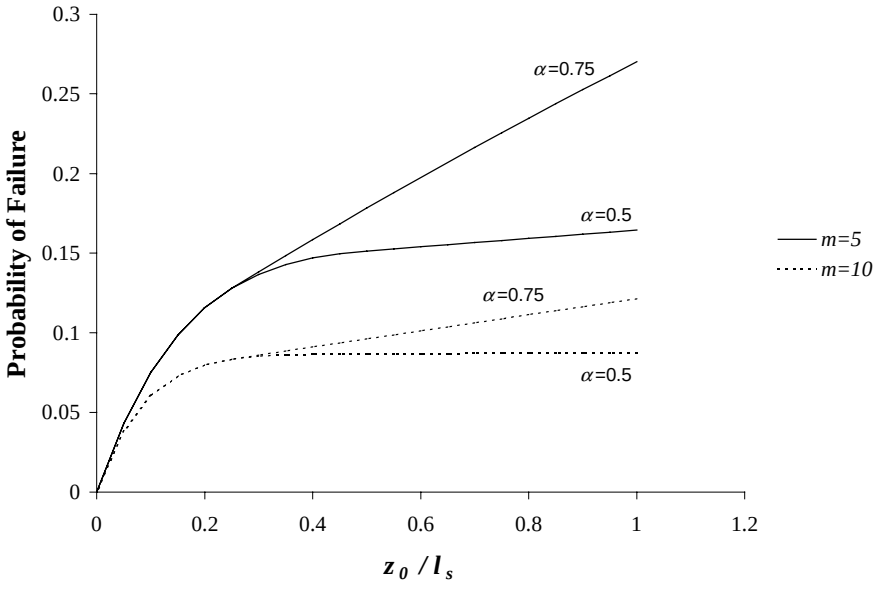

Figure 18. Probability of failure as a function of crack spacing

3.1.2 Fiber Time-Dependent Behavior

The mechanisms of degradation in alumina fibers has not been established, although stress rupture of monolithic alumina has been extensively studied (e.g. [61, 62, 63]). The general conclusion of these studies was that creep rupture in monolithic alumina is dominated by the formation and coalescence of cavities near the tip of pre-existing flaws at high stresses (approximately 22 ksi at 1150°). At lower stresses, crack blunting occurs and failure is due to the formation of creep cavities throughout the volume of the specimen. Given the temperatures and stresses used in the experimental program, slow crack growth is assumed to control the failure of the alumina fibers. The rate of crack growth follows a power law,

$$\frac{da}{dt} = CK^{\beta}, \tag{53}$$

where a is a crack size, K is the stress intensity factor at the crack tip, and β and C are constants which generally depend on temperature. Given that the stress intensity factor K is a function of stress σ and a geometric factor Y, behaving as

$$K = Y\sigma\sqrt{a}\,. \tag{54}$$

we can then rewrite the crack growth equation as

$$\frac{da}{dt} = CY^{\beta}\sigma^{\beta}a^{\frac{\beta}{2}}\,. \tag{55}$$

If we assume that the flaws which produce failure in quasi-static tension are the same flaws which grow under creep conditions to produce stress rupture, we can then relate the initial tensile strength (σ_i at a crack size a_i) to the flaw size at some later time, t. Given this assumption, we can combine equations (55) and (54) to produce the strength of the material as a function of t,

$$\sigma(t) = \left[\sigma_i^{\beta-2} - \left(\frac{\beta}{2}-1\right)CY^2K_{Ic}^{\beta-2}\int_0^t \sigma(t')^{\beta}\,dt'\right]^{\frac{1}{\beta-2}}. \tag{56}$$

Here we have assumed that the geometric factor Y is unchanged due to crack growth.

We can invert Equation (56) to find the initial strength required to provide a current strength of $\sigma(t)$ after the given stress history,

$$\sigma_i = \left[\sigma(t)^{\beta-2} + \left(\frac{\beta}{2} - 1 \right) CY^2 K_{Ic}^{\beta-2} \int_0^t \sigma(t')^{\beta} \, dt' \right]^{\frac{1}{\beta-2}} \tag{57}$$

Equation (57) can be normalized by introducing a non-dimensional time, $\tilde{t}$, given by

$$\tilde{t} = \frac{t}{CY^2 K_{Ic}^{\beta-2} \sigma_c^2 \left(\frac{\beta}{2} - 1 \right)}, \tag{58}$$

and a normalized stress, $\tilde{\sigma}$,

$$\tilde{\sigma} = \frac{\sigma}{\sigma_c}. \tag{59}$$

to yield

$$\tilde{\sigma}_i(\tilde{t}) = \left[\tilde{\sigma}(t)^{\beta-2} + \int_0^{\tilde{t}} \tilde{\sigma}(\tilde{t}')^{\beta} \, d\tilde{t}' \right]^{\frac{1}{\beta-2}} \tag{60}$$

If some stress history, $\sigma(t)$, is applied to a fiber, the probability that the fiber will fail is the probability that the initial strength of the fiber is less than the initial strength given by Equation (57). That is, for a fiber element of length δz, under some stress history, $\sigma(t)$, the probability of failure over the applied stress increment $\sigma(t)$ to $\sigma(t) + \delta\sigma(t)$, is obtained by substituting Equation (57) into Equation (28),

$$P_f(\sigma(t), z) = \frac{m \sigma_i^{m-1}}{l_0 \sigma_0^m} \delta z \delta \sigma_i \tag{61}$$

Following arguments identical to those used in the quasi-static case, we can produce the probability of failure of a fiber with respect to time under a position-independent stress history, $\sigma_{app}(t)$,

$$q(\tilde{\sigma}_i, \tilde{t}) = 1 - e^{-\int_0^{\tilde{\sigma}_i(\tilde{t})} \int_{-l_s}^{l_s} \frac{m}{\sigma_0^m l_0} \tilde{\sigma}'_i(\tilde{t})^{m-1} dz d\tilde{\sigma}'_i(\tilde{t})}, \tag{62}$$

which can be reduced to

$$q\left(\tilde{\sigma}_{app},\tilde{t}\right)=1-e^{\tilde{\sigma}_{app}(\tilde{t})\left[\tilde{\sigma}_{app}(\tilde{t})^{\beta-2}+\int_0^{\tilde{t}}\tilde{\sigma}_{app}(\tilde{t}')^{\beta}\,d\tilde{t}'\right]^{\frac{m}{\beta-2}}}. \qquad (63)$$

The failure probability of a fiber under a constant load $\tilde{\sigma}_{app}=0.5$ along the fiber length as a function of non-dimensional time for a variety of values for the parameters *m* and β is shown in Figure 19.

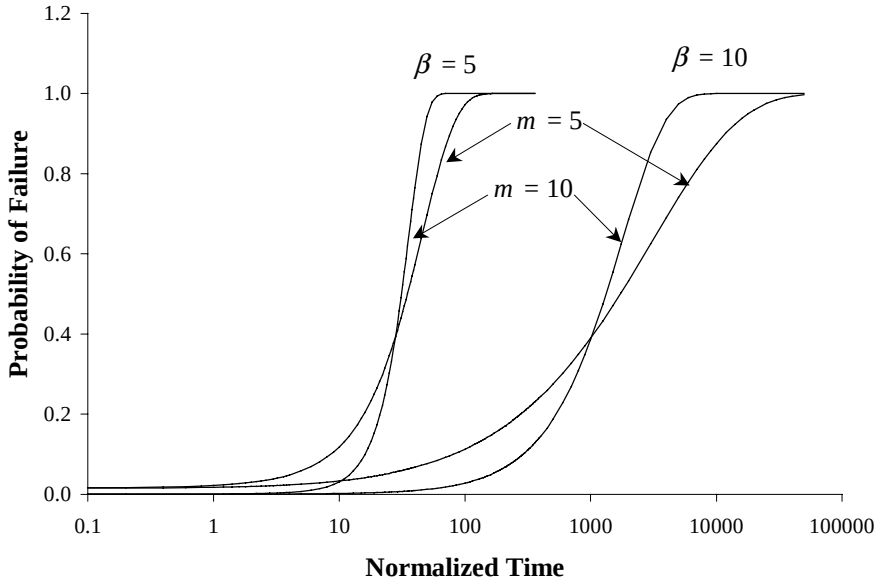

Figure 19. Probability of failure of a fiber under a constant load

Higher values of Weibull modulus, *m*, lead to narrower distributions in the initial fiber strength, corresponding to narrower distributions in failure time. Increasing the slow crack growth exponent, β, leads to wider lifetime distributions as well as much longer lifetimes.

Expressions similar to those derived previously which demonstrate the importance of parameters such as α and z_0 can be derived in the same fashion, although such equations must typically be solved numerically due to the complex interactions between position,

time, and stress. The probability of failure of a fiber as a function of time under the stress profile of Figure 14 is given by

$$q\left(\tilde{T},t\right)=1-e^{-2\left\{\int_0^{l_s}\frac{1}{l_0}\left[\tilde{\sigma}\left(\tilde{T},t,z\right)^{\beta-2}+\left(\frac{\beta}{2}-1\right)CY^2K_{Ic}^{\beta-2}\int_0^t\tilde{\sigma}\left(\tilde{T},t',z\right)^{\beta}dt'\right]^{\frac{m}{\beta-2}}dz\right\}} \tag{64}$$

where the order of integration has been reversed from the order used in the calculations performed previously and now the local applied stress $\tilde{\sigma}$ is a function of time as well as global stress and position. Figure 20 shows the effect of the parameter α on the probability of failure as a function of time for fibers under a constant load $\tilde{\sigma}_{app}=0.5$ with m = 5 and β = 5. As the contribution of the matrix increases (decreasing α), the fiber lifetimes increase, due to the overall decrease in fiber stress. This increase can exceed one order of magnitude, even at this moderate value of β. At low values of α, the fiber lifetimes are fairly insensitive to changes in α. Since the majority of fibers will fail near the crack plane, the additional decrease in fiber stress far from the crack plane at low values of α has an insignificant effect.

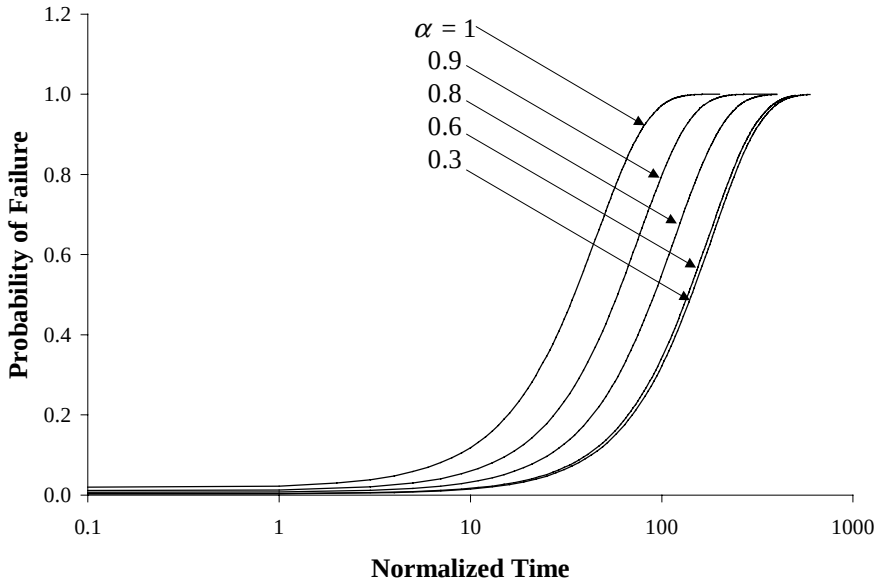

Figure 20. Effect of matrix modulus on fiber lifetime

As with the quasi-static case, the effect of crack spacing can be considered by changing the limits of integration in Equation (64). These equations will not be reproduced, as the trends are similar to those described previously.

3.2 Composite Behavior

Having discussed the behavior of a single fiber under a variety of stress profiles for both quasi-static and time-dependent behavior, we now turn to the behavior of a composite, which typically consists of a statistically large number of fibers. In a well designed ceramic composite, broken fibers transfer stress to other intact fibers in the plane through friction at the fiber/matrix interface, increasing the load on the remaining fibers. The equations of fiber failure discussed in the previous section are used and combined with load sharing laws, which determine how the load is transferred, to yield predictions of composite behavior. The simplest and most analytically tractable load sharing law is global load sharing, where the stress which was previously carried by broken fibers is shared equally among all other intact fibers in the plane. Global load sharing is used in all models discussed in this section.

3.2.1 Tensile Strength

To extend the behavior of single fibers to the behavior of a composite, the interactions between broken and unbroken fibers must be considered. In a composite, mechanical equilibrium must be maintained at all planes perpendicular to the applied load. Equilibrium at a matrix crack plane can be stated as a straightforward load balance relationship between the broken and intact fibers

$$P_{broken\ fibers} + P_{unbroken\ fibers} = P_{app}\,. \tag{65}$$

The applied load is known *a priori*, and is given by

$$P_{app} = \sigma_{app} A_{fiber} N_{fiber}, \tag{66}$$

at the matrix crack, where A and N are the area of a single fiber and the number of fibers in the composite respectively.

The load carried by an individual broken fiber at a matrix crack will depend on the distance from the fiber break to the matrix crack

$$\sigma_f = \frac{2\tau z}{r}, \tag{67}$$

where z is the distance from the fiber break to the matrix crack. The distance over which the fiber stress is less than the far-field value is the fiber slip length, l_s. If the matrix cracks are spaced at a distance less than l_s, a fiber break can affect the stresses on intact fibers over more than one matrix crack. Consider a 'central' matrix crack which is the location of the ultimate composite failure. For a crack spacing of z_0, the number of matrix cracks in either direction which affect the stresses on the central matrix crack through fiber breaks is l_s/z_0. At each crack, the number of broken fibers can be found by considering Equations (51) or (52), depending on the crack spacing. At each matrix crack plane, the fiber stress is symmetric about the matrix crack, so the resulting fiber breaks will be distributed symmetrically about the matrix crack as well. Given this, the average distance from the central matrix crack to the fibers broken about a second matrix crack will be the distance between the two cracks. The matrix cracks themselves are assumed to be evenly spaced on both sides of the central matrix crack, so the average distance from the central matrix crack to the other matrix cracks which affect the central crack will be $l_s/2$. The pullout from the central matrix crack must, however, be handled separately.

The equilibrium expression can then be re-written as

$$\frac{\sigma_{app}}{f} = q(T)\frac{2\tau\langle L\rangle_0}{r} + q(T)\frac{2l_s}{z_0}\frac{2\tau}{r}\frac{l_s}{2} + \left[1 - q(T)\left(1 + \frac{2l_s}{z_0}\right)\right]T, \tag{68}$$

where $<L>_0$ is the pullout from the central crack plane. The first term represents pullout from the central matrix crack. Pullout from the $2l_s/z_0$ other matrix cracks is represented by the second term. The stress carried by the fibers which remain intact is represented by the third term.

As discussed in the previous section, the percentage of fibers that are broken and the mean distance from the fiber break to the matrix crack can be found as a function of applied stress on the fibers, T, through Equations (47) and (50), for example. For the single fiber case discussed previously, $T = \sigma_{app} / f$, but in a composite, T must be determined by maintaining equilibrium in the composite while accounting for the stress carried by broken and slipping fibers. Equation (68) is then solved for T as a function of σ_{app}. When no solutions exist, the composite cannot satisfy equilibrium, and the lowest value of σ_{app} at which this occurs is the tensile strength of the composite. The composite strain will be the strain of the intact fibers, or T/E_f, so Equation (68) can be used to determine the stress-strain response of a composite specimen with arbitrarily spaced matrix cracks.

Due to the complicated nature of the pullout term, $<L>_0$, Equation (68) must in general be solved numerically. If this term is ignored, an assumption which is applicable when pullout lengths are short, (i.e. the fibers fail near a crack plane or the crack spacing z_0 is very small) then simpler solutions exist. This is the case considered by Curtin, Ahn, and Takeda (CAT Model) [25], where Equation (68) is reduced to the form

$$\frac{\sigma_{app}}{f} = \left[1 - q(T)\left(1 + \frac{T\delta_c}{2\sigma_c z_0}\right)\right]T \; . \tag{69}$$

As this method of analyzing the tensile response of a composite has been discussed quite thoroughly in the literature [25], the extension of the model to time-dependent strength will now be discussed.

3.2.2 Time-Dependent Strength

The concepts used to determine the tensile strength of a composite can be directly transferred to the determination of its time-dependent strength. Equation (68) for composite equilibrium must be solved as a function of time, with failure occuring when no solutions exist. The fraction of broken fibers is determined through the use of Equation (64). These two equations must be solved simultaneously to find T as a function of time.

As fibers break and the stress on the intact fibers increases, the result is a complex stress history on the intact fibers. This stress history makes analytic determination of the fraction of broken fibers impossible for general cases. Additionally, as the intact fiber stress, T, increases, there is a corresponding change in the fiber slip length. Thus, the limits on the position integral in Equation (64) are functions of time.

Two possible solutions to these problems are proposed. First, approximations regarding the stress history can be made which yield expressions which can be evaluated, albeit numerically. Second, a *single fiber simulation* approach can be used, where the stress history on the intact fibers in the composite is considered at a number of points along a generic intact fiber. The generic fiber is analyzed to determine the probability of fiber failure and correspondingly the stress carried by the remaining intact fibers.

In both methods an iterative process will be used, where the time is incremented, then the values of q and T are found using the appropriate equations. Once the equilibrium state has been determined, time is incremented again. This procedure is repeated until composite failure occurs, which is when no solutions to Equation (68) exist.

For the first method, it is necessary to keep a running total of the value of ρ, a damage parameter, where

$$\rho = \int_0^{\tilde{t}} \tilde{\sigma}\left(\tilde{t}\,'\right)^{\beta} d\tilde{t}\,',$$

although strictly, in this method, this is a sum over the N timesteps taken

$$\rho = \sum_{i=1}^{N} \tilde{T}^{\beta} dt_i \ . \tag{70}$$

This value, ρ, represents the time-dependent degradation of the fiber strength. Given a position dependent stress (Equation (40)), the value of the damage parameter is multiplied by the *position factor*

$$\begin{matrix} \left(1-\dfrac{x}{l_s}\right)^{\beta}, & |x| < \delta \\ \left(\dfrac{E_f}{E_c}\right)^{\beta}, & \delta < |x| < l_s \end{matrix} \tag{71}$$

to determine the degradation as a function of position. Strictly, this position factor, Equation (71), should be included in the damage parameter, and the damage parameter should be a function of position. However, as an approximation, the position factor is determined using the slip length determined by the current value of intact fiber stress, *T*. Thus, for a fiber in a composite with $\alpha = 1$ and isolated matrix cracks ($z_0 > 2l_s$), the failure probability for the fibers is then

$$P_f\left(\tilde{T},t\right) = 1 - e^{\int_{-l_s}^{l_s} \frac{1}{\delta_c}\left[\tilde{T}^{\beta-2}\left(1-\frac{x}{l_s}\right)^{\beta-2} + \rho\left(1-\frac{x}{l_s}\right)^{\beta}\right]^{\frac{m}{\beta-2}} dx} \ . \tag{72}$$

Similar expressions are derived for composites with interacting matrix cracks or different values of α. This technique overstates the stress history along the fiber, but requires only a single parameter, ρ, to represent the entire stress history of the composite. For composites in which failure is expected close to the matrix crack (high values of $m\alpha^{m+1}$, for example), this assumption is very accurate.

The second method is a hybrid of analysis and simulation. A generic fiber with the properties of the fibers in the composite is divided into *M* elements. The fiber length is chosen such that it exceeds the maximum expected slip length. For the simulations performed in this work, the simulated fiber length was set equal to the fiber slip length at a stress of $\tilde{T} = 2$. The global applied stress on the composite is applied to the fiber and the local stress on each fiber element is determined. The probability of failure at each position can then be readily determined using the fiber Weibull and degradation parameters and the specific element stress history. The probability of failure of the fiber will then be

$$P_f = 1 - e^{-\sum_{i=1}^{N} P_{f_i}}, \tag{73}$$

where P_{fi} is the probability of failure of the *i*-th fiber element. The elements are summed over the *N* elements which fall within the slip length, although those fiber elements outside the slip length are allowed to degrade, in anticipation of a longer slip length at a later time.

The difference in predicted lifetime between these two methods will be a function of the changes in *T* before failure occurs and of the stress sensitivity of the fibers. If, for example, the final failure process begins while *T* is fairly close to its initial value (at time zero), then the difference between the two methods will be small. If there is a change in *T*, but the stress sensitivity is low, then the consequences of ignoring the change in slip length will also be minor.

The composite stress-rupture lifetimes as a function of stress depend on many parameters: m, C, β, α, σ_c, τ, and z_0. Understanding the effects of these parameters on the stress-rupture lives of composites is important in terms of attempting to improve composite properties through altering the constituents. Due to the complicated stress histories on intact fibers in composites and the load sharing from broken fibers, the trends in composite lifetime may not follow the trends in the lifetimes of the single fiber. While

the relationship between the normalized time used in the lifetime equations and real-world time is dependent on other parameters (namely, σ_c, K_{Ic}, and C), this dependence will not be considered, as the scaling is straightforward in this case.

The Weibull modulus, m, affects the distribution of failure times of single fibers, as shown in Figure 19. In the composite, decreasing m results in an increase in failure time, as shown in Figure 21, although over the range of m usually seen in ceramic reinforcing fibers, ($3 < m < 12$) the change in lifetime is minimal.

The slow crack growth exponent, β, affects the lifetimes of the single fibers – increasing β increases the mean failure time. The same effect occurs in the composite as shown in Figure 22. This parameter has a very large effect on composite lifetime – several orders of magnitude in life can be obtained by only slight changes in β.

The effect of the matrix parameter α is to increase the failure times of a single fiber. In the composite, however, the lifetimes are unaffected by changes in α, as shown in Figure 23. While increasing α increases the single fiber lifetime, it also acts to increase the tensile strength of the composite. These two effects are balanced in the composite, so while the absolute lifetimes for a given stress are shorter for smaller α, when plotted relative to tensile strength, there is no effect. The lifetimes plotted relative to the fiber characteristic strength are shown in Figure 24 and demonstrate that there is an absolute increase in lifetime for larger α.

The ratio of the crack spacing, z_0, and the characteristic length, δ_c, affects the lifetime in a similar fashion as α. Results are shown in Figure 25. As with Figure 24, the stresses have been normalized with respect to the characteristic strength, and the curves collapse if normalized to the tensile strength.

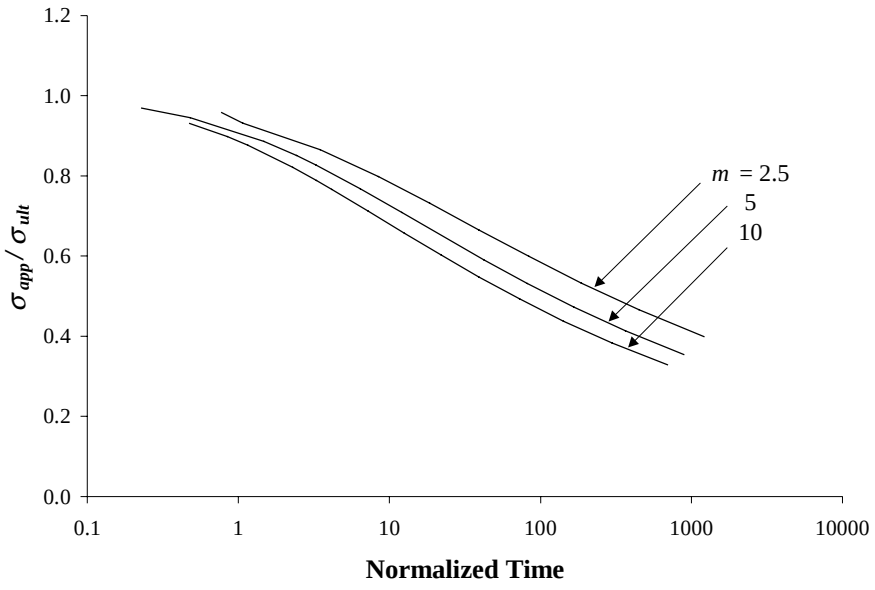

Figure 21. Effect of Weibull modulus, *m*, on composite lifetime (β = 5, α = 1)

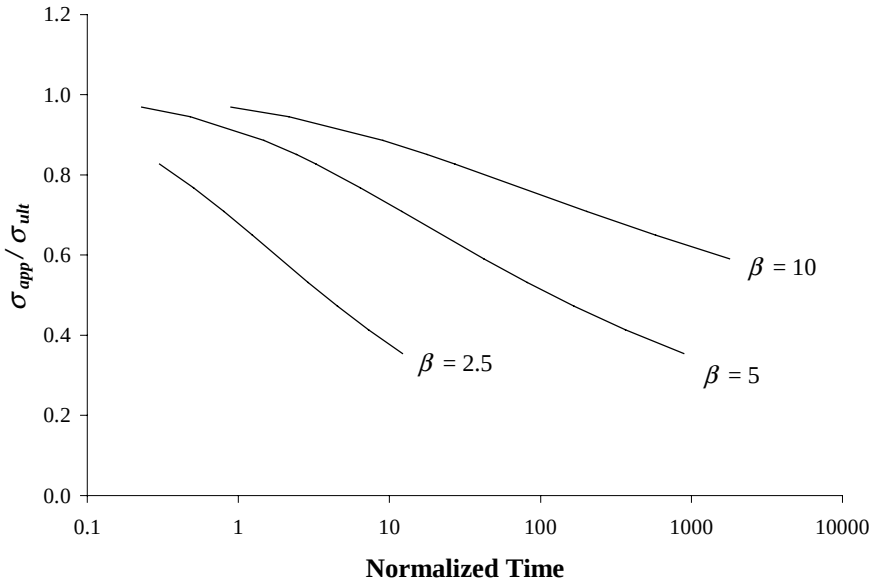

Figure 22. Effect of β on composite lifetime (*m* = 5, α = 1)

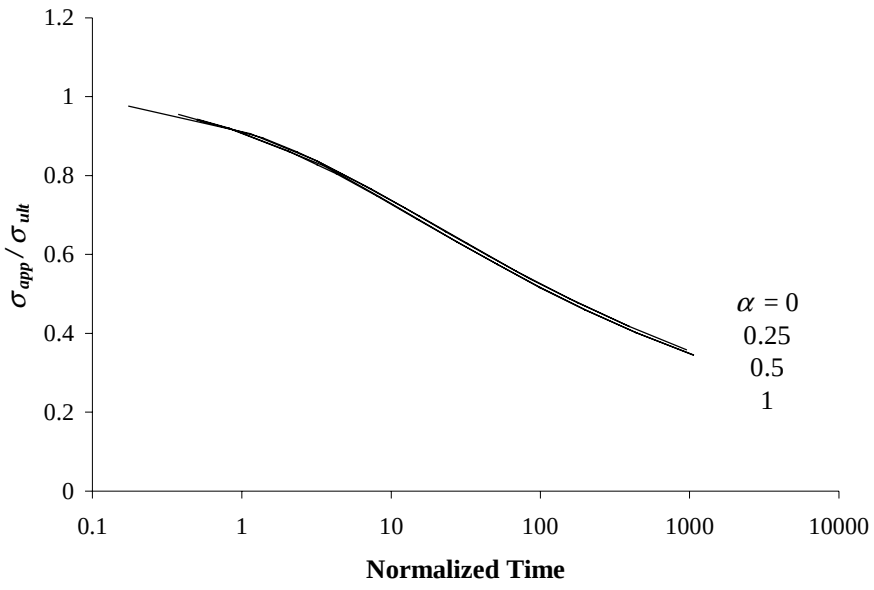

Figure 23. Effect of α on composite lifetime (m = 5, β = 5)

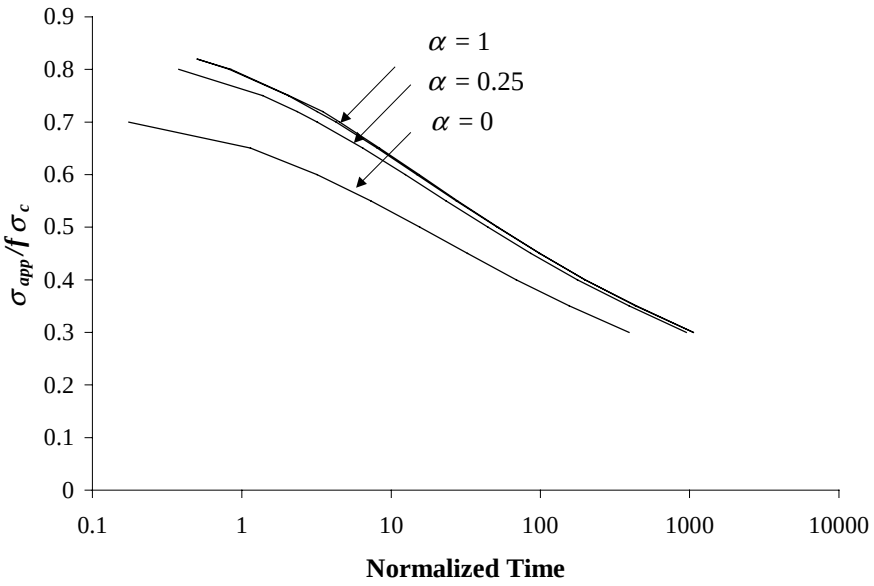

Figure 24. Effect of α on composite lifetime (m = 5, β = 5)

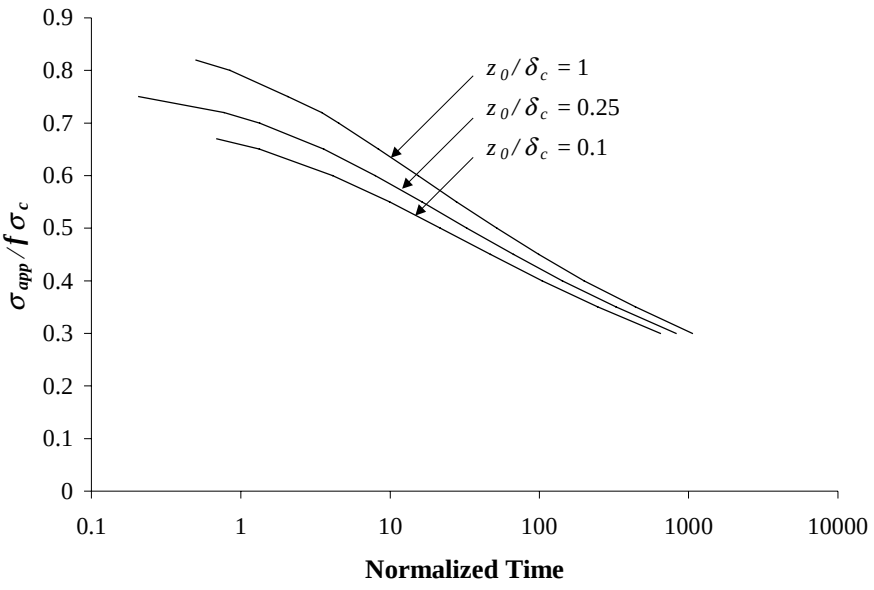

Figure 25. Effect of crack spacing on composite lifetime (m = 5, β = 5)

Thus far, the effect of creep deformation on the stress-rupture lifetime has not been considered. In tension, the matrix contribution can be characterized by the ratio of the elastic constants,

$$\alpha = \frac{fE_f}{E_c}, \tag{46}$$

which is used to determine the far-field fiber and matrix stresses. Another definition for α is

$$\alpha = 1 - \frac{\delta}{l_s}, \tag{74}$$

which is equivalent to Equation (46) when the composite is in tension. When the fibers and the matrix behave in a viscoelastic manner, however, the far field fiber and matrix stresses are determined by the equality of the strain *rates*, not the absolute strains. That is,

$$\dot{\varepsilon}_m = \dot{\varepsilon}_f$$
$$\frac{\dot{\sigma}_m}{E_m} + B\sigma_m^n = \frac{\dot{\sigma}_f}{E_f} + H\sigma_f^p, \tag{75}$$

where the fiber and matrix strain rates are assumed to follow a power-law relationship. The fiber and matrix stresses must satisfy equilibrium

$$f\sigma_f + (1-f)\sigma_m = \sigma_{app}. \tag{76}$$

Substitution of Equation (75) into Equation (76) will yield the change in fiber stress in the far-field as a function of time

$$\frac{d\sigma_f}{dt} = \frac{(1-f)E_f E_m}{E_c}\left[B\left(\frac{\sigma_{app} - f\sigma_f}{1-f} \right)^n - H\sigma_f^p \right]. \tag{77}$$

The initial fiber far-field fiber stress at time $t = 0$ will be governed by the quasi-static response of the constituents, and the subsequent changes are governed by Equation (77). A steady state is reached when the fiber stress is constant with time, i.e. when

$$B\left(\frac{\sigma_{app} - f\sigma_f}{1-f} \right)^n - H\sigma_f^p = 0 \tag{78}$$

As the far-field fiber stress changes, the length of the fiber slip zone will change as well, thus affecting the failure probability of the fiber and the composite strain rate. This is shown schematically in Figure 26, where the initial quasi-static fiber stress profile is altered due to creep deformation. In the case shown, the far-field fiber stress increases under creep deformation, implying that the matrix carries less stress in creep than in quasi-static tension. This has the effect of increasing both the rate of fiber degradation and the strain rate of the composite.

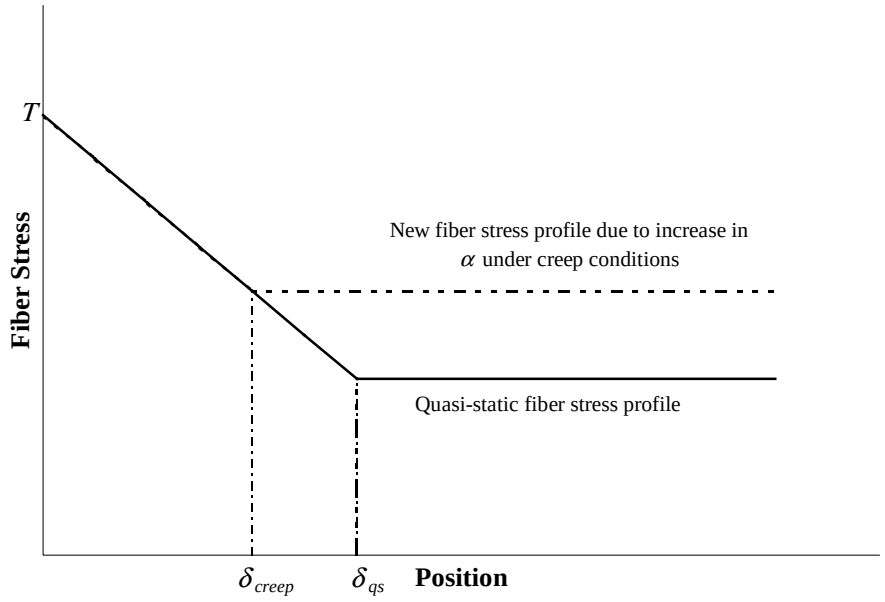

Figure 26. Change in fiber far-field stress due to creep deformation

The overall composite strain rate is found by integrating the strain rate of the fiber over one-half of the crack spacing

$$\dot{\varepsilon}_c = \int_0^{z_0} \dot{\varepsilon}_f(z)\, dz\,. \tag{79}$$

The fiber strain rate is a function of the applied stress, which in turn is a function of position. Therefore, Equation (79) can be stated as

$$\dot{\varepsilon}_c = \int_0^{\delta} B\left[T\left(1-\frac{z}{l_s}\right)\right]^n dz + \int_{\delta}^{z_0} B\sigma_{ff}^n\, dz\,, \tag{80}$$

where the far field fiber stress, σ_{ff}, is determined from Equation (77) and δ can be determined by fitting the strain rate obtained from Equation (80) to the experimentally measured strain rate. The parameter α can then be found using Equation (74).

It is possible that the shear stress at the interface can be affected by creep of the constituents (e.g. Iyengar and Curtin [34]). In this case, the characteristic length, δ_c, will change. This can have a large effect on the degradation of the composite, but cannot be

determined without testing the composite directly. This topic will be discussed in the seventh chapter.

One advantage to this method of predicting stress-rupture lifetime and creep deformation is that it can be truly predictive. The parameters required to generate stress-rupture predictions are

1. The single fiber rupture parameters (C and β),
2. The fiber characteristic strength in the composite (σ_c),
3. The fiber Weibull modulus (m),
4. The interface frictional stress (τ),
5. The matrix contribution (α), and
6. The crack spacing (z_0).

The parameters C, β, and m can be found from single fiber tension and stress rupture tests. The parameters z_0, τ, and σ_c can be found from tension and hysteresis tests on the composite. The matrix contribution α can be determined from an analysis of creep deformation tests on the fibers and on the matrix material. With this information, true predictions of stress-rupture lifetimes and creep deformation can be made prior to any composite stress-rupture testing. In the fifth chapter, these necessary parameters will be determined from the literature and from experiments performed on a Nextel 610/alumina-yttria composite. The model detailed in this chapter will then be compared to stress rupture lifetimes and creep deformation rates obtained experimentally.

Chapter 4 Experimental Methods

4.1 Material System

The material examined is an oxide/oxide CMC produced by McDermott Technologies, Inc. (MTI) of Lynchburg, VA. This material consists of Nextel 610 fibers (>99% Al_2O_3) aligned in a hybrid alumina-yttria matrix with a fugitive carbon interface. A small sample of materials with the fibers woven in an eight-harness satin weave was also provided.

These materials are fairly unique in that they are produced with no bond between the fiber and the matrix. This is done by coating the fibers with a thin (80-100 nm) layer of carbon through an immiscible liquid coating process before processing the matrix. After the matrix has been added the carbon is oxidized, leaving a small gap between the fiber and the matrix. It is hoped that this gap will be large enough to prevent large-scale sintering of the materials at elevated temperatures, but small enough to permit the stress transfer between the constituents necessary for optimal composite properties. The carbon also serves to protect the fiber from any adverse chemical reactions during the process which creates the alumina-yttria matrix.

To create the matrix, a slurry of alumina powder is first pressure cast into the fiber preform. Next a sol of yttria particles is infiltrated into the preform, and the preform is dried at 700°C. After a few infiltration and drying steps, the part is fired at 1100°C for approximately one hour. The infiltration/drying/firing cycle is then repeated until the desired density is reached, typically four to six cycles. For these materials, processing was halted when the composite porosity was approximately 20%. The yttria reacts with the alumina during the firing cycle to create $AlYO_3$ and $Y_3Al_5O_{12}$. The exact composition of the matrix is unknown, and samples of the matrix cannot be provided as the matrix cannot be produced without the fibers to serve as a structure.

A list of the panels received, the weights during processing, and the density as measured by Archimedes' Technique reported by MTI is given in Table IV. A total of eighteen panels were received totaling 89 specimens. Fourteen 3-ply woven materials were received.

Table IV : Panel Properties as Reported by MTI

Panel No.	Fiber Wt. (g)	Weight After Powder Processing (g)	Wt. After Sol Processing (g)	Percent Porosity
1	38.11	66.851	73.657	16.92
2	38.09	71.649	77.866	19.92
3	38.32	92.912	102.578	25.34
4	34.42	88.122	96.332	26.05
5	36.78	91.966	102.893	26.07
6	38.22	60.215	64.720	22.13
7	38.26	59.037	64.550	22.02
8	38.56	57.152	63.866	21.01
12	39.42	57.815	61.535	19.34
13	39.10	55.879	60.149	18.71
14	39.50	54.802	59.538	18.15
15	40.05	59.046	64.755	20.31
16	40.44	58.322	62.272	16.52
17	38.42	54.402	59.606	19.94
18	39.04	57.290	61.993	21.00
19	38.46	56.776	61.204	20.93
20	38.94	56.584	60.954	21.01
21	39.95	63.560	67.912	18.50
22	39.10	60.534	64.584	17.38
23	39.24	64.298	67.385	17.32

4.2 Mechanical Testing

The unidirectional material will be used for quasi-static and stress-rupture testing at four temperatures: 23°C, 950°C, 1050°C, and 1093°C. The woven material will be tested at 1093°C. The planned test matrix is shown in Table V.

4.2.1 Quasi-Static Testing

Quasi-static testing was performed on an MTS[3] 880 test frame with an MTS 458 controller. The specimens were tabbed with 0.020" fully annealed aluminum tabs to prevent damage from gripping. The aluminum tab was placed around the end of the specimen and the specimen was placed in the MTS grip. The pressure of the grip plastically deformed the aluminum to 'fit' the specimen and no adhesive was used. Grip pressures were kept at approximately 100 psi. The tests were run in load control at a rate of 40 lbf/s. Strain at room temperature was measured with an MTS extensometer (Model 632-11B). Specimen alignment was maintained through a fixture at the grips. The alignment was checked before each set of tests was run.

For the elevated temperature tests, a compact oven was used (Figure 27). The oven has four silicon carbide resistance elements which heat the specimen[4]. The oven shell is stainless steel and has dimensions 3.5" high x 3" x 3". Fused silica insulation[5] lines the inside of the oven, reducing the interior dimensions to 2.5" x 2" x 2". Two temperature

[3] MTS Systems, Inc., Minneapolis, Minnesota

[4] Norton Advanced Ceramics, Worcester, Massachusetts

[5] Cotronics Corporation, Brooklyn, New York

controllers[6] control the silicon carbide elements, one for the two upper elements and one for the two lower elements. Each controller recieves input from a type R (platinum/platinum-rhodium) thermocouple.

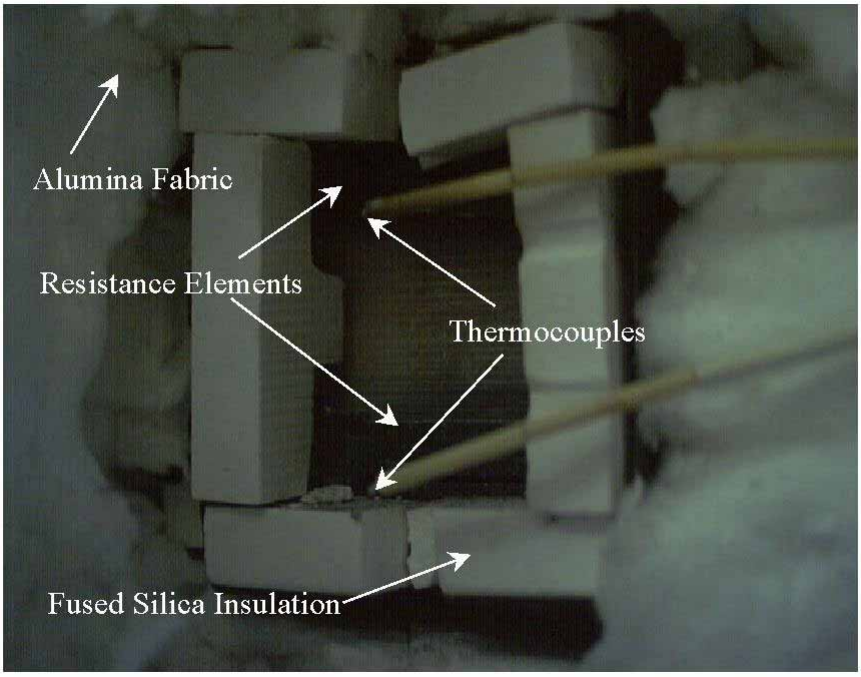

Figure 27: High temperature oven used for experimental study

Table V: Test Matrix

Test	Temperature	# of Tests
Quasi-Static Tensile	23°C	5
Quasi-Static Tensile	950°C	5
Quasi-Static Tensile	1050°C	4

[6] Eurotherm model 818S, Eurotherm, Reston, Virginia

Quasi-Static Tensile	1093°C	2
Hysteresis Loop	23°C	3
Hysteresis Loop	950°C	2
Hysteresis Loop	1050°C	2
Stress-Rupture – 37.5 ksi	950°C	5
Stress-Rupture – 30 ksi	1050°C	5
Stress-Rupture – 17 ksi	1093°C	3
Stress-Rupture – 42.5 ksi	950°C	5
Stress-Rupture – 37.5 ksi	1050°C	5
Stress-Rupture – 21.5 ksi	1093°C	3
Stress-Rupture – 45 ksi	950°C	4
Stress-Rupture – 42.5 ksi	1050°C	4
Stress-Rupture – 26 ksi	1093°C	4
Stress-Rupture – 42.5 ksi – 50% of Life	950°C	2
Stress-Rupture – 30 ksi – 50% of Life	1050°C	2
Stress-Rupture – 42.5 ksi – 75% of Life	950°C	2
Stress-Rupture – 30 ksi – 75% of Life	1050°C	2
Stress-Rupture – 45 ksi – 50% of Life	950°C	2
Stress-Rupture – 37.5 ksi – 50% of Life	1050°C	2
Stress-Rupture – 45 ksi – 75% of Life	950°C	2
Stress-Rupture – 37.5 ksi – 75% of Life	1050°C	2
Woven Quasi-Static	1093°C	4
Woven Stress-Rupture	1093°C	8

The oven shell is surrounded by alumina fabric insulation[7] for efficient heating and to help maintain a constant temperature. A heat shield attached to the oven holds the

[7] Cotronics Corporation, Brooklyn, New York

extensometer (MTS model 621-51E). The extensometer measures strain according to the deflection of two 5” alumina rods which pass through the oven shell and contact the specimen. The entire assembly is attached to the test frame at one of the posts. The extensometer, the heat shield, and the MTS grips are cooled by water.

For a high temperature test, the temperature is ramped at a rate of 33°C/s to the desired test temperature. The temperature is then held constant for 10 minutes before the test begins to ensure thermal equilibrium.

4.2.2 Hysteresis Loop Testing

Hysteresis loop tests at room and elevated temperatures were run in a manner rather similar to the quasi-static tests. However, for the hysteresis tests, the load was cycled from zero to 100 lbf and back to zero, then 0-200-0, 0-300-0, and so forth until failure occurred. The load rate was kept constant at 40 lbf/s.

4.2.3 Stress-Rupture Testing

The stress rupture testing proceeds similarly to the quasi-static testing. However, the load rate for the stress-rupture tests was set to 150 lbf/s. This was done to minimize creep effects during the initial loading ramp. Once the desired load was reached, it was held constant until failure occurred. Strain data was collected throughout the test.

Some tests were stopped after specified times for residual strength tests. For a residual strength test, the load was returned to zero, then the specimen was ramped to failure at 40 lbf/s.

4.3 Microscopy

Selected specimens from a variety of panels will be examined before any mechanical testing is performed. The volume fraction of these specimens will be determined through optical examination, and any damage caused by processing will be evaluated through microscopy.

The technique for determining the volume fraction of a specimen is straightforward. A small piece of the sample is removed, potted in epoxy[8], and polished using successively finer diamond paste (to approximately 1μ). The specimen is then examined under an optical microscope. An area approximately 2 mm x 1.5 mm is photographed. The number of fibers contained in the photograph is determined, and an average fiber size is also found. From this information and the size of the photograph, the volume fraction of the specimen can be found. Due to the lack of optical contrast between the fibers and the matrix, computer-assissted techniques were insufficient for this task, although the images were scanned into a computer to allow more accurate dimensional measurements.

Scanning electron microscopy (SEM) was also used on virgin specimens. Specifically, the existence of matrix cracking due to residual stresses from processing was determined. This was also performed on potted and polished specimens

Failed specimens were also examined through SEM. Scanning electron microscopy of failed fiber surfaces can often reveal information about the strength of the fiber through the analysis of 'fracture mirrors' [21,64]. This was attempted on specimens tested at room temperature and elevated temperature. The existence of a sufficient number of fracture mirrors allows more accurate determination of the fiber Weibull strength

[8] Epoxide system, Buehler, Lake Bluff, Illinois

properties and their change with time and temperature. Previous researchers have had little success in observing fracture mirrors on Nextel fibers [65], but an attempt must be made, as it is the only direct method by which fiber properties after testing and/or processing can be determined for these materials.

Examination of the fracture surface yields a measurement of the distribution of pullout lengths. When combined with the fracture mirror strength measurements, this distribution is used to determine the interface frictional stress at the time of failure. This can also be correlated with hysteresis analysis of specimens tested for residual strength.

If matrix cracks exist, their spacing is determined by the interface frictional stress, yielding another measure of this property. Their existence (or non-existence) also has an effect on the stresses carried by the fibers. This may have a significant effect on the strain rate of the composite, especially since the fiber strain rate is extremely sensitive to the applied stress, as indicated by Equation (27). The pre- and post-test measurements yields information about the evolution of matrix cracks with time, temperature, and stress.

Microscopy of the interface will also be performed. Initially, there should be a gap between the fiber and the matrix where the fugitive interface has oxidized away. After exposure to temperature, this gap may have closed due to changes in the structure of the constituents. This also will have implications for the magnitude of the interfacial frictional stress.

Chapter 5 Experimental Results and Discussion

The results obtained from the experimental program are discussed in this chapter. In the first section, the results from the examination of untested specimens will be presented. Specifically, the fiber volume fraction will be determined and any matrix damage will be quantified. This information will establish the initial state of the material. The results from the quasi-static test program will then be presented and analyzed to determine important composite parameters, such as fiber characteristic strength, fiber/matrix interface frictional stress, and the constituent moduli. The stress-rupture experimental results will then be discussed in the context of both simple models presently used and the model described in Chapter 3.

5.1 As-Received Specimens

5.1.1 Fiber Volume Fraction and Matrix Porosity

A calculation of fiber volume fraction was performed for the unidirectional composites based on the weights of alumina and yttria added during processing, the densities of alumina and yttria (3.97 g/cm^3 and 5.03 g/cm^3 respectively), and the measured composite porosity. The fiber volume fraction, *f*, is

$$f = \frac{(1 - f_p)V_f}{\left(V_f + V_m\right)}, \tag{81}$$

where *V* represents the volume of the fiber and of the matrix and f_p is the porosity fraction of the composite. Any reaction between the alumina and yttria which might produce species of different densities is ignored in performing this calculation. In order to verify these calculation, microscopic examination of polished cross-sections was performed on several unidirectional panels. A photograph of a cross-section of specimen 23-4 is shown

in Figure 28. The field of view in this photograph contains approximately 250-300 fibers and is typical of the cross-sections examined for fiber volume fraction determination. The results of the density measurements and the optical measurements are given in Table VI. There is good agreement between the two methods for most of the panels examined and the two methods do not form a consistent pattern where the results from one method are higher than from the other. In some of the specimens examined, there was poor fiber distribution in the cross-section which might cause difficulty in optical measurements of fiber volume fraction. A specimen from panel 5, where the uneven distribution is evident, is shown in Figure 29. Based on the good correlation between the two methods, the fiber volume fractions were set at 27.5% for panels 3-5 and at 51% for panels 6-23 for further analysis.

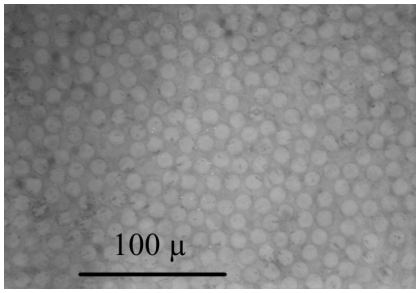

Figure 28. Specimen 23-4 cross section for fiber volume fraction measurement

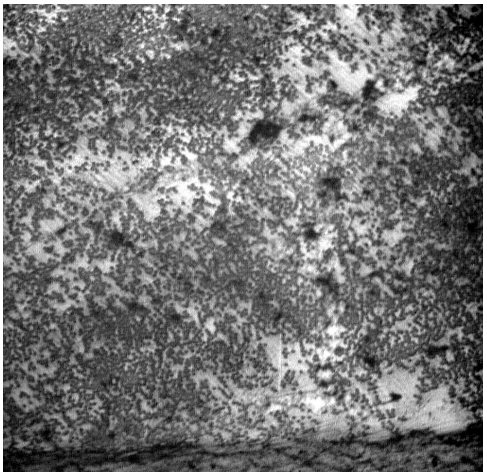

Figure 29. Poor fiber distribution in specimen cross-section

Table VI. Fiber volume fraction from density measurements and optical technique

Panel No.	Fiber Volume Fraction (density)	Fiber Volume Fraction (optical)	Relative Error (%)
1	43.9	43.6 ± 7.0	0.6
2	39.9	38.1 ± 7.1	4.5
3	28.5	--	--
4	26.9	26.2	2.6
5	27.1	32.7 ± 1.2	20.7
6	46.7	40.3	13.7
7	47.1	53.1	10.6
8	48.8	--	--
12	52.4	48.4 ± 7.1	7.6
13	53.7	--	--
14	55.3	--	--
15	50.3	49.2 ± 1.2	2.2
16	55.0	--	--
17	52.6	--	--
18	50.6	51.2 ± 1.9	1.2
19	50.5	--	--
20	51.3	54.7	6.6
21	48.6	--	--
22	50.7	--	--
23	48.6	55.4	14.0

The matrix porosity was calculated directly from that measured by MTI and given in Table IV. The average composite porosity for panels 6-23 was 19.6%, which translates to a matrix porosity of 40% with a matrix volume fraction of 49%. For panels 1-5, the matrix porosities were slightly lower, at approximately 33%.

The processing parameters were not provided for the woven materials so only optical fiber volume fraction measurements were performed. A sample cross-section of the microstructure of the woven composite is shown in Figure 30. The measurements on the tow and composite are given in Table VII and a schematic of the woven cell illustrating the definitions of these measurements is shown in Figure 31. If the tows are assumed to be elliptical in cross section, the overall fiber volume fraction in the axial direction can be determined:

$$f_{axial} = \frac{f_{tow}\left(\pi \frac{a}{2}\frac{h_t}{2}\right)}{2ha} = f_{tow}\frac{\pi}{8}\frac{h_t}{h}. \tag{82}$$

The axial fiber volume fraction is then found to be 12.4% . The matrix porosity was assumed to be 40%, and was not measured independently.

Table VII. Optically measured properties of the woven material

	Measured
Number of Fibers in Tow (n)	420
Fiber Diameter (d_f)	14 µ
Tow Fiber Volume Fraction f_{tow}	0.342
Lateral Tow Spacing (a)	1050 µm
Undulation length (a_0)	1050 µm
Unit Cell Height (h)	260 µm
Yarn Height (h_t)	240 µm

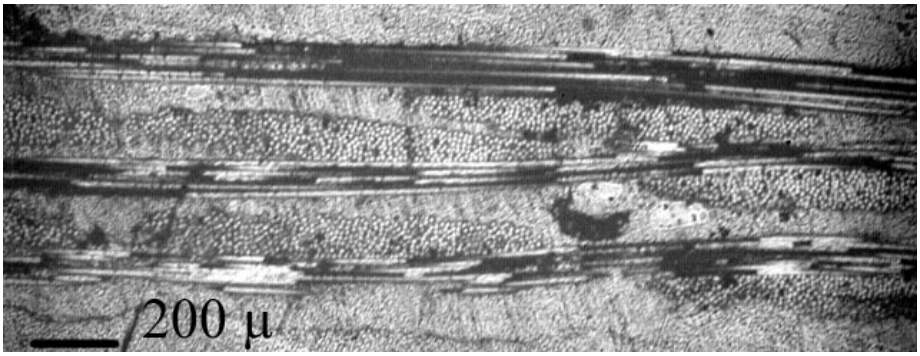

Figure 30. Microstructure of the woven materials

5.1.2 Matrix Cracking

Polished sections of several unidirectional panels were examined under scanning electron microscopy. A typical micrograph is shown in Figure 32. The cracks appeared to extend between adjacent fibers only, rather than extending across the entire specimen width and some regions appeared entirely free of cracks. The mean crack spacing was approximately 40 µm. For the 29% fvf specimens, the cracks were much more widely spaced – approximately 200 µm as seen in Figure 33. In both materials longitudinal matrix cracks which run in the direction of the fibers also exist, as indicated in Figure 34 which shows an end view of a specimen.

In the woven material, the crack patterns are more complex, as shown in Figure 35. In the interlaminar, matrix-rich regions cracks are spaced at approximately 150 µm. These cracks tend to deflect at ply interfaces to form delaminations and also penetrate into the 90° tows.

The sol-gel process used to manufacture these composites is prone to cracks produced by volume changes during processing [65], and this effect is the probable cause of the

cracks. Any residual stresses in the consitutents caused by differences in the coefficients of thermal expansion have probably been relieved by the matrix cracks.

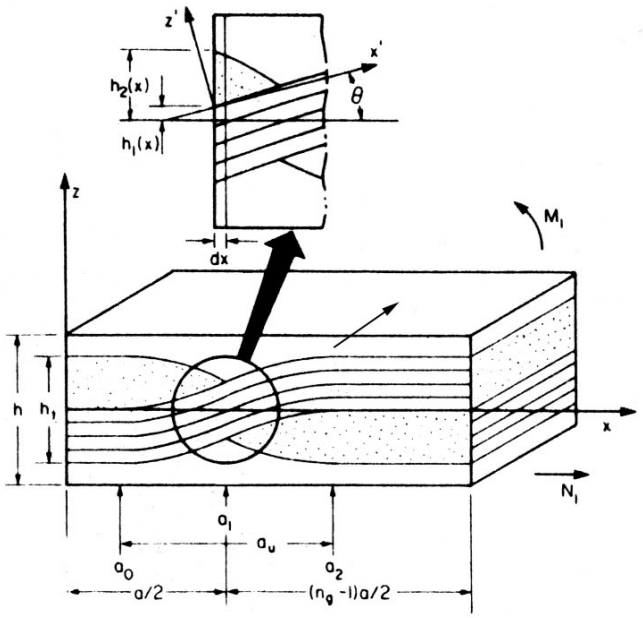

Figure 31. Schematic of a woven composite [66]

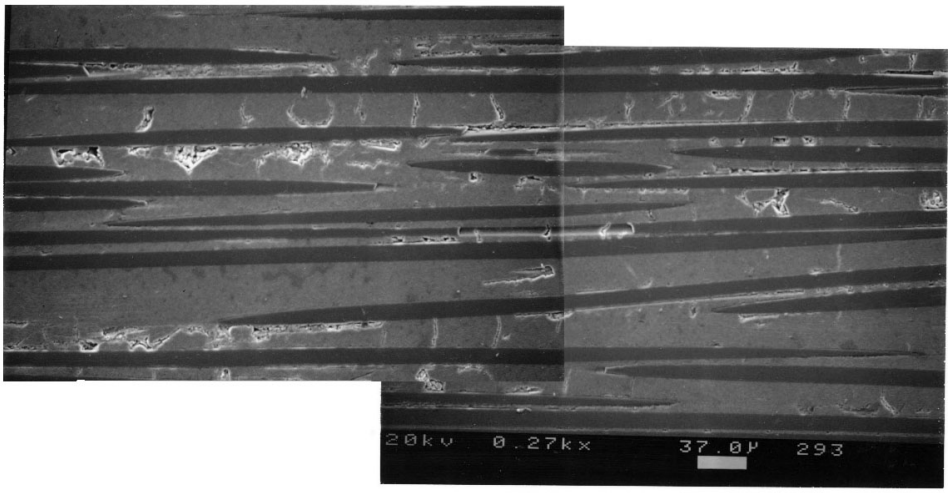

Figure 32. Surface of a virgin unidirectional specimen

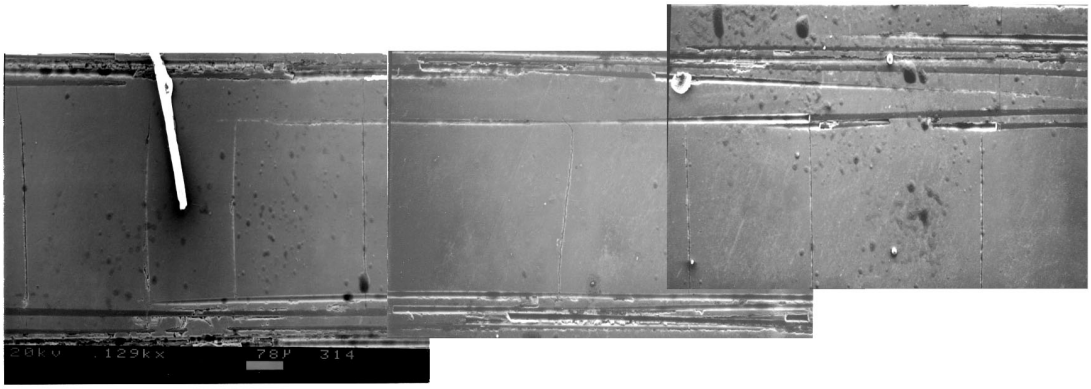

Figure 33. Initial matrix damage for a specimen with 29% fiber volume fraction

Figure 34. Longitudinal matrix cracking in virgin specimen

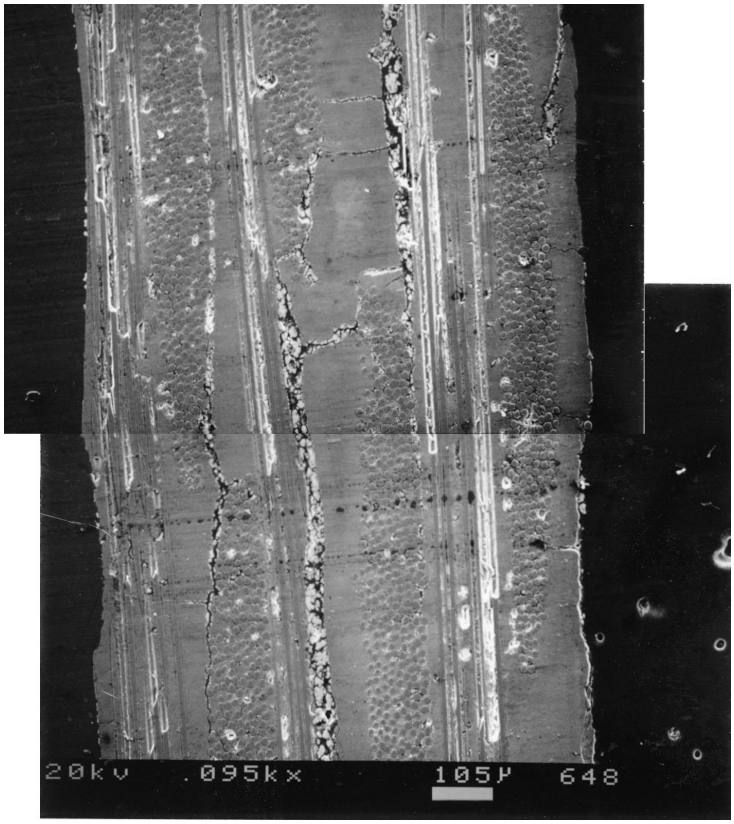

Figure 35. Crack patterns in a virgin woven specimen

5.2 Quasi-Static Tension Tests and Discussion

5.2.1 Quasi-Static Tension Test Results

Stress-strain curves for the unidirectional quasi-static tension tests are shown in Figure 36, for the woven specimens in Figure 37, and the averaged results are listed in Table VIII. The effects of temperature on the tensile modulus, strength, and failure strain of the unidirectional materials are shown in Figure 38 - Figure 40. There is a general trend toward decreasing strength and modulus and increasing failure strain with increasing temperature. The non-monotonic trends are believed to be a result of specimen-to-

specimen variabilities. These variabilities are most probably a consequence of the experimental nature of the manufacturing process. The stress-strain curves are slightly non-linear with stress. At room temperature this is indicative of damage to the fibers or matrix or sliding at the interface. At elevated temperatures creep of the constituents may affect the stress-strain curve.

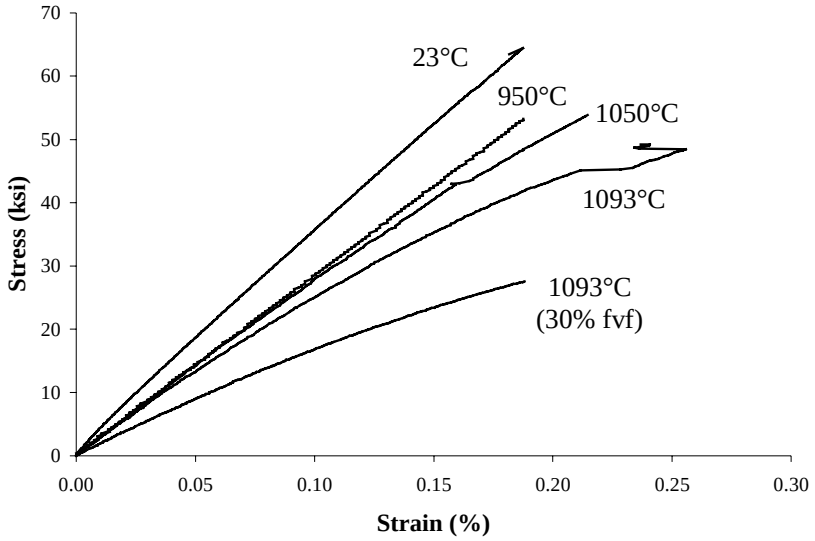

Figure 36. Sample unidirectional stress-strain curves

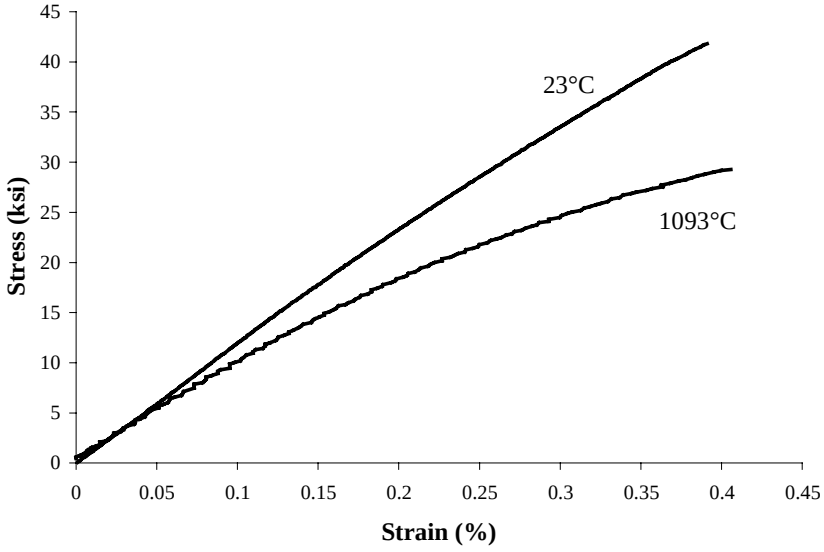

Figure 37. Sample stress-strain curves for woven specimens

Table VIII. Quasi-static tension test results

Temperature °C	Modulus (msi)	Strength (ksi)	Failure Strain (%)	Number of Tests
23	35.6 ± 5.2	56.8 ± 9.1	0.177 ± 0.034	4
23 (Woven)	11.2 ± 0.6	41.1 ± 1.0	0.375 ± 0.023	2
950	27.4 ± 0.9	49.6 ± 7.9	0.194 ± 0.037	5
1050	27.7 ± 2.3	53.7 ± 7.9	0.214 ± 0.018	3
1093	28.6 ± 2.0	44.3 ± 4.1	0.206 ± 0.240	3
1093 (27.5% fvf)	22.8 ± 7.5	27.3 ± 0.4	0.163 ± 0.040	2
1093 (Woven)	10.0 ± 0.5	28.9 ± 1.7	0.374 ± 0.025	4

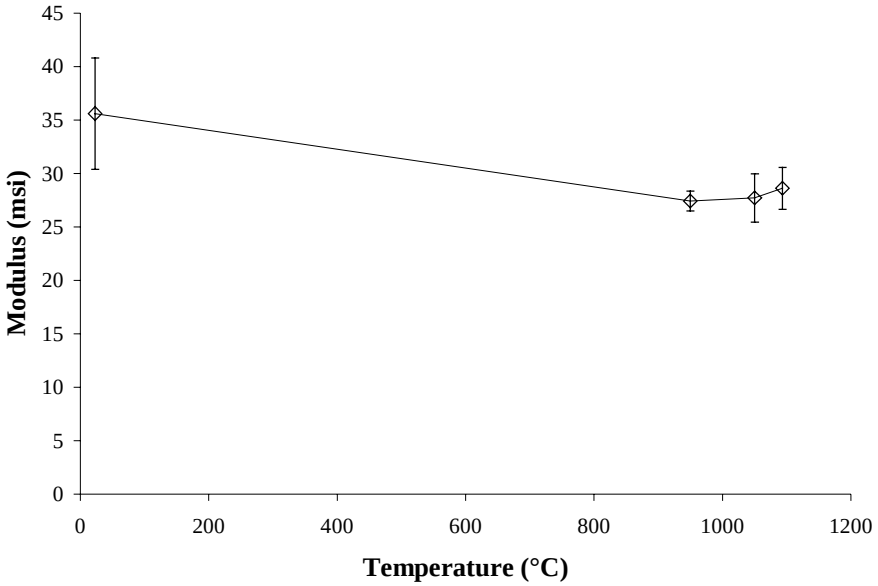

Figure 38. Tensile modulus as a function of temperature

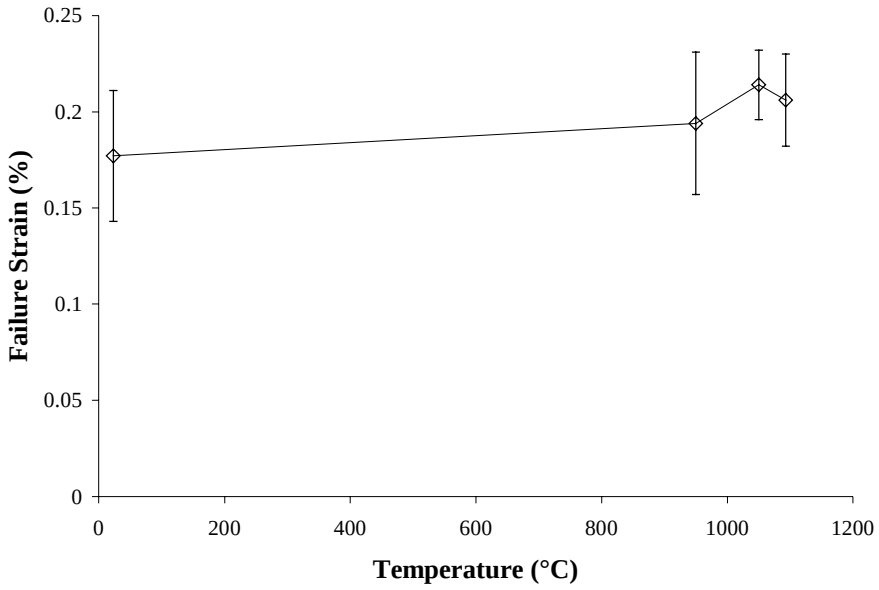

Figure 39. Tensile failure strain as a function of temperature

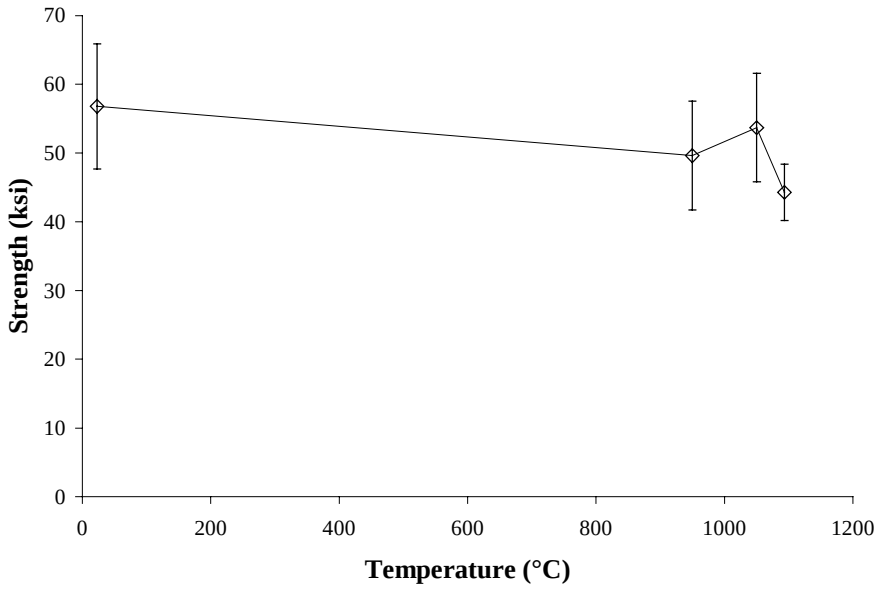

Figure 40. Tensile strength as a function of temperature

During quasi-static testing, longitudinal splits were observed in the unidirectional materials. The macroscopic appearance of failed test specimens are shown in Figure 41 and Figure 42 and the longitudinal splits are readily apparent. Specimens tested at elevated temperatures exhibited more splitting. A higher magnification image of the failure surface of a unidirectional composite is shown in Figure 43. There is no clearly defined failure plane in the unidirectional composites, which makes identification of fiber pullout lengths impossible. Although the woven materials fail in a narrowly defined region and do not demonstrate the extensive splitting seen in the unidirectional materials, the pullout lengths shown in Figure 44 are in excess of 2 mm. When these materials (both unidirectional and woven) are tested at room temperature failure is accompanied by disintegration of the matrix near the (presumed) failure plane, which is probably a result of the high matrix porosity. Further evidence of this is the appearance of the 90° tow in Figure 44, which is a loose bundle of fibers rather than a well-infiltrated tow. As a result, pullout measurements cannot be performed for either the unidirectional or the woven materials. However, it is evident from both failure surface micrographs that the fiber fractures are not confined to one plane of the composite, indicating that there is little stress concentration from broken fibers and that global load sharing is most likely applicable.

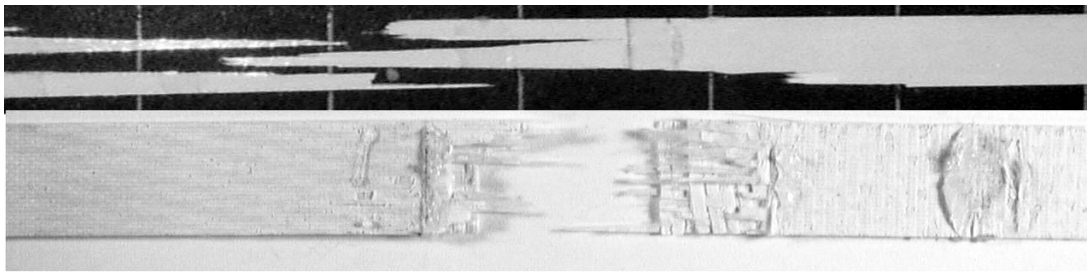

Figure 41. Fracture surfaces of room temperature quasi-static specimens

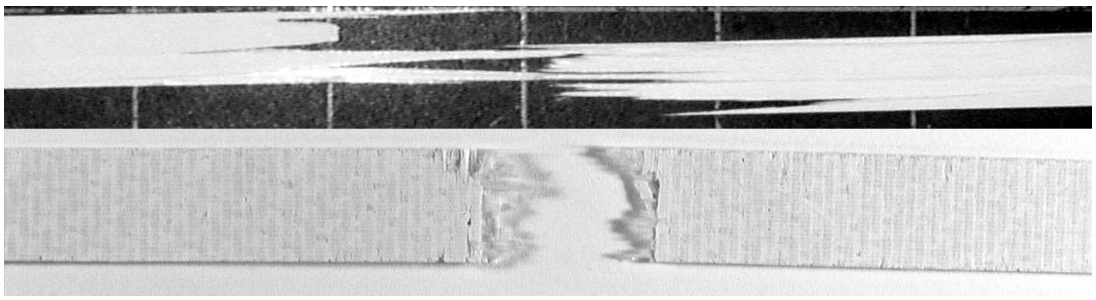

Figure 42. Fracture surfaces of elevated temperature quasi-static specimens (1093°C)

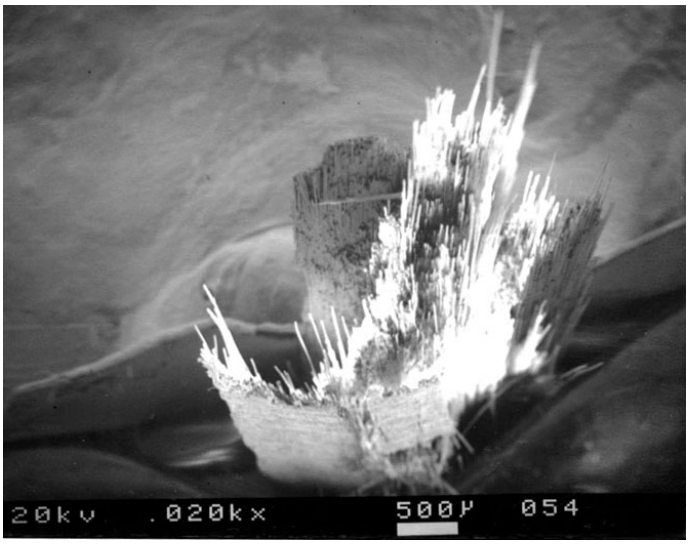

Figure 43. Fracture surface of specimen tested at room temperature

A small fraction of the fiber fracture surfaces at room temperature demonstrate evidence of fracture mirror-like patterns, although the proportion of fibers showing these features are too low for accurate analysis. A more typical fiber failure surface is shown in Figure 45, where the fiber fracture surfaces are smooth with no discernable fracture origin. Fracture surfaces of specimens tested at higher temperatures are similar both in the appearance of the composite and the appearance of the fiber fracture surfaces.

Figure 44. Fracture surface of a woven specimen tested in quasi-static tension at 1093°C.

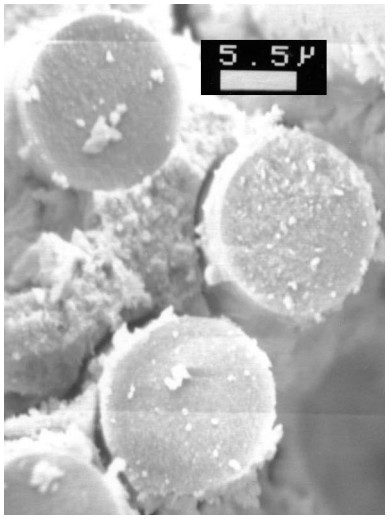

Figure 45. Fiber fracture surfaces for a specimen tested in quasi-static tension

Similar crack spacings and patterns as virgin specimens are seen on the polished edges of specimens tested at room temperature (Figure 46) and at elevated temperatures (Figure 47). In the woven materials, the crack patterns before and after testing are also similar,

although after testing there are collections of fiber fractures in the plane of the crack as shown in Figure 48.

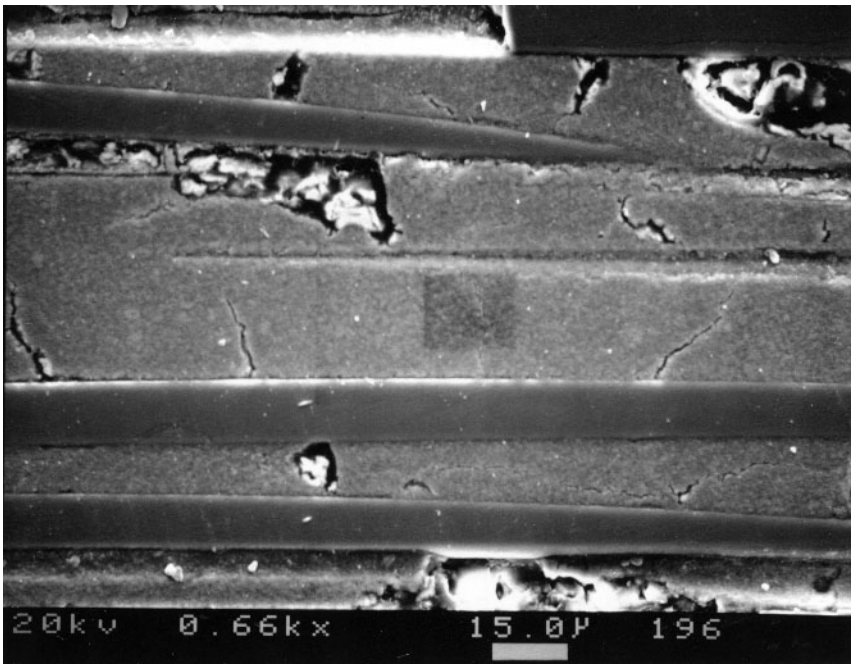

Figure 46. Matrix damage under room temperature quasi-static loading

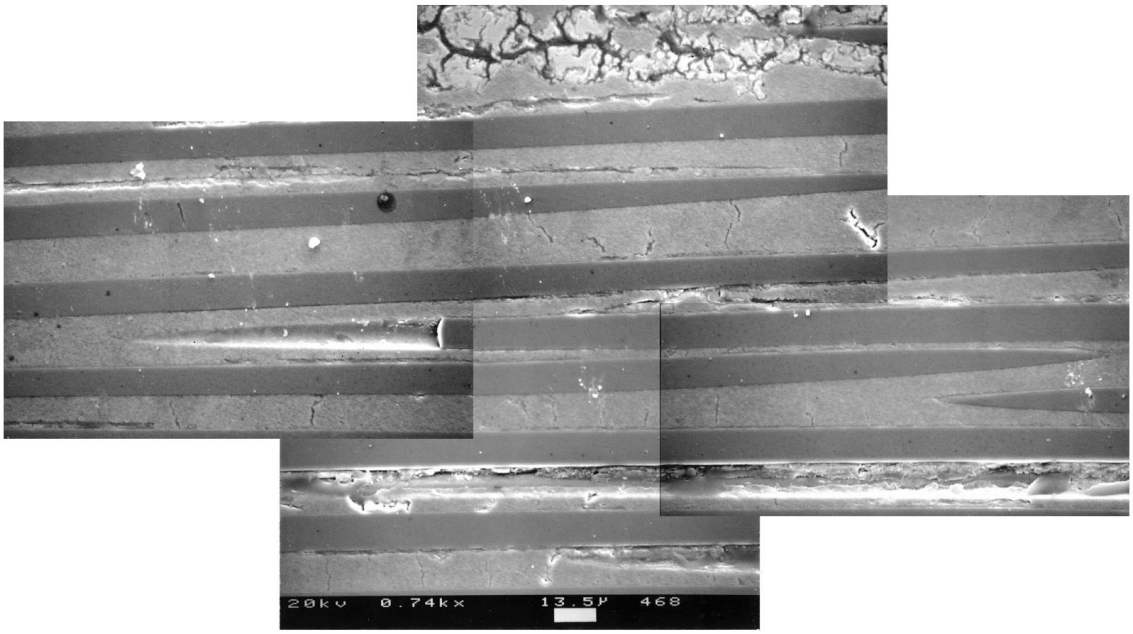

Figure 47. Matrix damage under 950°C quasi-static test

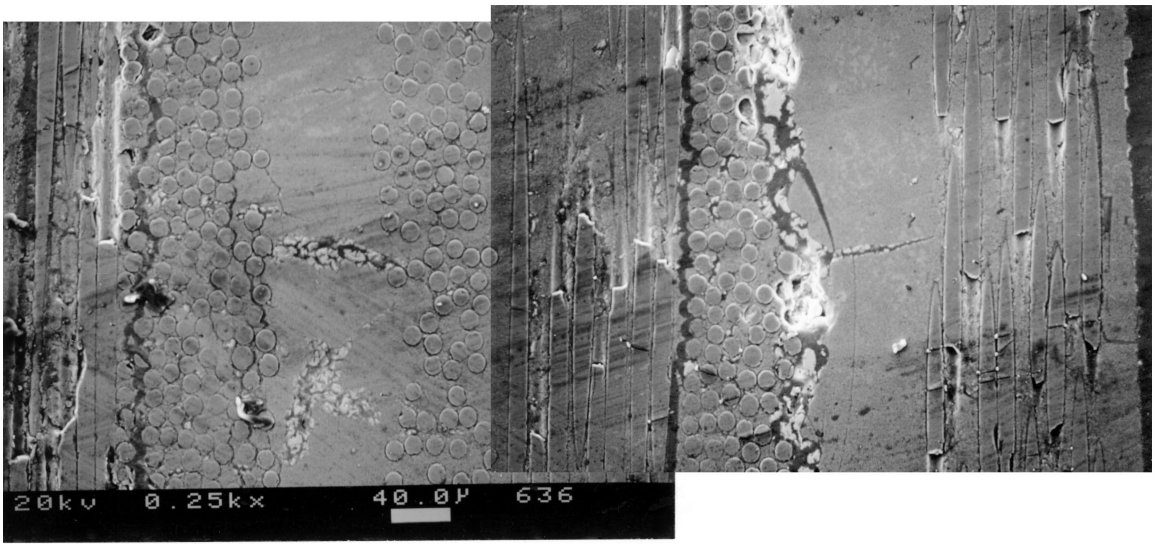

Figure 48. Cracking in a woven specimen which demonstrates fiber failure in the plane of the crack.

5.2.2 Hysteresis Loop Testing

Hysteresis loop testing was performed on unidirectional specimens at room temperature, 950°C and 1050°C. Sample stress-strain curves are shown in Figure 49. There is some hysteresis in the unload/reload cycle at room temperature, indicating that there is some frictional dissipation at the fiber/matrix interface. At elevated temperatures, however, there is very little hysteresis. This indicates an extremely low interface frictional stress. Often during both hysteresis and quasi-static tension tests, the composite will undergo longitudinal splitting. During hysteresis tests, longitudinal splitting is often accompanied by large hysteresis loops, indicating frictional dissipation. It may be that the friction accompanying the longitudinal splitting dominates over the interface frictional stress.

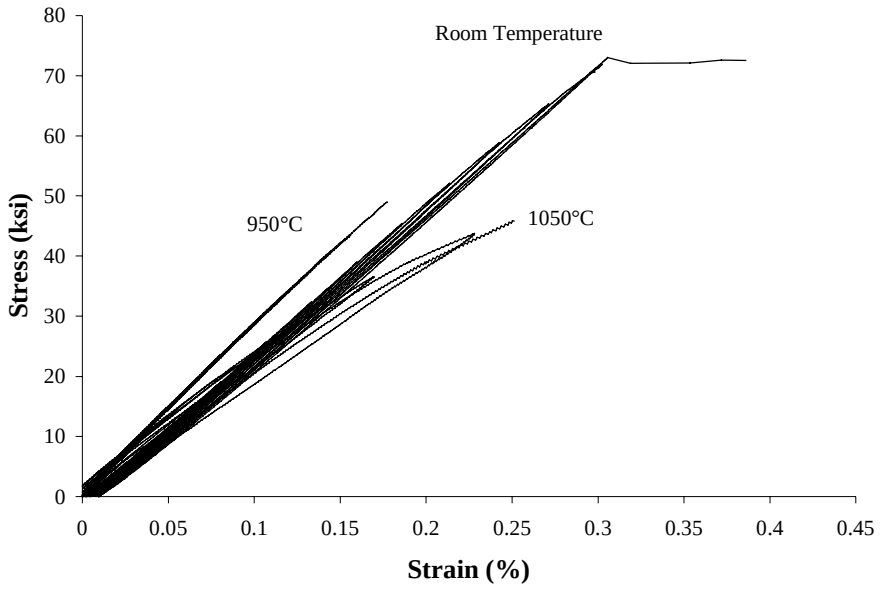

Figure 49. Hysteresis loop testing

5.2.3 Discussion of Quasi-Static Experiments

There are a number of material properties which must be determined in order to perform accurate stress-rupture analyses:

- fiber modulus (E_f),
- matrix modulus (E_m),
- fiber strength properties (σ_c, m), and
- interface frictional stress (τ).

The only property which is available in the literature is the room temperature modulus of the fibers, which has been determined to be 54 msi (360 GPa). All other properties must be found from analysis of the experimental results.

As a lack of specimens prevents the properties of the matrix from being determined by direct mechanical testing, they must be inferred from the mechanical testing of the composite. For unidirectional materials the rule of mixtures expression for composite modulus

$$E_c = fE_f + (1-f)E_m, \tag{83}$$

and the known modulus of the alumina fibers allows straightforward calculation of the effective matrix modulus, which is found to be 16.4 msi at room temperature.

The modulus of alumina is approximately 59 msi at room temperature, although the moduli of the yttria inclusions are somewhat lower (25 msi). The modulus of alumina is very sensitive to porosity. According to Knudsen [67], the modulus of porous alumina is

$$\frac{E}{E_0} = e^{-bP} \tag{84}$$

where b is a constant taken to be 3.95, P is the percent porosity, and E_0 is 59.5 msi. For the average 40% porosity of the specimens, the predicted modulus of pure alumina is 12.7 msi. The average measured weight fraction of yttria is 20%, as measured by MTI, which corresponds to a volume fraction of 16.4%. To consider the effect of 16.4% yttria inclusions with a modulus of 25 msi, Eshelby's Technique [68] is used with the yttria particles treated as spherical inclusions, which results in a predicted modulus of 14.1 msi. Thus the measured matrix modulus of 16.4 msi is slightly stiffer than that expected for a porous alumina with yttria inclusions. Possibly additional yttrium-aluminum-oxygen phases are present or the assumed spherical geometry of the yttria particles is inaccurate.

The amount of porosity, yttria content, and the fiber volume fractions do vary, however, from panel-to-panel. We can consider, for example, the values for each panel from which a room temperature tensile test specimen was obtained. For each panel, a specific modulus prediction accounting for the measured quantities can be made. The results of this analysis are listed in Table IX. The results do not indicate that this method is more

accurate than merely considering the average values of porosity, volume fraction, and yttria content.

Table IX. Panel specific modulus calculations

Panel	Fiber Volume Fraction (%)	Composite Porosity (%)	Yttria Volume Fraction (%)	Calculated Matrix Modulus (msi)	Calculated Composite Modulus (msi)	Measured Composite Modulus (msi)	Relative Error (%)
12	52.4	19.3	13.8	13.2	34.6	34.1	1.5
16	55.0	16.5	14.9	15.2	36.5	38.6	5.4
19	50.5	20.9	16.0	12.7	33.5	40.8	17.9
22	50.7	17.4	13.0	15.8	35.2	29.0	21.4

A similar analysis can be performed for the elevated temperature tests, although it is complicated by the fact that the effect of temperature on the modulus of Nextel 610 fibers is not known. There are two methods that we can use to predict the composite modulus. As one method we can consider the behavior of monolithic alumina at elevated temperatures and assume the fibers behave in an identical fashion. The modulus of 99.5% dense polycrystalline α-alumina decreases linearly with temperature [69], although the results are highly dependent on purity, as only a 1% weight fraction of silica can reduce the modulus by 15% [70].

Secondly, we can examine the modulus of materials with varying fiber volume fractions. The material from panels 1 and 2 have approximately 43.9% and 39.9% fiber volume fractions respectively. Specimens from these panels were tested in tension at 1093°C. The modulus values can be compared to the values obtained from materials with 51% and 29% fiber volume fraction. Stress-strain curves from all four materials are shown in

Figure 50, where the decrease in modulus with decreasing fiber volume fraction is evident. The modulus as a function of fiber volume fraction is shown in Figure 51 along with a line corresponding to a fiber modulus of 49.9 msi and a matrix modulus of 4.0 msi. Unfortunately, specimen availability limited this technique to only one temperature.

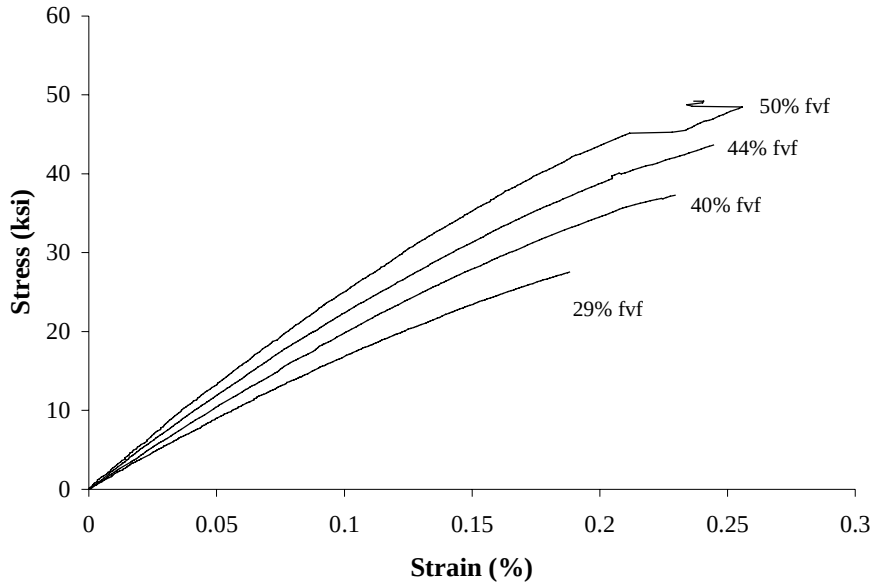

Figure 50. Stress-strain curves at 1093°C for specimens with varying fiber volume fractions

The results for the matrix modulus as a function of temperature are given in Table X. There is a rather large difference between the fiber modulus as determined from the tests at 1093°C and from comparison to monolithic alumina. This is most probably due to a high modulus measurement for the 50% fvf specimens at 1093°C. Further examination of Nextel fibers will be necessary to reconcile these two methods.

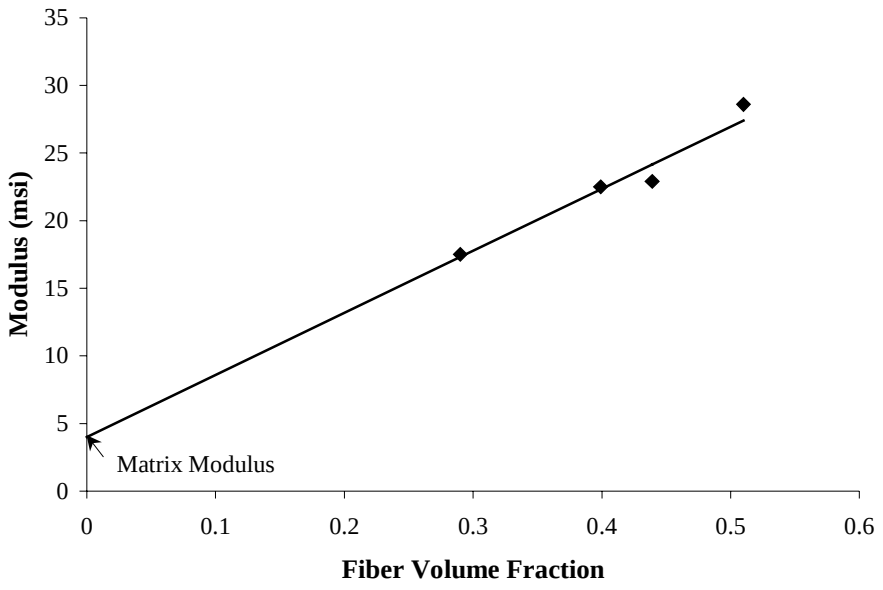

Figure 51. Effect of fiber volume fraction on elastic modulus at 1093°C

Table X: Matrix modulus calculated from tension tests

Temperature (°C)	Fiber modulus (msi)	Effective matrix modulus (msi)
23	54	17.2
950	47.5	7.3
1050	46.8	8.6
1093	46.6	10.6
1093 (fvf method)	49.9	4.0

The interface frictional stress can be obtained from a number of possible methods. One of the more promising is the hysteresis loop technique of Vaggagini et al. [16]. The main advantages of this method are that the value is an average obtained over a large number of fibers (all fibers in the cross-section) and that it can be used at elevated temperatures.

The information required for the analysis is the tangent modulus of the composite stress-strain response as the composite is unloaded from the peak applied stress. The slope of the reciprocal of the tangent modulus, called the inverse tangent modulus (ITM) is inversely proportional to the interface frictional stress.

$$\mathfrak{L} = \frac{b_2 \left(1 - a_1 f\right)^2 r}{8 z_0 \tau E_m f^2} \tag{85}$$

where $2\mathfrak{L}$ is the measured slope of the ITM and b_2 and a_1 are combinations of elastic constants determined by Hutchinson and Jensen [5].

The ITMs obtained from a room temperature hysteresis loop test are shown in Figure 52. Only the regions near the peak stress are used to avoid problems such as crack closure [17]. The value of $\mathfrak{L}$ is found to be $(4.6 \pm 1.5)\ x10^{-8}$ ksi^{-2} and given a crack spacing of 40μ the interface frictional stress at room temperature is found to be 3.6 ± 1.2 ksi. Push-out tests[9] on virgin specimens found an interface frictional stress of 4.8 ± 2.3 ksi, which shows fairly good agreement.

At elevated temperature, values of $\mathfrak{L}$ were much higher, ranging from $1.3x10^{-7}$ ksi^{-2} to $8.5x10^{-7}$ ksi^{-2}, which correspond to interface frictional stress values of approximately 0.5 ksi. Unfortunately, the curves were very irregular and noise in the strain signal implies that the data is suspect. Push-out tests run on a specimen exposed to 37 ksi for 50 hours yielded an interface frictional stress of 4.2 ± 1.8 ksi. This shows that there is little, if any, degradation of the interface stress due to elevated temperature stress-rupture testing. Therefore, the value of τ obtained at room temperature will be used for the elevated temperature analyses as well.

[9] Performed by Jeff Eldridge at NASA-Glenn Research Center, Cleveland, Ohio

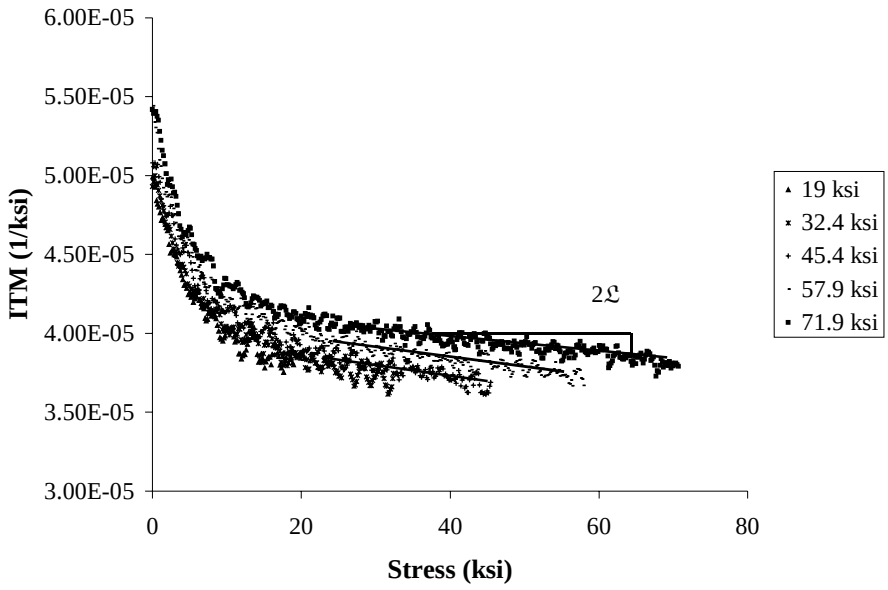

Figure 52. Inverse tangent modulus plot at room temperature

From observation of the polished specimen edges, it was concluded that the matrix is generally undamaged by monotonic tension or stress-rupture, save for extreme damage very near the fracture plane. The lack of a well-defined fracture plane means that measuring fiber pullout is impossible. Due to a lack of sufficient fiber fracture mirrors, fiber in situ strength properties can also not be determined. However, we do have accurate measurements of the composite tensile strength, and using the tensile strength model detailed in Chapter 3, we can derive a combined strength measure, σ_c, the fiber characteristic strength.

Recall that the strength of a composite depends on the simultaneous solution of two equations, the equilibrium equation (Equation (69)) and the fiber damage equation (Equation (47), for example). Incorporated in these equations are the crack spacing and fiber and matrix moduli. Unfortunately this model does not provide a well-defined relationship between the fiber characteristic strength, σ_c, and the measured composite ultimate tensile strength, σ_{ult}, although it can be used to determine the tensile strength

through numeric solution techniques. Stress-strain curves created using this model with τ values obtained from the hysteresis loop analysis and the measured values of f, E_m, E_f, and z_0 are shown in Figure 53 and Figure 54. The value of σ_c was chosen in order to produce a tensile strength which matches the experimentally determined value. It can be seen from these figures that while it is possible to match the initial moduli, the degree of non-linearity near failure predicted by the model is not seen in the experimental results.

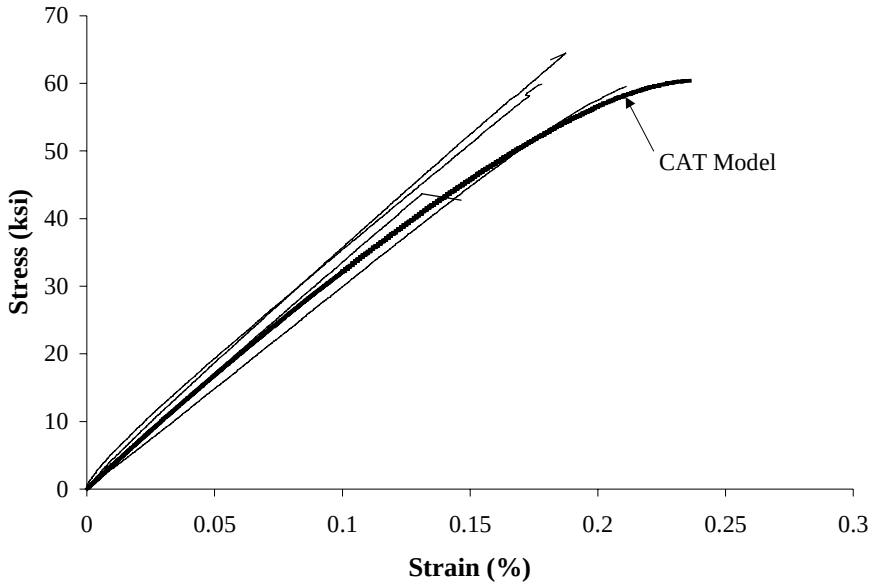

Figure 53. CAT model compared to room temperature data (σ_c = 167 ksi)

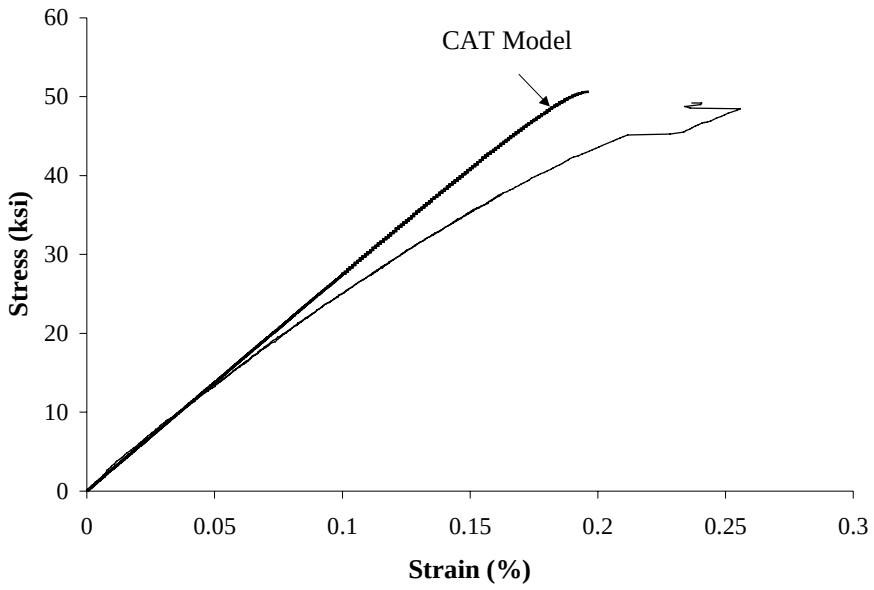

Figure 54. CAT model compared to experimental data at 1093°C (σ_c = 139 ksi)

The characteristic strength, σ_c, is given by

$$\sigma_c = \left(\frac{\sigma_0^m l_0 \tau}{r} \right)^{\frac{1}{m+1}}. \tag{86}$$

For the measured interface frictional stress of 3.6 ksi, at a 1 inch gage length the Weibull strength of the as-processed Nextel fibers is deduced to be 67 ksi at room temperature. This is far lower than the virgin fiber strength of 460 ksi [41] and indicates significant fiber damage during processing. Xu et al. reported a drop in fiber strength after 1100°C exposure for two hours [43], but not to such a large extent.

For the woven materials, a strict determination of the moduli requires an accurate accounting of the axial fiber tow paths. However, given that the material is an eight-harness satin weave, where tow crossovers occur over approximately one-eighth of the tow length, the modulus should be only slightly less than that of a crossply composite.

The modulus of a 0° composite with a 34.2% fiber volume fraction determined by the rule of mixtures is approximately 30 msi, using the matrix properties determined from the unidirectional materials. The elliptical tow will occupy an area fraction of $(\pi/8)(h_t/h)$ in the cross-section. Thus the tow by itself is sufficient to yield a composite modulus of 10.8 msi, which is very close to the measured value of 11.2 msi. Perhaps the large amount of delamination in the as-received materials de-couples the axial tow from the remainder of the composite. An alternate theory is a lower matrix modulus in the woven materials than in the unidirectional materials, although this has not been examined experimentally.

5.3 Time-Dependent Testing

5.3.1 Stress-Rupture Testing

The measured lifetimes from the stress-rupture testing performed at 950°C and 1050°C on the 51% fvf (fiber volume fraction) specimens are shown in Figure 55. The strain rates during testing for two tests at 1050°C are shown in Figure 56. The excursion shown in the 25 ksi test is most likely due to longitudinal splitting, which often creates a discontinuity in the strain measurement. In the stress-rupture tests, the strain rate quickly decreases to a steady state, then slowly increases over the final 10%-25% of life. The steady-state strain rate as a function of stress is plotted in Figure 57. The strain at failure for these tests is shown in Figure 58. Failure strains in excess of 7% can be observed at 1050°C under 25 ksi applied stress. This is a 30-fold increase over the strains measured in quasi-static tension. The lifetimes obtained at 1093°C tests for the 29% fiber volume fraction specimens and for the woven specimens are shown in Figure 59 and the steady-state strain rates are shown in Figure 60.

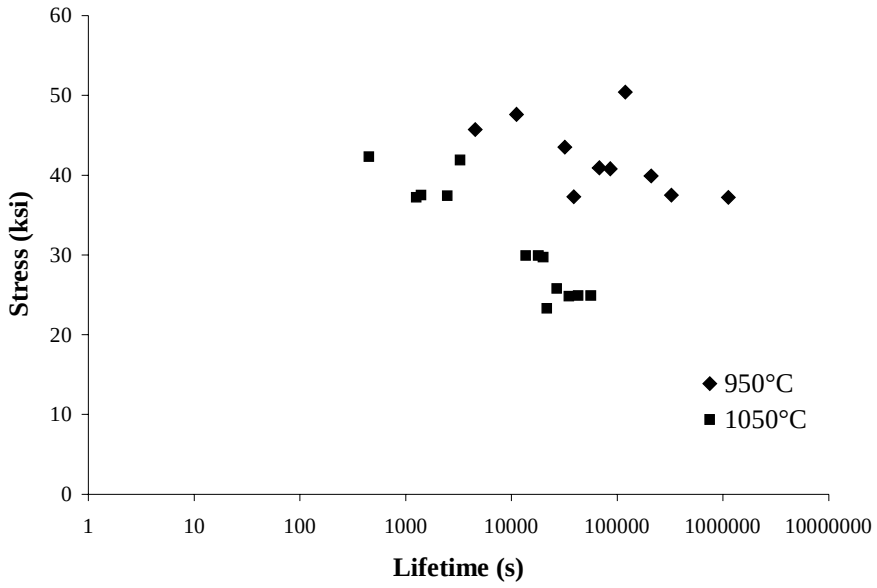

Figure 55. Stress-rupture testing for 50% fiber volume fraction specimens

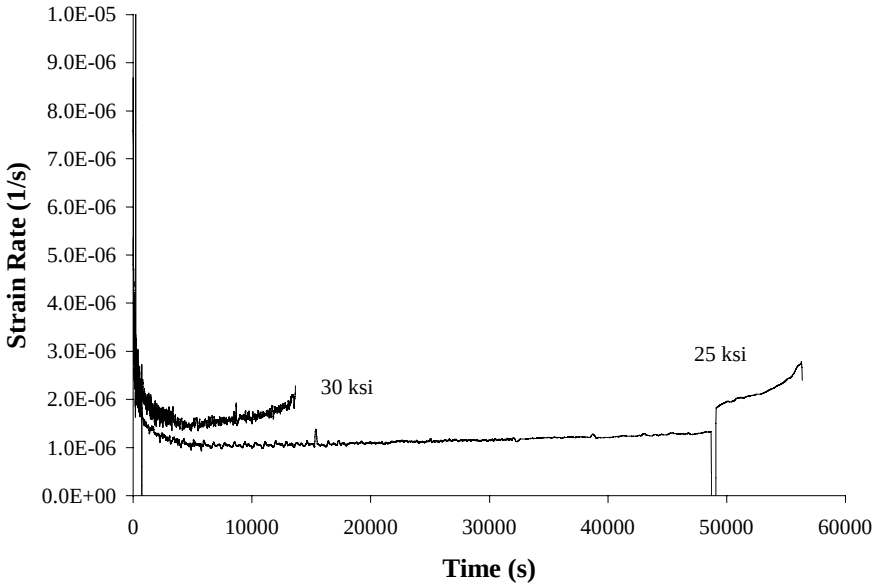

Figure 56. Strain rates during two stress rupture tests at 1050°C

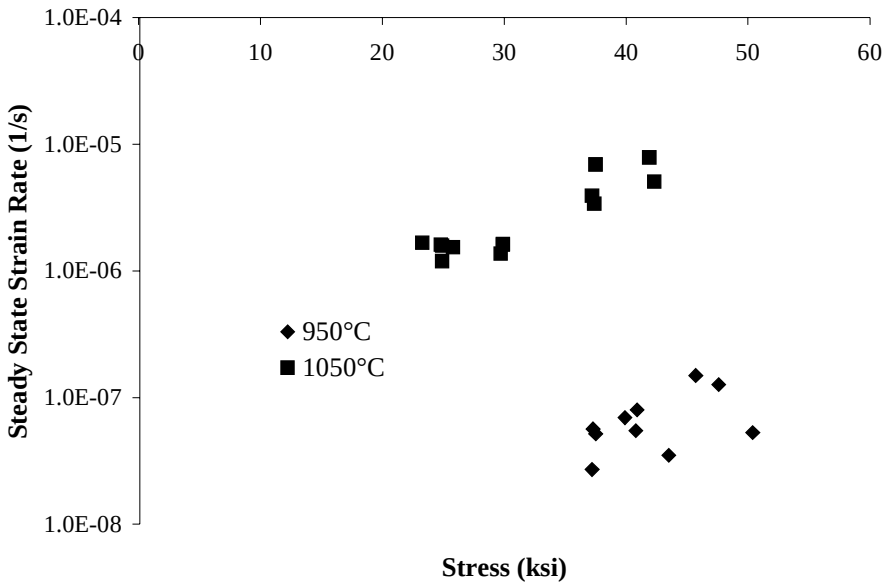

Figure 57. Steady-state strain rate during stress-rupture

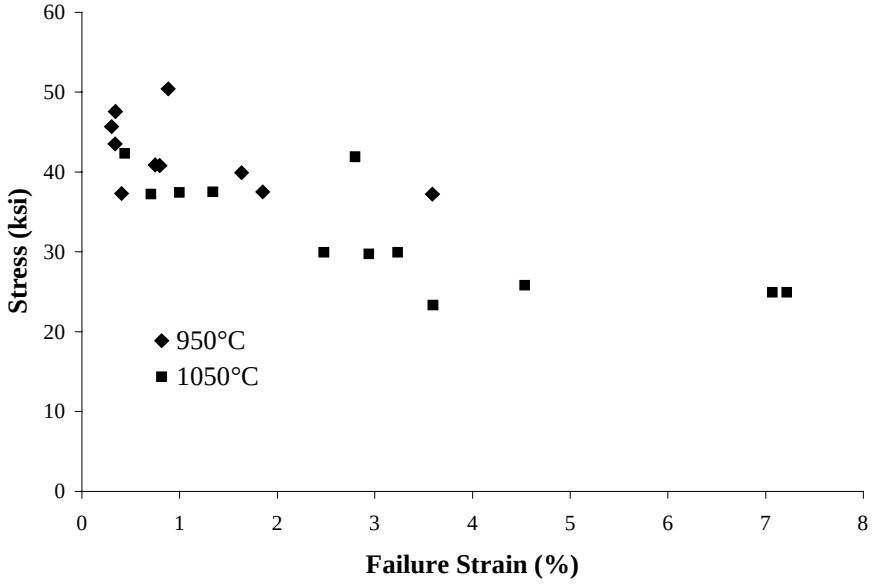

Figure 58. Failure strain in stress-rupture

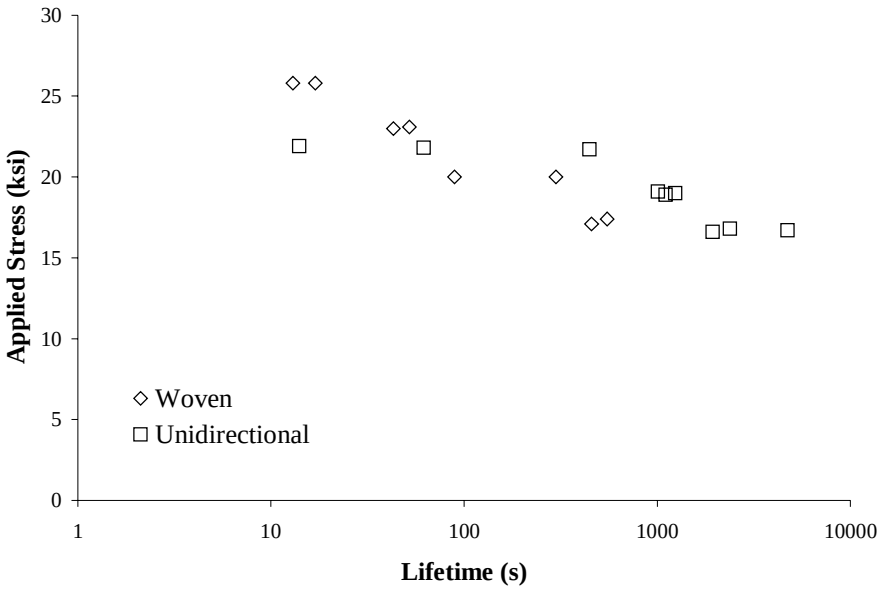

Figure 59. Stress-rupture behavior at 1093°C

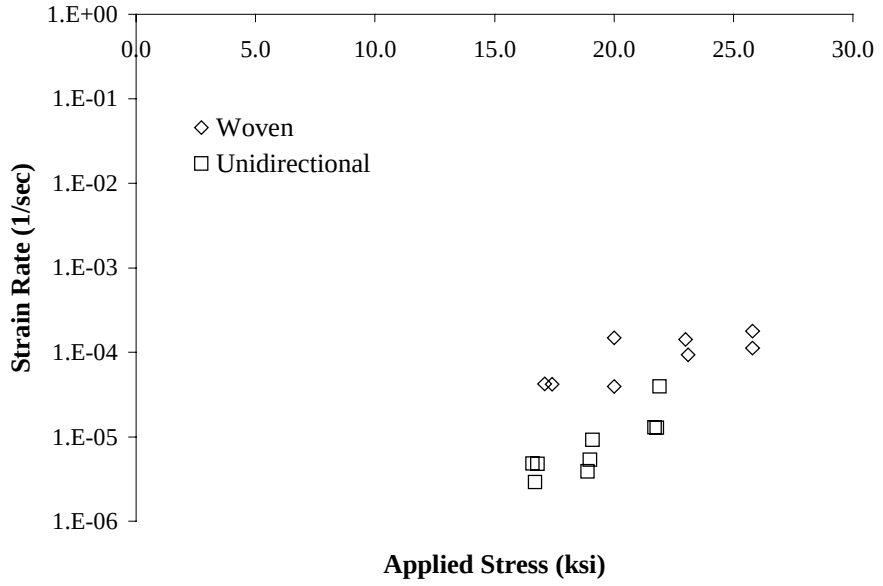

Figure 60. Steady-state strain rate at 1093°C

The macroscopic appearance of broken specimens is shown in Figure 61. A typical fracture surface for a unidirectional specimen tested in stress-rupture to failure is shown in Figure 62. As with the specimens tested in quasi-static tension, there is no readily

definable crack plane from which to measure pullout. The crack spacings observed on the specimen edge are approximately 40μ, as shown in Figure 63 and Figure 64, unchanged from the virgin material. The fiber failure surfaces were fairly smooth (Figure 65 and Figure 66) and did not differ significantly in appearance from those tested in quasi-static tension.

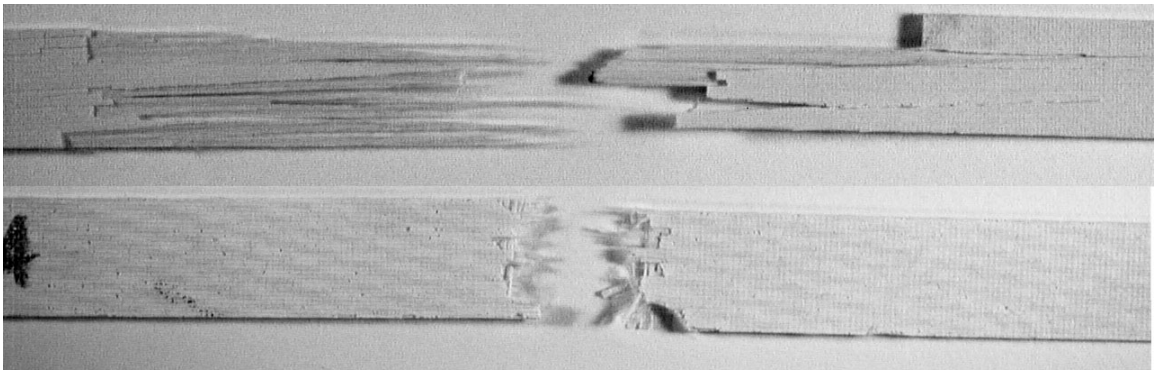

Figure 61. Fracture surfaces of specimens tested in stress rupture at 1093°C

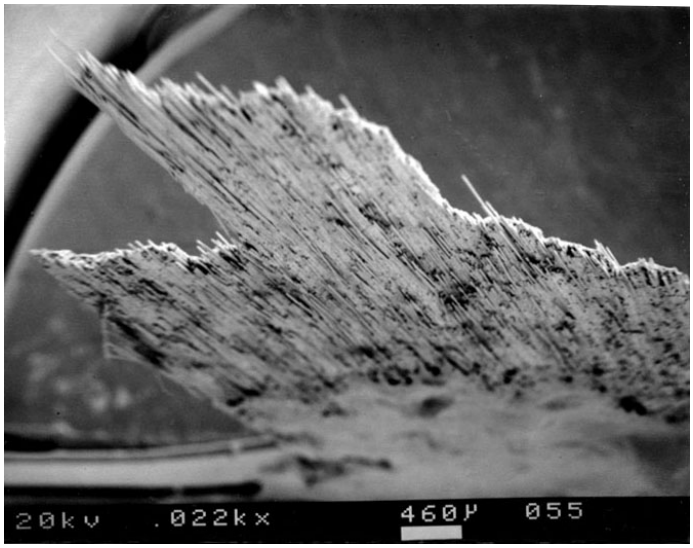

Figure 62. Fracture surface of specimen tested in stress-rupture at 950°C

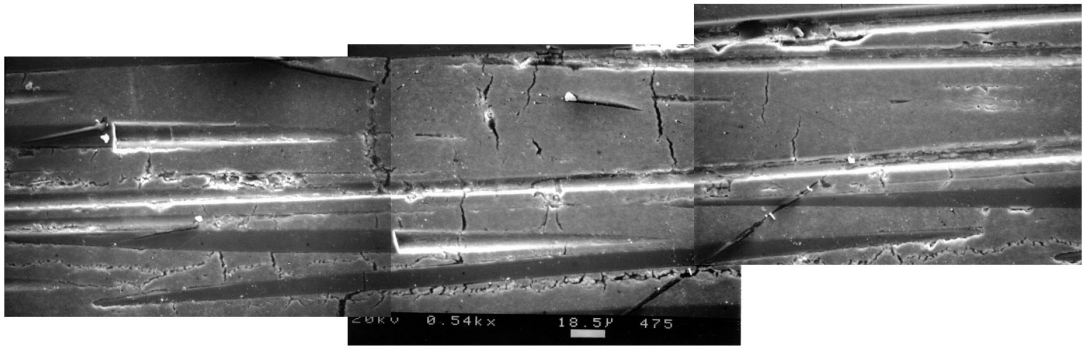

Figure 63. Matrix damage in stress-rupture at 950°C

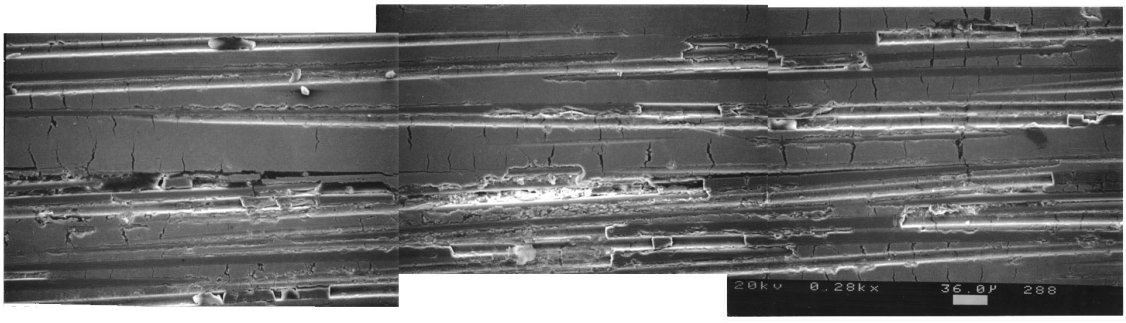

Figure 64. Matrix damage in stress-rupture at 1050°C

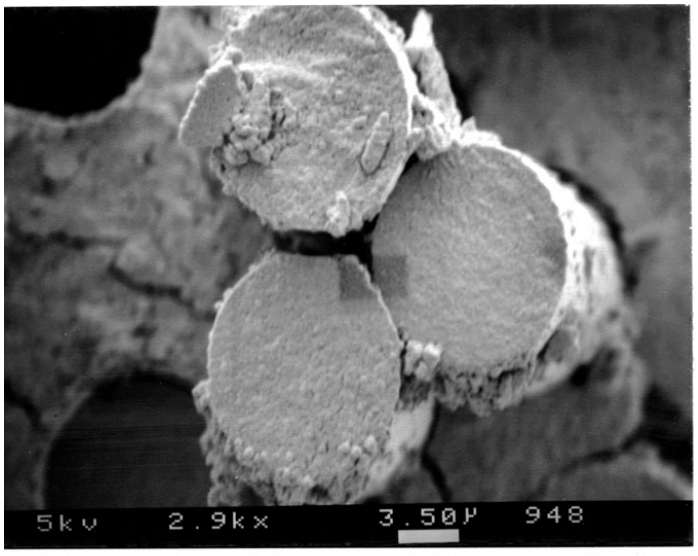

Figure 65. Fiber fracture surfaces in stress-rupture at 950°C

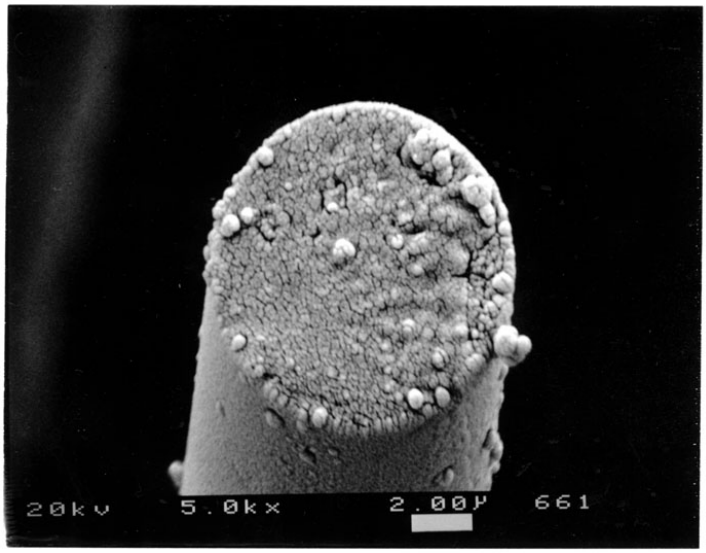

Figure 66. Fiber fracture surface under stress-rupture at 1093°C

5.3.2 Residual Strength Testing

Residual strength testing was performed successfully only for one condition – 1050°C and 25 ksi applied stress. At other stresses and temperatures, the specimens failed in stress rupture with lifetimes shorter than the planned test duration and were included in the stress-rupture data. The remaining strengths after stress rupture are shown in Figure 67. On this plot, the quasi-static tensile points are included at time $t = 0$, and the stress-rupture tests to failure are shown at the applied stress during the test. Figure 68 shows that there is a slight but definite change in tensile modulus for the four residual strength tests. As the matrix damage has been shown to be minor, it is presumed that this demonstrates the effect of broken fibers on the tensile modulus.

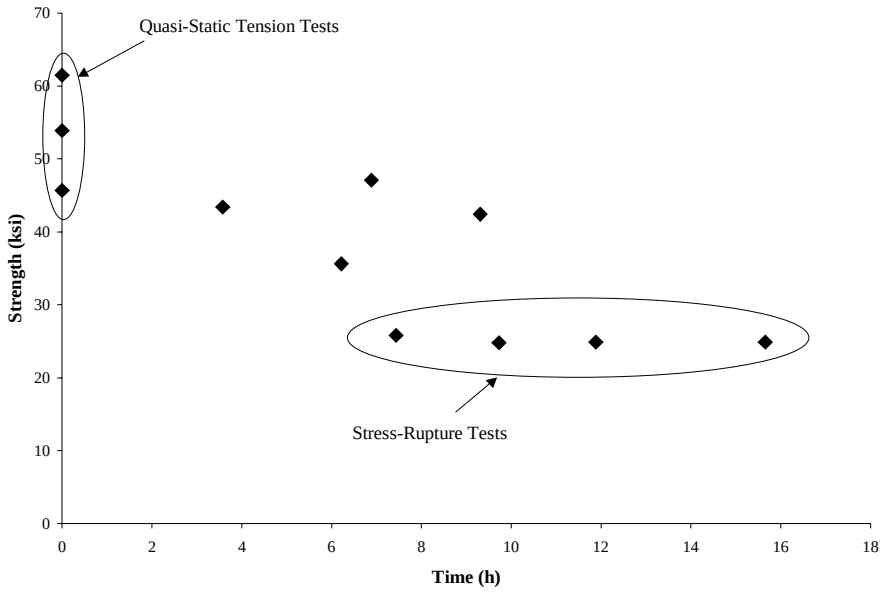

Figure 67. Residual strength testing at 1050°C and 25 ksi applied stress

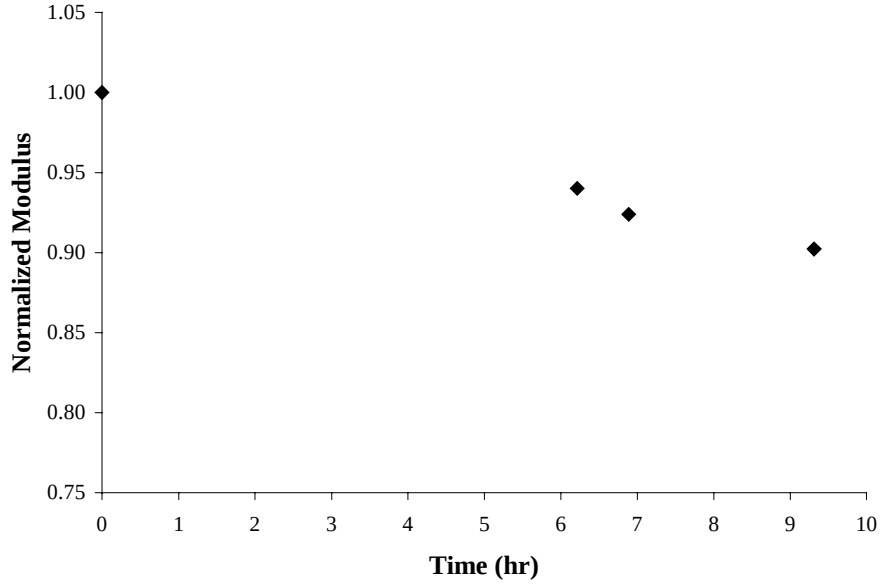

Figure 68. Modulus change due to stress-rupture testing

5.3.3 Discussion of Stress-Rupture testing

For traditional engineering materials, there are many parameters with which stress-rupture is described. For composite materials, the Larson-Miller parameter is often used. The Larson-Miller parameter is derived from an Arrhenius-type equation

$$t_r = Ae^{\frac{\Delta H}{RT}}, \tag{87}$$

where t_r is the stress-rupture lifetime, ΔH is the activation energy for the process, T is the absolute temperature, R is the ideal gas constant, and A is a constant. Rearrangement of this equation yields the most common form of the Larson-Miller expression

$$\frac{\Delta H}{R} \equiv Q = T\left(F + \log t_r\right). \tag{88}$$

Failure at a given applied stress will occur at a critical value of Q, which must be determined experimentally. The Nextel 610 fiber data in Figure 8 has been collapsed on to a Larson-Miller plot with the constant, F, equal to 22. One straightforward method of predicting composite lifetime is to compare the Larson-Miller plot of the fibers to that of the composite [71]. This method is perhaps applicable when the matrix has been cracked and carries little stress. Although it ignores stress transfer from broken to intact fibers and the appropriate fiber length scales in the composite, it is easy to apply and requires only single fiber tests, which avoids the expense of composite processing. To make this comparison, the fiber stresses are scaled by the fiber volume fraction, as the fibers are assumed to carry all the stress. The results of such a comparison are shown in Figure 69. All composite rupture data from both the unidirectional and woven materials have been collapsed on this figure. The agreement is rather poor. Additionally, the Larson-Miller parameter is a measure of failure time only and is not designed to determine residual strength during the stress-rupture test.

The Monkman-Grant relationship is also a potential method of describing stress-rupture lifetime. The Monkman-Grant equation is a relationship between the steady-state strain rate and the rupture lifetime

$$\log t_r + k \log \dot{\varepsilon} = D, \tag{89}$$

where k and D are constants.

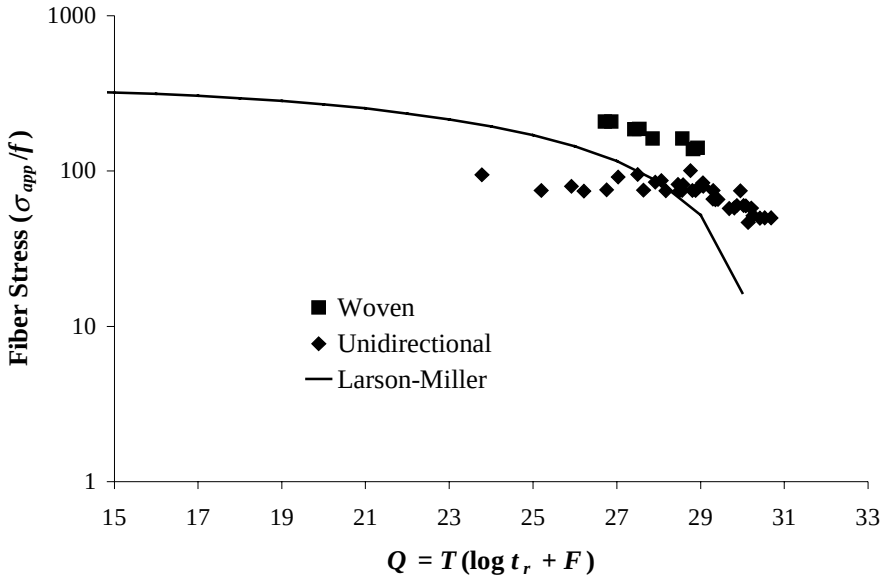

Figure 69. Larson-Miller plot of fibers compared to experimental composite data

In cases where the matrix has not cracked and still carries load this has been proposed as a method of life prediction [71]. The Monkman-Grant plot of the composite rupture lifetime versus the steady-state strain rate as compared to fiber data is shown in Figure 70. The accuracy in this plot is better than the Larson-Miller plot, but the composite data at each individual temperature examined has a steeper slope than the fiber data. As with the Larson-Miller plot, this method of describing the data does not provide any information about remaining strength during stress-rupture.

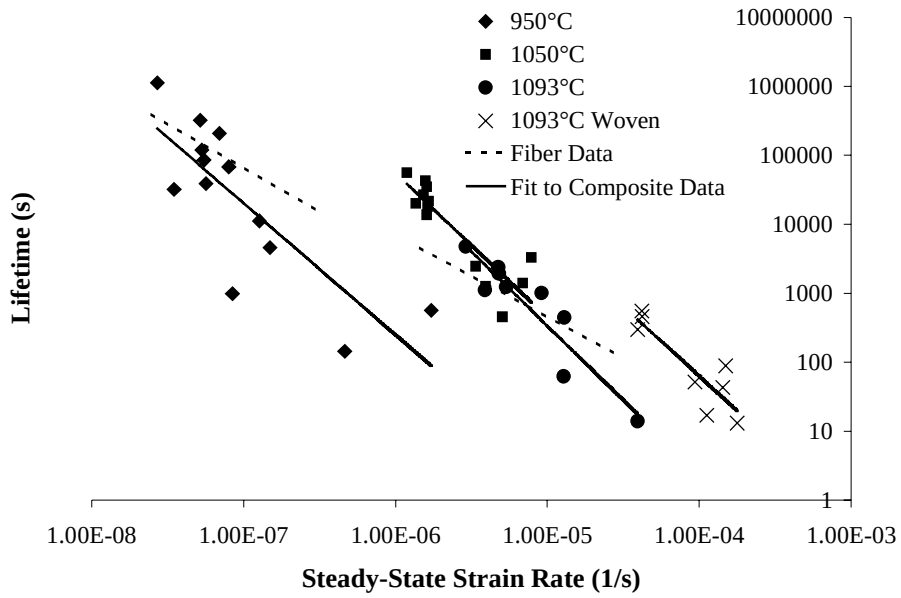

Figure 70. Composite Monkman-Grant plot compared to fiber data. Fiber data from Reference [71].

5.4 Application of the Stress-Rupture Methodology

Ultimately, the utility of a stress-rupture lifetime prediction method will depend on its applicability to real-world situations. The experimental data obtained in this chapter are compared to the predictions obtained from the method of Section 3.2.2 to determine the accuracy of the proposed technique. Predictions are made for lifetime and creep rate. The parameters obtained from analysis of the quasi-static tests discussed in Section 5.2.3 will be used as well.

5.4.1 Steady-State Creep Rate

The steady-state creep rate of Nextel 610 fibers has been established by Wilson et al. [47] to be

$$\dot{\varepsilon} = 2.944\text{x}10^{15}\sigma^{3}e^{\left(\frac{-660\,\text{KJ}}{RT}\right)}, \tag{27}$$

where stress is measured in ksi. The matrix behavior in creep is not known, although the behavior of the matrix can be determined through analysis (using Equation (80))of the measured steady-state creep rates, which are shown in Figure 57.

The value of α in creep was determined to be 0.75 for all elevated temperature tests. This is slightly different from the value obtained from the quasi-static tension tests, which was approximately 0.85. This indicates that the matrix stresses are, on average, higher in creep than in quasi-static tension. The results of matching the strain rates in this fashion is shown in Figure 71. In Figure 71, the strain rates obtained by setting α = 0.75 are shown as the solid lines, while the strain rates obtained using the quasi-static moduli are shown in the dashed lines.

During the initial stage of the stress-rupture test (at time t = 0), the composite strain rate will be governed by the quasi-static fiber stress profile and the primary creep behavior of the constituents. A comparison of the strain rates measured at the beginning of the stress rupture test to the strain rates predicted using the value of α appropriate for quasi-static tension is shown in Figure 72.

The initial creep rates at 1050°C match the values obtained using the steady-state fiber creep behavior (Equation (27)) and the value of α obtained from the quasi-static moduli rather well. At 950°C, the initial strain rates are much higher than the predicted values. Primary creep in Nextel fibers is rather limited in duration and has not been reliably

quantified [47], so the close agreement at 1050°C may not be indicative of material behavior.

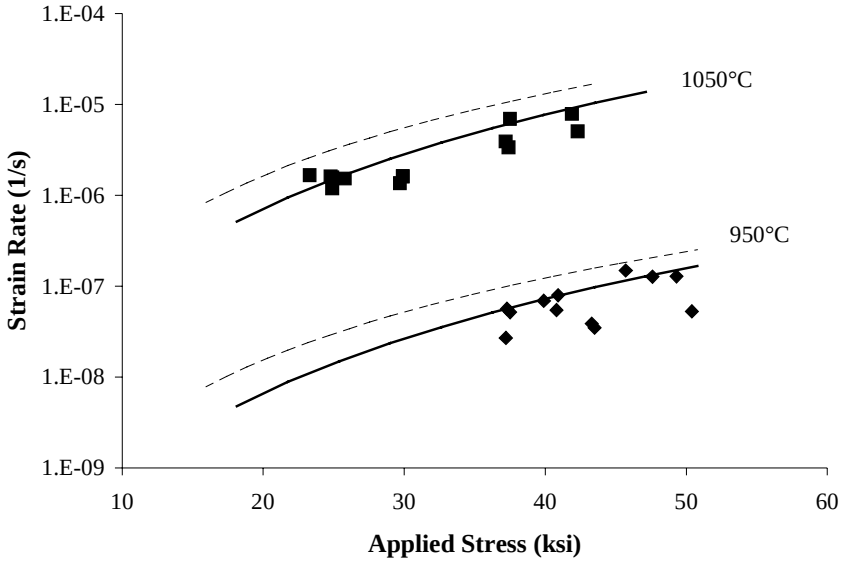

Figure 71. Strain rates found by setting α = 0.75

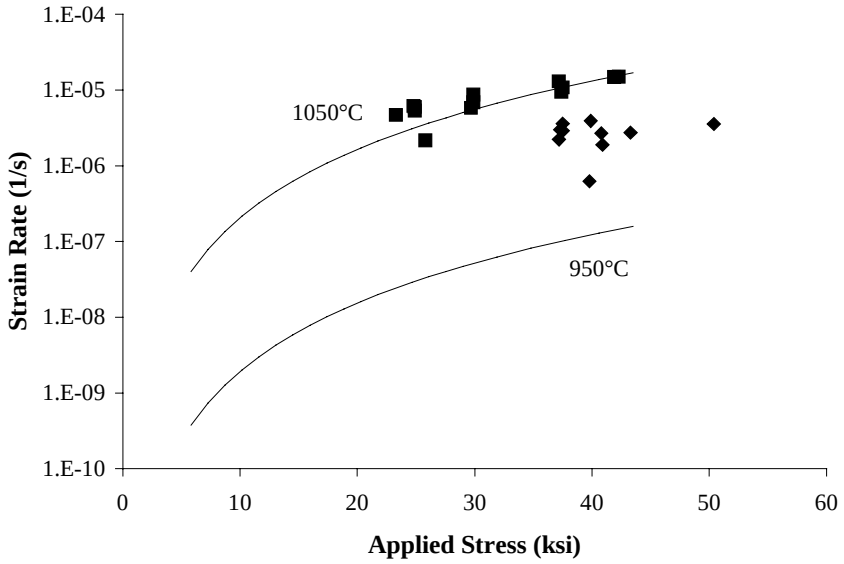

Figure 72. Initial strain rates in stress-rupture compared to predictions based on quasi-static properties

5.4.2 Stress-Rupture Lifetime

There are three parameters which describe the stress-rupture behavior of single fibers, σ_i, β, and the product $CY^2K_{Ic}^2$. These parameters can be found by fitting experimental data to the single fiber lifetime equation, Equation (57). The resulting values are given in Table XI and the comparisons to the single fiber experimental data (shown previously in Figure 7) are shown in Figure 73.

Table XI. Fiber stress rupture data

Temperature (°C)	σ_i (ksi)	β	$CY^2K_{Ic}^2$ (psi^2/s)
900	260	12	2.10×10^8
950	248	7.2	4.21×10^8
980	241	4.7	8.41×10^8
1050	220	2.4	2.52×10^8

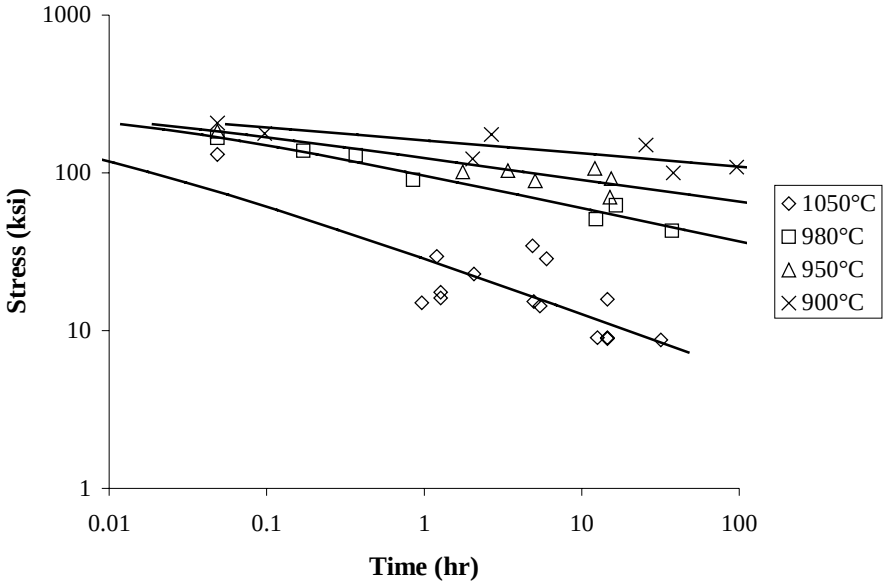

Figure 73. Comparison of experimental data to fitted behavior

The value of σ_i obtained in this fashion is significantly greater than that found from the analysis of the quasi-static tensile strength of the composite. The tests in Figure 73 were

performed on as-received fibers, which have a higher strength than those in the composite. The exact mechanism by which the fiber strength is reduced during processing is unknown, and the fiber strengths as found from tensile testing of the composite will be used. However, the values of the parameters C and β found from the single fiber tests will be used to describe the subsequent time-dependent degradation of the fibers under stress-rupture. The fiber Weibull modulus m was set to 5, based on the values obtained from single fibers [43].

The parameter α was determined from analysis of the creep deformation of the composite as discussed in the previous section. The crack spacing z_0 was measured as well. The characteristic strength, σ_c, was determined using the method of Section 3.2.1. The interface frictional stress τ was set to 3.6 ksi.

Table XII. Parameters used in stress-rupture analysis

Temperature (°C)	σ_c (ksi)	z_0 (μm)	δ_c (μm)	α_{creep}
950	136	20	204	0.75
1050	133	20	201	0.75

The results of performing the analysis (i.e. the solution of Equations (64) and (68) as a function of time) with the described parameters is shown in Figure 74. It is evident that the model lifetimes are shorter by two orders of magnitude.

There are many assumptions in the model which cannot be verified independently of the composite stress-rupture data, chief among which are a) that fiber degradation is controlled by the growth of existing flaws, and b) that fiber degradation rates are unaffected by composite processing.

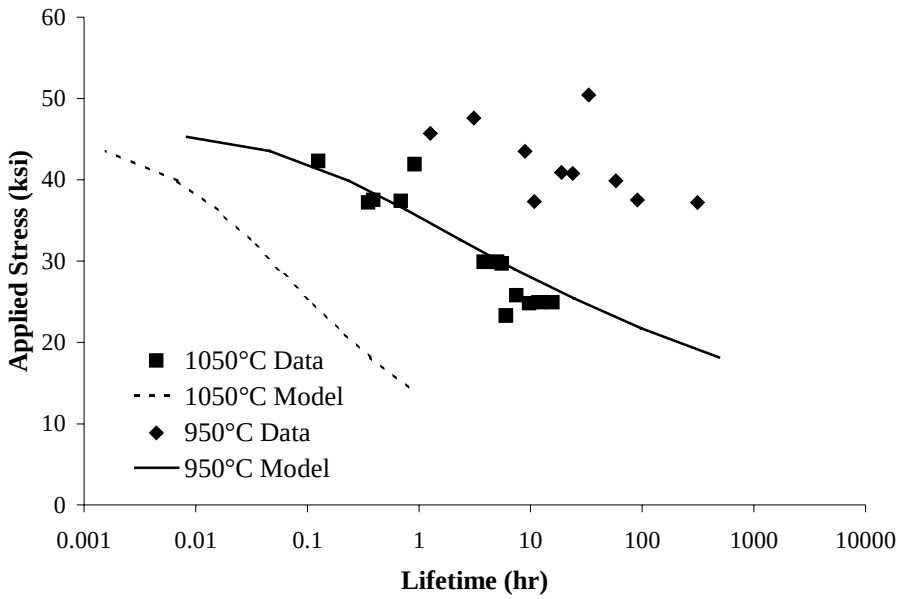

Figure 74. Comparison between model and experiment

If fiber stress-rupture failure is a result of microstructural changes which are unrelated to the flaws which govern quasi-static failure, then Equation (56), which is a relationship between current fiber strength and fiber stress history is no longer valid. Instead, some new relationship must be used. This relationship would probably be similar in form, that is, some sort of power law in stress, but the constants required, specifically initial strength (σ_i), Weibull modulus (m), and degradation constants (β and C) would have to be determined for this other mechanism.

Determining these parameters would require extensive testing of single fibers, both for stress-rupture lifetimes and for remaining strength after a given stress history. To determine the scaling of this damage mechanism with fiber length, a crucial element of the model, these tests would have to be run for fibers of a variety of lengths. Such a data set would provide information about the fiber strength degradation with time which could then be used in the stress-rupture model. At this time, no such data set exists.

If the same flaw population does control both tensile and rupture lives, there are many parameters which affect the stress-rupture lifetime. The stress-rupture lifetime is a function of the parameters listed in Section 3.2.2, namely C, β, α, z_0, m, σ_c, and τ. The relationship between the normalized time used in the analysis and the real time measured in the laboratory is a function of C, K_{Ic}, and β. Examination of the magnitude of the effects of these parameters in Section 3.2.2 indicates that only β will have a significant effect on the normalized stress-rupture lifetime. This value was obtained from testing on as-received single fibers. Testing on processed single fibers is impossible, as the fibers cannot be extracted from the composite. This makes any effects on the fiber due to processing difficult to quantify. The effect of annealing Nextel 610 fibers at 1093°C in an air environment for 100 hours was examined by Goldsby et al. [72] and implied that there was a reduction in creep rate at elevated temperatures coupled with an increase in lifetime. However, the increases in fiber lifetime were much less than an order of magnitude, as shown in Figure 75. While the composites are processed at approximately 1093°C, the total exposure time is less than 5 hours.

The relationship between the lifetime measured in the laboratory, t, and the normalized lifetime used in the model, $\tilde{t}$, is

$$\tilde{t} = \frac{t}{CY^2 K_{Ic}^{\beta-2} \sigma_c^2 \left(\frac{\beta}{2} - 1 \right)}. \tag{58}$$

It was assumed in deriving the fiber degradation equation that the geometric factor, Y, is independent of crack size. While this assumption has been shown to be inaccurate [73], the variations in Y with crack size are insufficient to create a large change in predicted life.

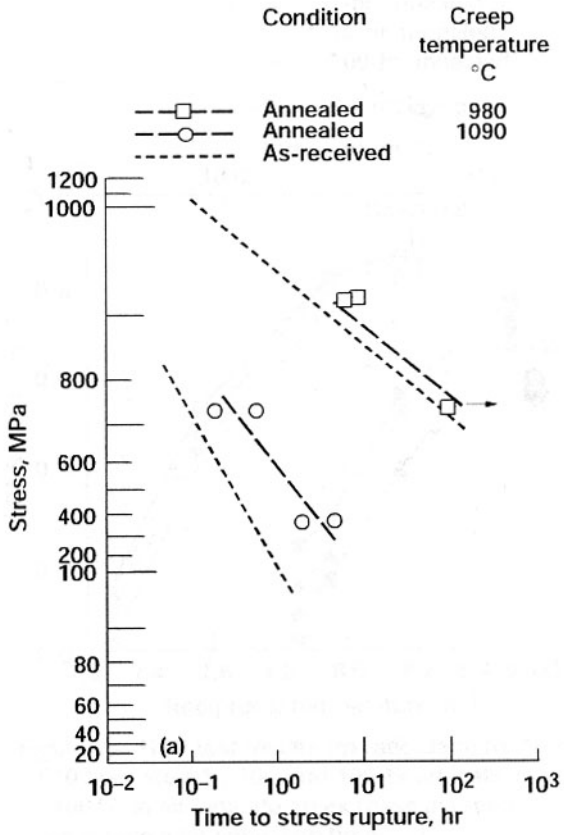

Figure 75. Effect of annealing on stress-rupture lifetime of Nextel 610 fiber [72]

If the parameter C is changed by a factor of 100, the model predictions more closely match the experimental data, as shown in Figure 76. No mechanism for this effect is proposed, although excellent agreement with experiments is a result of this empirical modification of the theory. It may be possible, for example, to run a small number of stress-rupture tests at relatively high temperatures, then use the theory to extrapolate the behavior to low stresses. While this eliminates the fully predictive capability of the model, such a procedure may still be of benefit for evaluating the stress-rupture behavior of new materials.

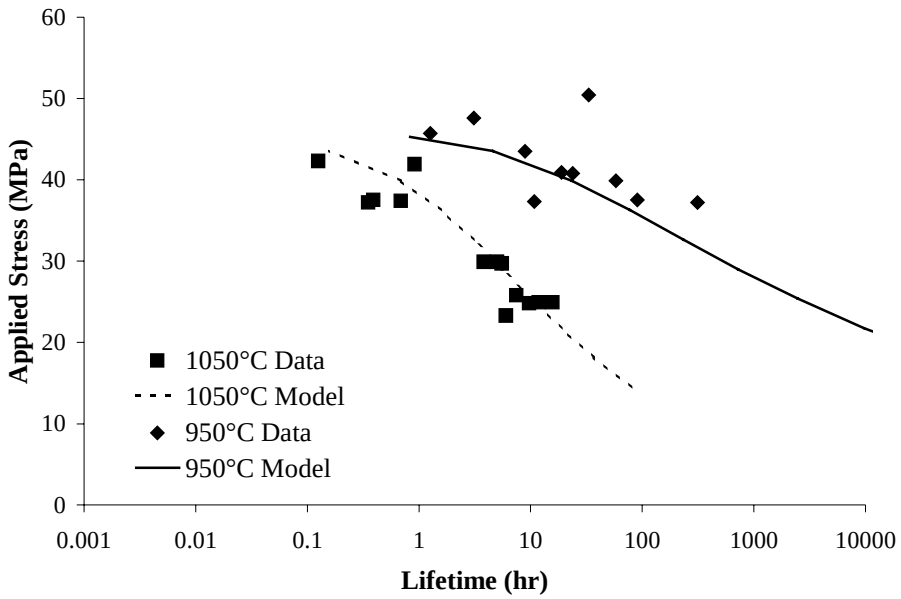

Figure 76. Effect of altering normalized timescale on the comparison between model and experiment

5.4.3 Tertiary Creep

As damage accumulates in the composite, the stress on the intact fibers increases. An example of this increase in stress is shown in Figure 77, which plots the fiber stress at a matrix crack, T, against normalized time, $\tilde{t}$ using the proposed stress-rupture model for two applied stresses. The creep rate as a function of time can then be determined using Equation (80). The resulting creep rates for two stress-rupture tests at 1050°C are shown in Figure 78, along with experimental data. Due to the large differences in predicted and measured lifetimes, the predicted lifetimes are increased by two orders of magnitude by changing the value of the parameter C as discussed in the previous section. While the measured strain rates differ slightly from the predicted strain rates, the trends are nearly identical. This indicates that tertiary creep observed in these materials is due to fiber damage increasing near the end of life.

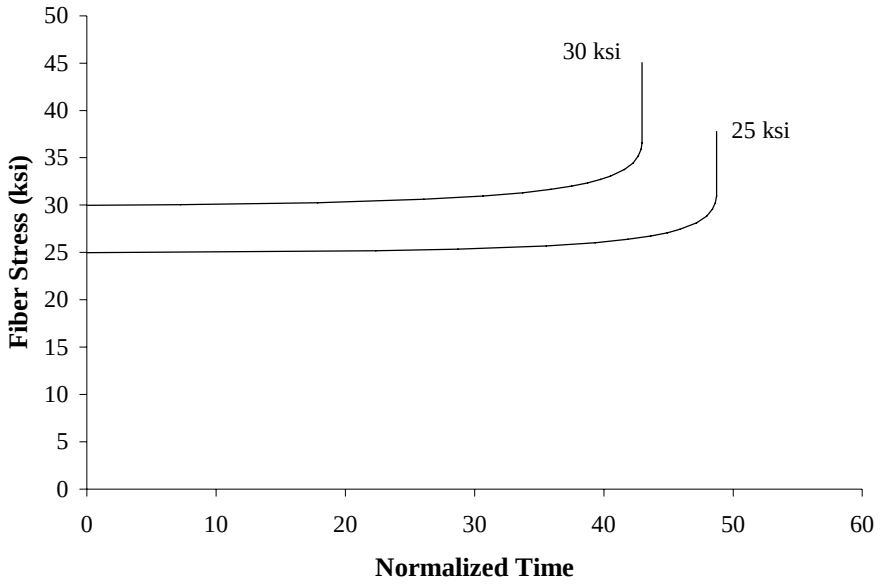

Figure 77. Fiber stress as a function of time

5.4.4 Residual Strength

The analytic model will also provide residual strength values. This can be done by simply increasing the value of the applied stress σ_{app} in the equilibrium equation (Equation (68)) until no solutions to intact fiber stress T exist. The residual strength tests run at 1050°C along with the model predictions are shown in Figure 79. As with the tertiary creep data, the composite lifetime has been scaled by a factor of 100 to provide better lifetime matching with experiment. Three lines are shown, corresponding to the variations in initial composite strength. The central line is for the mean strength (53.7 ksi), while the two outer lines represent specimens with a strength variation of one standard deviation (±7.9 ksi). Much of the variation in remaining strength and measured lifetime can be explained as a direct result of the variations in initial composite strength.

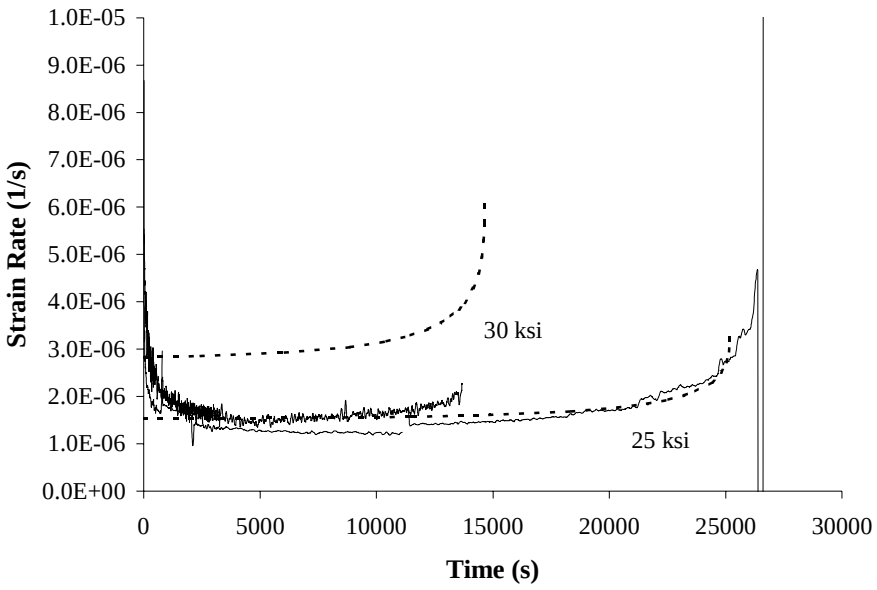

Figure 78. Comparison of composite creep rate with experimental data

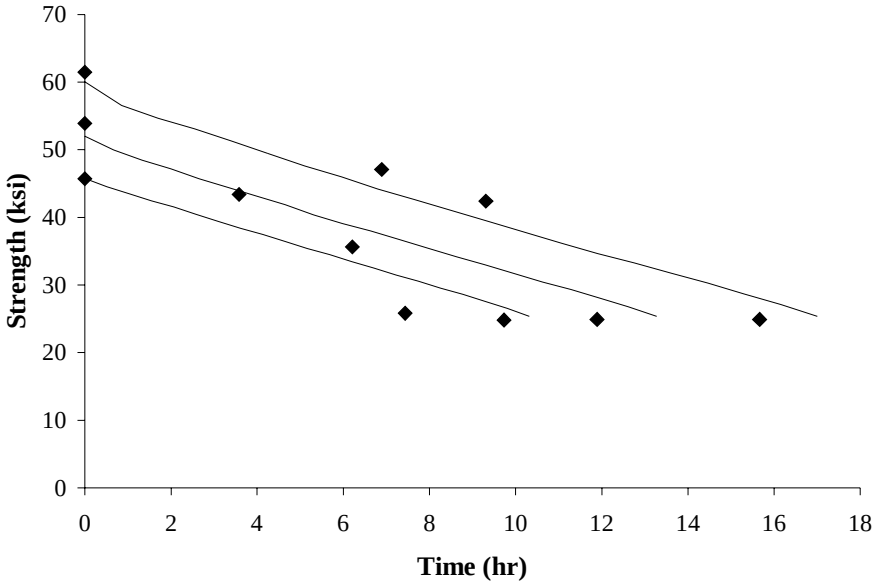

Figure 79. Predicted and measured residual strength values

5.4.5 Summary of Comparisons of Model and Experiment

The stress-rupture model depends on seven experimentally determined parameters:

- The single fiber rupture parameters (C and β),
- The fiber characteristic strength in the composite (σ_c),
- The fiber Weibull modulus (m),
- The interface frictional stress (τ),
- The matrix contribution (α), and
- The crack spacing (z_0)

Six of these parameters were determined independently of the stress-rupture testing. The seventh, α, was determined through examination of the measured creep strain rates. Using the model detailed in Section 3.2.2 with these parameters resulted in predicted lifetimes which were two orders of magnitude shorter than those measured experimentally. However, by increasing the value of the parameter C by 100, the model lifetimes match quite well the experimental lifetimes. With this single change in the input parameters, the tertiary creep rates and the remaining strength after an interrupted stress-rupture test were also well matched by the model. Thus, while the model is not truly predictive in nature, it can be used to explain many experimental observations of the stress-rupture process in ceramic composite materials.

Chapter 6 Woven and Crossply Composites

Although unidirectional composites are well-suited for laboratory examination, more complicated geometries, such as crossply or quasi-isotropic layups, are commonly used in applications. Therefore, it is useful to extend the models derived in Chapter 3 to these configurations. As a first step, the behavior of a cross-ply material will be examined in the context of time-dependent strength. Using established relationships between crack surface tractions and crack displacements, the stresses on fibers bridging cracks in crossply materials will be examined. The fiber stresses will lead to fiber degradation in the composite due to processes similar to those described earlier and the potential for fiber damage-driven crack growth will be examined. Finally, the woven materials tested in stress-rupture at 1093°C will be examined and the lifetimes compared to the unidirectional stress-rupture results.

6.1 Approach

A schematic of the problem defining the parameters used in the analysis is shown in Figure 80. For a crack of length *c*, with a bridged length *a*, we wish to determine the crack shape *u(x)*. In the bridged region, the fibers will exert closure tractions *p(x)* on the crack surface. Crack growth is determined by the stress intensity factor at the crack tip, *K*.

The equation which we consider gives the equations of shape for a 2-D crack in plane stress with a crack opening displacement *u(x)* and surface tractions *p(x)* under uniform remote stress σ_∞. The displacement is related to the traction as follows [74]:

$$u(x) = \frac{4\left(1-\nu^2\right)}{\pi E}\int_x^c \frac{s}{\sqrt{s^2-x^2}}\left\{\int_0^s \frac{\sigma_\infty - p(t)}{\sqrt{s^2-t^2}}dt\right\}ds, 0 \le x < c\,. \tag{90}$$

Additionally, the stress intensity factor at the crack tip is

$$K = 2\sqrt{\frac{c}{\pi}}\int_0^c \frac{\sigma_\infty - p(x)}{\sqrt{c^2 - x^2}}dx\,. \tag{91}$$

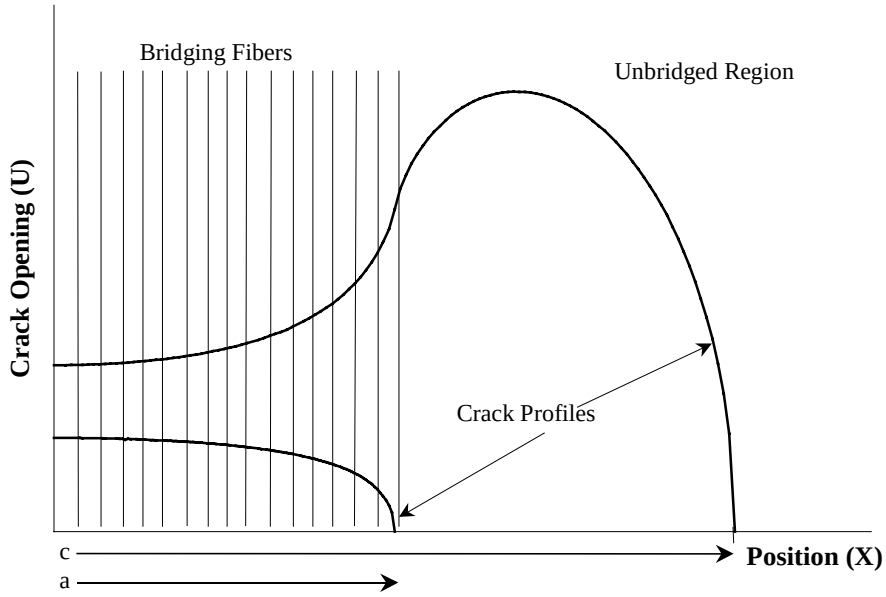

Figure 80. Schematic of bridged cracks

The tractions on the crack face are, in turn, determined by the displacements on the crack surface. Danchaivijit and Shetty have derived a stress-displacement relationship which is given by [28]

$$p(u) = \frac{\eta\sigma_\infty}{2(1+\eta)}\left\{\left[1+\frac{16(1+\eta)^2 E_f f^2 \tau u}{\eta^2\sigma_\infty^2 r}\right]^{\frac{1}{2}} + 1\right\}, \tag{92}$$

where η is a parameter

$$\eta = \frac{fE_f}{(1-f)E_m}\,. \tag{93}$$

Normalizing the stresses and displacements and substituting the bridging law into the crack shape relationship yields an integral equation for *U(X)*

$$U(X) = \frac{\gamma C}{S}\int_X^1 \frac{s}{\sqrt{s^2 - X^2}}\int_0^s \frac{\eta + 2 - \left[\eta^2 + 4(1+\eta)U(X)\right]^{1/2}}{\sqrt{s^2 - t^2}}dtds\,, \tag{94}$$

where γ, C, U, and S are given by

$$\gamma = \frac{4}{3(1+\eta)}, \tag{95}$$

$$C = \frac{c}{c_0};\ c_0 = \pi\left(\frac{K_{cm}}{\alpha}\right)^{\frac{2}{3}}(1-f)^2(1+\eta)^2, \tag{96}$$

$$U = \frac{u(x)}{u_0};\quad u_0 = \frac{\sigma_\infty^2 r}{4(1+\eta)E_f f^2 \tau}, \tag{97}$$

$$S = \frac{\sigma_\infty}{\sigma_0};\quad \sigma_0 = \left(\alpha K_{cm}^2\right)^{1/3},\ \alpha = \frac{6(1-\nu^2)\pi E_f f^2(1-f)(1+\eta)^2}{rE_m}. \tag{98}$$

Note that σ_0 is the ACK matrix cracking stress, Equation (8) [6].

Reversing the order of integration allows replacement of the double integral with two single integrals. This improves the convergence of the equation and reduces the run time required to obtain a solution.

$$U(X) = \frac{4C}{3S(1+\eta)}\left[\int_0^X \left[2+2\eta-P(X)\right]\ln\left|\frac{\sqrt{1-t^2}+\sqrt{1^2-X^2}}{\sqrt{t^2-X^2}}\right|dt + \int_X^1 \left[2+2\eta-P(X)\right]\ln\left|\frac{\sqrt{1-t^2}+\sqrt{1^2-X^2}}{\sqrt{X^2-t^2}}\right|dt\right],$$

$$P(X) = \left[\eta^2 + 4(1+\eta)U(x)\right]^{\frac{1}{2}} + \eta. \tag{99}$$

The solution technique is iterative. A proposed crack shape, *U(X)*, is substituted into the right hand side of Equation (99), and the equation evaluated numerically. The new crack shape on the left hand side is compared to the initial crack shape. If the two differ by more than some predetermined value at any point along the crack profile, a weighted average of the two profiles is taken. This new crack shape is again substituted into the right hand side and the process repeated until the crack shape converges.

As an example of the technique, the critical stress for crack advance in the Nextel 610/ alumina-yttria composite was determined. For the elastic parameters found experimentally for the unidirectional oxide/oxide materials at room temperature, η is 3.1.

Determining the normalization parameters c_0 and σ_0 for the unidirectional oxide materials is difficult, due to uncertainties about the matrix composition. It has been suggested by Rice [75] that the fracture toughness of porous alumina should show an exponential behavior,

$$\gamma_I = \gamma_0 e^{-bP} \tag{100}$$

similar to the porosity dependence of elastic modulus (Equation (84)). The data in the literature has extremely wide scatter, with *b* ranging from 1.5 to 10 and with little data in the high porosity (> 20%) regime (see [76]). Average values are approximately 3.5, which is similar to the porosity dependence of elastic modulus. Given an 'ideal' (zero porosity) toughness of 4 MPa$\sqrt{m}$, the toughness of a 40% porous material should be approximately 1.0 MPa$\sqrt{m}$. Pabst [77] determined that the toughness of monolithic alumina with a similar porosity was 1.3 MPa$\sqrt{m}$. The predicted matrix cracking stress, found by using Equations (98), is σ_0 = 83 ksi. Given the well-established matrix damage in the virgin materials and the measured tensile strength of 56 ksi, verification of this value could not be determined. The predicted normalizing distance is c_0 = 61 µm. Given a 50% fiber volume fraction and a 12µm fiber diameter, a crack of this size would be bridged by two or three fibers.

Figure 81 shows the calculated matrix cracking stress of the unidirectional materials. For long cracks, the predicted stress is nearly identical to the ACK matrix cracking stress, but for short to intermediate cracks, the DS expression results in higher stresses. The fact that short cracks require a higher than normal stress to propagate was noticed previously by Marshall et al. [7].

6.2 Growth of Cracks in Crossply/Woven materials

Although unidirectional materials are simpler to analyze, woven and crossply materials are more commonly used in applications. In chapter 2 the damage progression in a crossply composite was illustrated (Figure 4). This behavior can be modeled using this approach by setting the bridging stresses to zero over the unbridged region (i.e. the 90° ply).

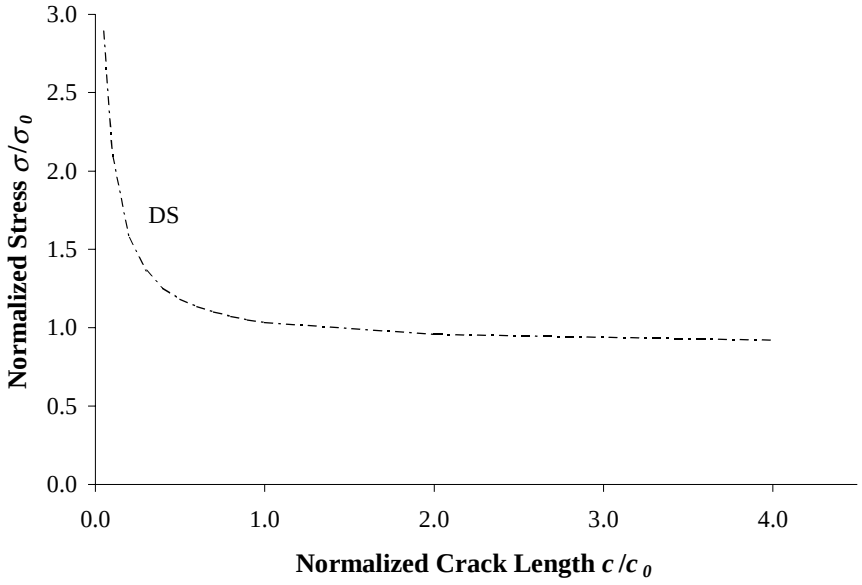

Figure 81. Predicted matrix cracking stress as a function of initial crack length in the unidirectional oxide/oxide materials

Crack growth under stress rupture conditions is an important consideration in composite materials, especially in materials with fiber and/or interfaces sensitive to environmental degradation. Morscher [79], for example, has noted a 'multi-planar' fracture surface in silicon carbide reinforced silicon carbide composites at intermediate temperatures and stresses in air, illustrated in Figure 82. The current belief is that although matrix cracks can form at these temperatures and stresses, they do not cross the entire composite cross

section upon formation due to the effect of the bridging fibers. Under stress-rupture, however, they can grow, although in this case the cracks do not propagate through more than one or two tows before composite failure takes place. Morscher has noted that many cracks appear to terminate within a 90° tow [78]. In these materials oxidative effects on the fiber/matrix interface will affect the behavior of the fibers, but crack growth will still be governed by the stress intensity factor at the crack tip.

Figure 82. Multi-planar fracture in SiC/SiC composite [79]

The crack size under the initial quasi-static load will depend on the applied stress and the distribution of the bridging fibers. Two cases are considered, crack growth from a 90° ply into a 0° ply and vice versa. The quasi-static behavior is illustrated in Figure 83 which shows the critical stress required to propagate a fully formed 90° ply crack into a 0° ply and Figure 84 which shows the reverse problem. The figures show calculations for two composites, a crossply Nextel 610/alumina-yttria composite with mechanical properties identical to the materials studied experimentally and a SiC/SiC composite similar to those tested by Morscher. The composite parameters are given in Table XIII.

Table XIII. Parameters used in the analysis of crack growth composites

Property	Oxide composite	SiC/SiC composite
E_f	54 ksi	39 ksi
E_m	18 ksi	45 ksi
f	0.248	0.342
σ_0	83 ksi	42 ksi
c_0	61 μ	78 μ
tow width	120 μ	152 μ
C	1.97	1.95
η	0.989	0.452

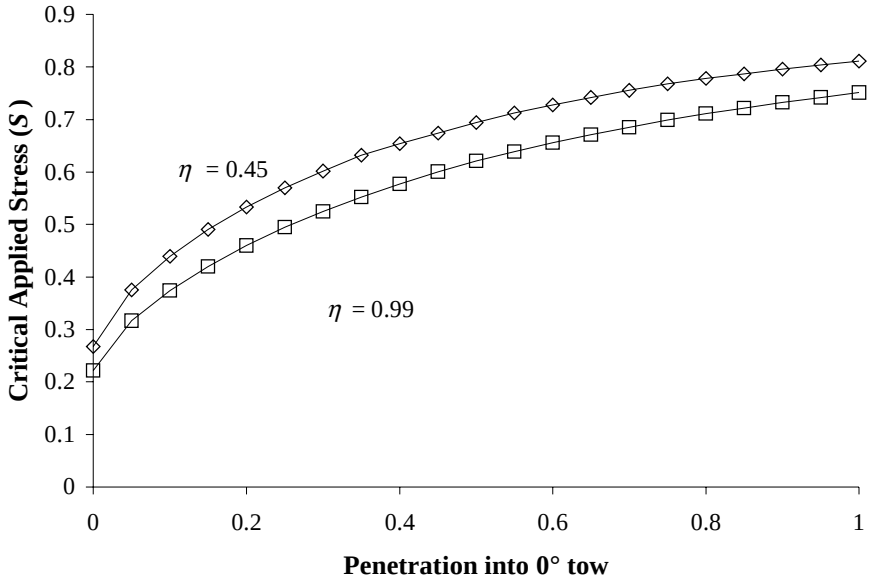

Figure 83. Crack penetration into 0° ply

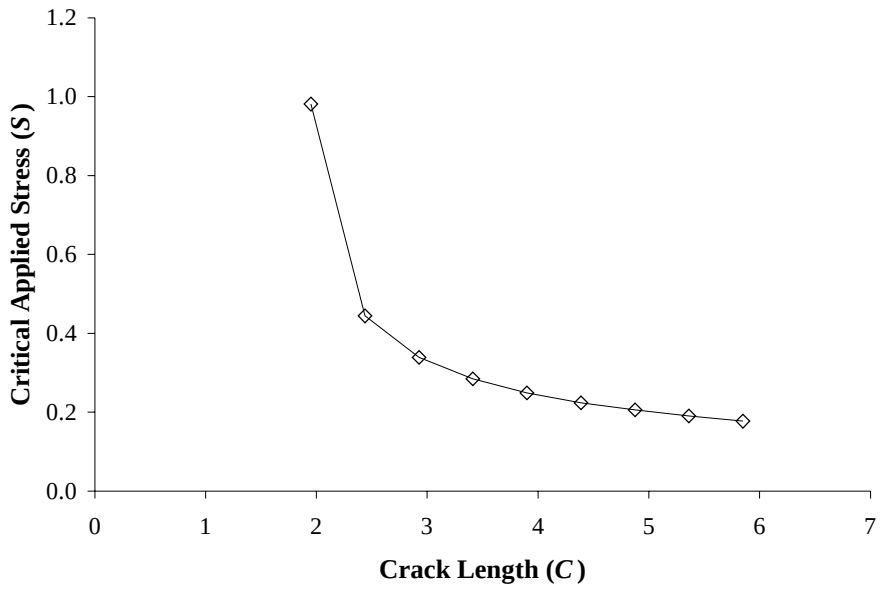

Figure 84. Critical stress required for crack advance from 0° ply into 90° ply for SiC/SiC materials

While stable crack growth under a gradually increasing applied load is possible if the crack is initially in the 90° ply, growth from a 0° ply into a 90° ply does not seem possible in quasi-static tension. Under stress-rupture conditions, however, stable crack growth may occur as a result of decreases in the bridging stresses on the crack due to failure of the bridging fibers.

The degradation of silicon carbide fibers in a composite exposed to a high temperature air environment is a complex problem involving oxidation, mass transport, and other issues which has not been completely solved. Nevertheless, it is instructive to attempt to model the growth of these cracks in the context of the stress-rupture model derived in Chapter 3.

To examine crack growth as a result of fiber degradation and failure, an approach based on tracking the damage as a function of position was used. The composite was divided into *2N* nodes along the direction of crack propagation with *N* nodes in a 0° tow and *N* nodes in the adjacent 90° tow. A matrix crack was placed in one of the tows with a crack

tip at the interface and a stress applied to the model. The fibers were assumed to degrade according to a power law, identical to the slow crack growth models described in Chapter 3. Once the crack shape was found through iteration, the time was incremented and the probability of fiber failure at each node was determined. The bridging law at each point was modified by the fraction of fibers remaining intact. Fiber failure leads to increased crack opening and therefore a larger stress intensity factor at the crack tip. Consequently, there may be crack advance should the stress intensity factor exceed the critical stress intensity factor. This is illustrated schematically in Figure 85.

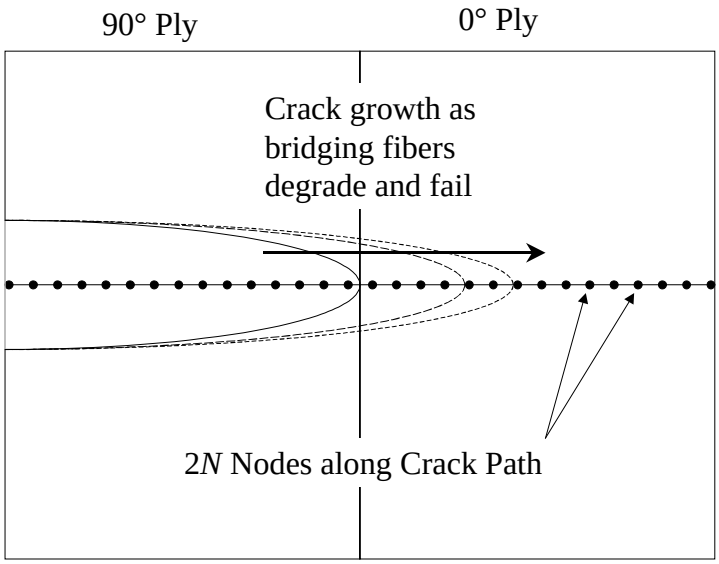

Figure 85. Schematic of analysis of crack growth

The matrix cracking parameters used in this examination were those used for the SiC/SiC materials as given in Table XIII. The degradation and failure properties were varied slightly from run to run to determine the sensitivity to the fiber behavior. The parameters used were:

m = 5, 10

β = 5, 10

$\sigma_c = 10\ \sigma_0$

Equation (47) was used to determine the probability of fiber failure with the applied stress T given by the bridging stress $p(x)$ divided by the fiber volume fraction. However, there

is no reason why a different expression for fiber failure could not be used. Pullout was ignored for simplicity.

As shown in Figure 86, which plots the crack penetration into the 90° ply with time for a crack originating in the 0° ply, this case does not undergo steady-state crack advance. Instead, after a period of fiber degradation, the crack propagated rapidly through the 90° ply. The value of β used in the calculations displayed was 5, and similar results were found with a value of 10. The applied stresses were taken to be 25% and 50% of the matrix cracking stress, σ_0, which would correspond to approximately 16% and 32% of the ultimate tensile strength of the composite.

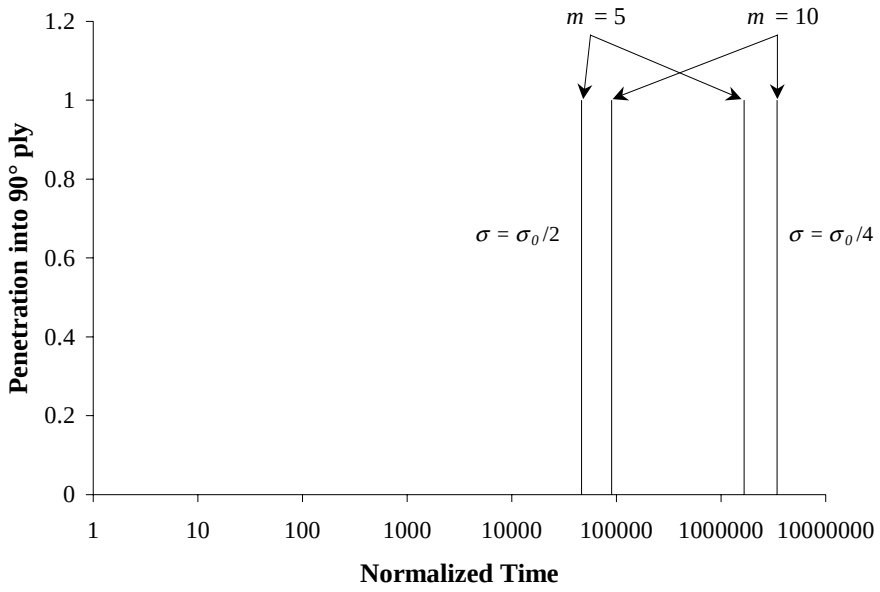

Figure 86. Crack penetration into 90° ply under stress-rupture conditions

For a crack originating in the 90° ply and penetrating the 0° ply it is seen that steady-state crack advance is possible. In Figure 87, the time-dependent crack size at an applied stress of 50% of the ACK matrix cracking stress (32% UTS) for m = 5 and m = 10 with β = 5 is shown. Figure 88 shows the percentage of fibers surviving as a function of position after

the crack has penetrated completely through the 0° ply. Near the interface between the 0° and 90° plies, fiber failure is a virtual certainty.

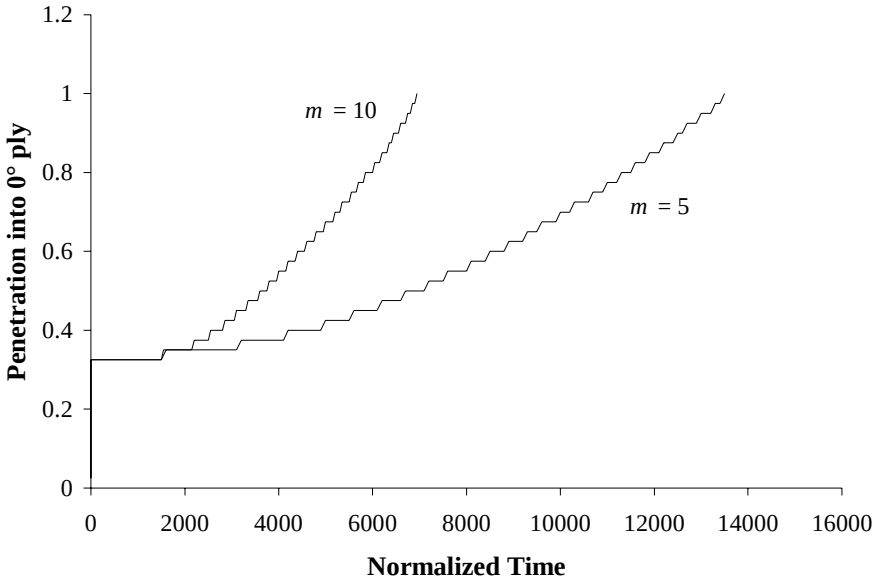

Figure 87. Crack penetration into 0° ply under stress-rupture conditions

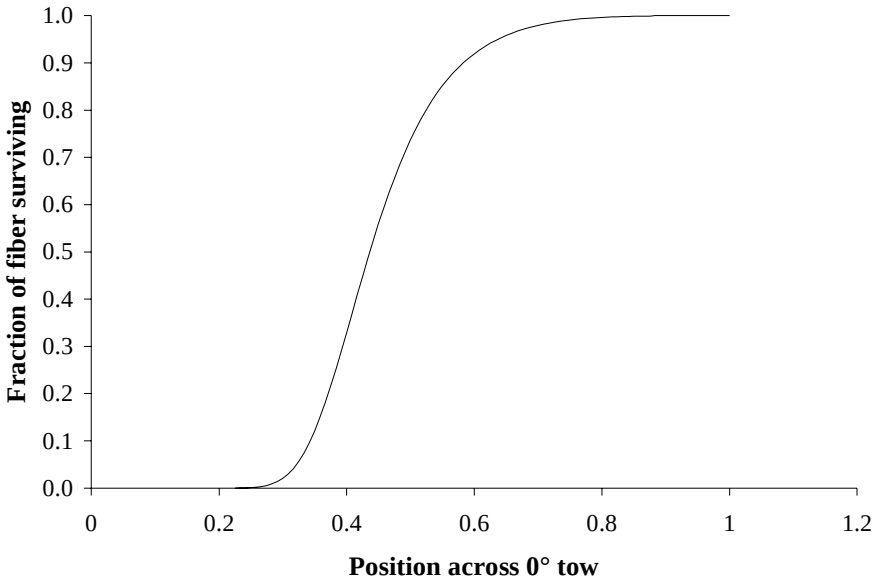

Figure 88. Fiber damage across 0° tow in stress-rupture

Once the crack tip has passed completely through the 0° ply, it propagates rapidly through the next 90° ply. At this point, the crack can behave in one of two ways. It can propagate rapidly through the 0° ply, or it can propagate stably. In the example shown in Figure 88, approximately half of the reinforcing fibers in the central 0° ply have broken by the time the crack has propagated completely through the 0° ply. Given this, it is reasonable to assume that further propagation will be rapid, leading to a crack which passes completely through the matrix. However, component failure will still be governed by failure of the reinforcing fibers. The stress-rupture behavior of a composite with such a crack is the subject of the next section.

6.3 Modeling of 'Through' Cracking

This solution technique can also be used to examine the behavior of a matrix crack which extends across the entire composite (i.e. has no crack tip). A model which consists of many alternating 0° and 90° plies can be used to approximate a crossply composite. If there are enough layers in the model, the effect of the crack tip at plies far behind the tip is negligible.

Crack shapes for cracks which have penetrated several plies of a SiC/SiC composite are shown in Figure 89. Figure 90 shows the critical stress required for crack advance as a function of crack size. The periodicity is evident, indicating that there is a steady-state effect wherein the behavior far behind the crack tip is unaffected by changes at the crack tip. Therefore, by analyzing a sufficiently large crack, the through matrix crack can be simulated. The possibility of failure of the bridging fibers has not been considered.

One important consideration in a crossply composite is the stress concentration which occurs on the fibers at the interface between the 0° and 90° plies. This increased stress is a result of the increased displacement in the 90° plies due to the lack of bridging in those

regions. The stress across a 0° ply for a through crack is shown in Figure 91. The stress concentration is the ratio of the stress at the edge of the ply (x = 0.5 in Figure 91) to the applied stress.

The stress concentration at the 0°/90° interface for a through crack at a variety of applied stresses and values of η is shown in Figure 92. The stress concentration decreases with increasing applied stress and with increasing η.

The stress concentration on the fibers at the ply interfaces can have a large effect on composite strength and stress-rupture life. This is especially true for composites where the ACK stress is a significant fraction of the ultimate strength.

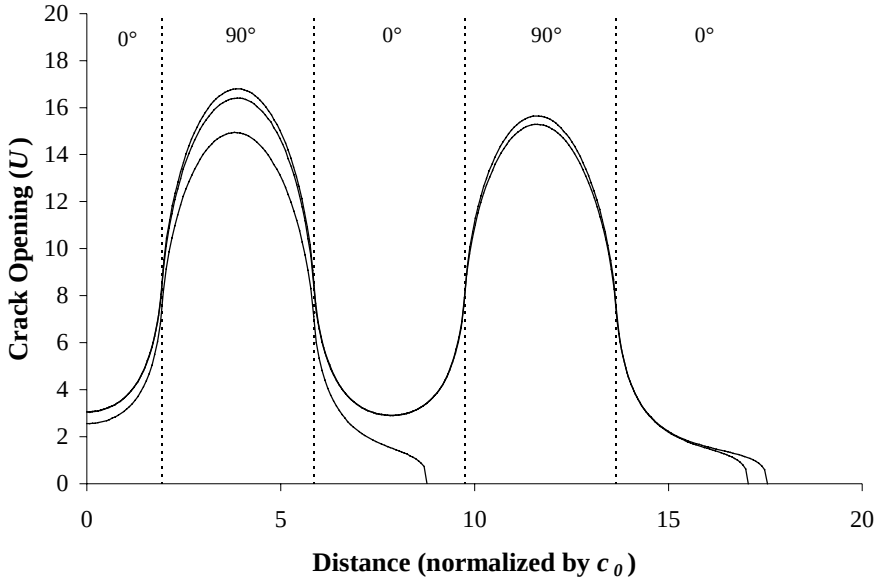

Figure 89. Crack shape of a crack penetrating through many 0° and 90° plies

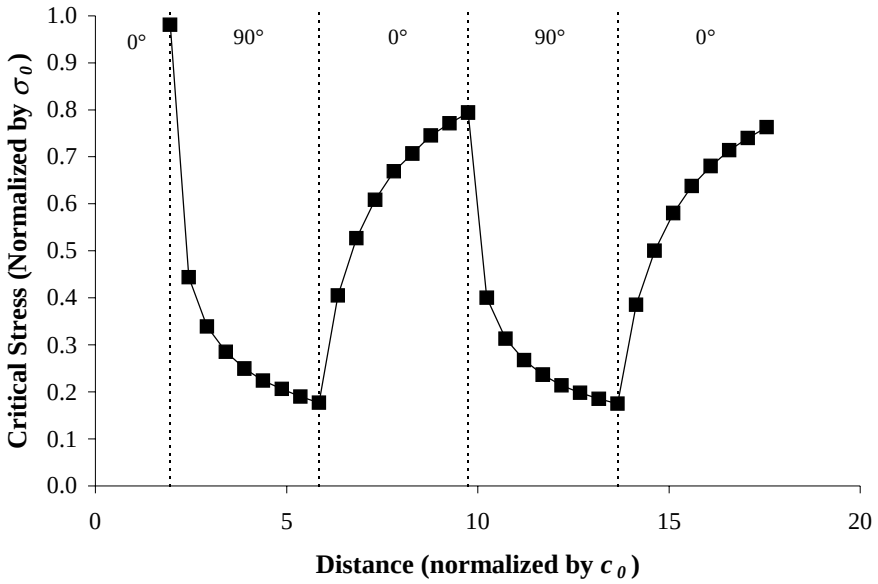

Figure 90. Critical stress required for crack advance as a function of crack size in a crossply composite

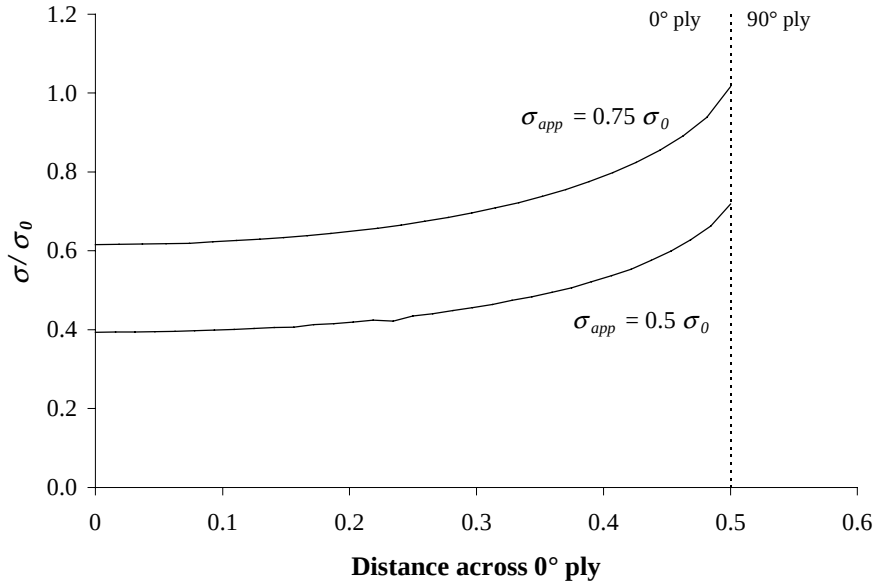

Figure 91. Stress as a function of position in 0° ply

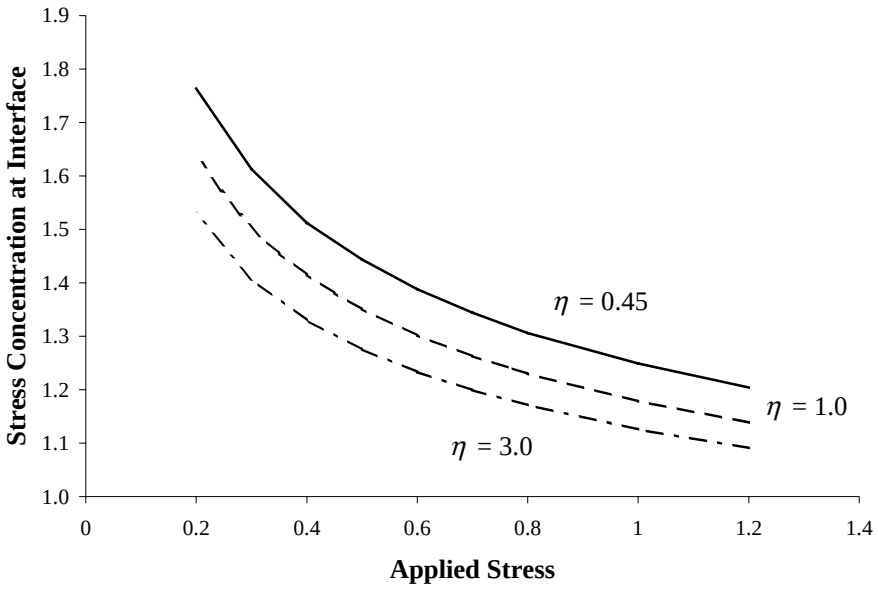

Figure 92. Stress concentration at 0°/90° ply interface

The woven Nextel 610 composite studied in this work has an ACK matrix cracking stress for the 0° tows of approximately 36.3 ksi. The measured tensile strength of the composite at 1093°C is 29.9 ksi. The stress concentration at the ply interfaces for this applied stress is 1.23, as shown in Figure 92. Thus, the strength measured for the crossply materials would be $(1.23)^{-1}$ of the strength expected for a composite with an equivalent volume fraction of fibers equally spaced. Given the measured tensile strength of 29.9 ksi and an axial fiber volume fraction of 12.4%, the characteristic fiber strength, σ_c, is calculated to be 339 ksi, using Equation (68) with the measured crack spacing of 150 µm. This is much larger than the characteristic fiber strength measured in the unidirectional materials, which was 135 ksi. The reasons for this large increase in strength in the woven materials is unclear, although it exists at both ambient and elevated temperatures.

For the stress-rupture tests on the woven materials described in Chapter 5, the applied stresses range from 0.48 σ_0 to 0.72 σ_0. The stress concentrations at these applied stress

levels range from 25% to 40%. As there is no fiber data at 1093°C, the model was first used to fit rupture parameters to the unidirectional stress-rupture lives measured experimentally at the same temperature. The results of the curve fit are shown in Figure 93. The parameters used to produce the stress-rupture curve are

$C = 3.6 \times 10^{16}$, and

$\beta = 2.4$.

Based on the behavior of unidirectional materials at this stress level, and the stress concentration at the ply interface, the stress-rupture lifetimes for the woven materials as compared to the experimentally determined values are shown in Figure 94, along with the unidirectional data. The stress concentration is treated as a multiplier to the applied stress, yielding an effective stress which was then used to determine the stress-rupture lifetime. Thus, the increase in stress concentration at the ply interface with decreasing stress leads to a steeper stress-life curve, which is also observed experimentally. Additionally, the fiber rupture behavior observed in the unidirectional materials is still applicable to the woven materials, despite the large difference in tensile strength.

6.4 Summary

Some consequences of the effect of unbridged regions on the stress-rupture behavior of ceramic composites have been considered. Specifically, crack propagation due to fiber failure in the crack wake and stress concentrations at ply interfaces have been examined. For the oxide materials examined experimentally in Chapter 5, it is seen that the stress concentrations at the ply interface explain a great deal of the observed differences in stress-rupture lifetimes between unidirectionally reinforced composites and woven composites.

However, the current bridging model has many limitations. It is difficult to extend this model to problems involving materials of differing elastic moduli. While this is not a significant problem in SiC/SiC materials, where the moduli of the 0° and 90° plies are rather similar, in the oxide materials, this assumption is extremely poor. Additionally, Xia et al. have pointed out that bridging models of this type do not accurately represent materials with fiber slip lengths that are similar in length to the ply thickness [27].

Ultimately, it may become necessary to use a finite element model rather than the numeric solution currently used. A finite element model would allow the examination of plies of differing elastic moduli as well as incorporating the large-scale bridging effect of Xia et al.

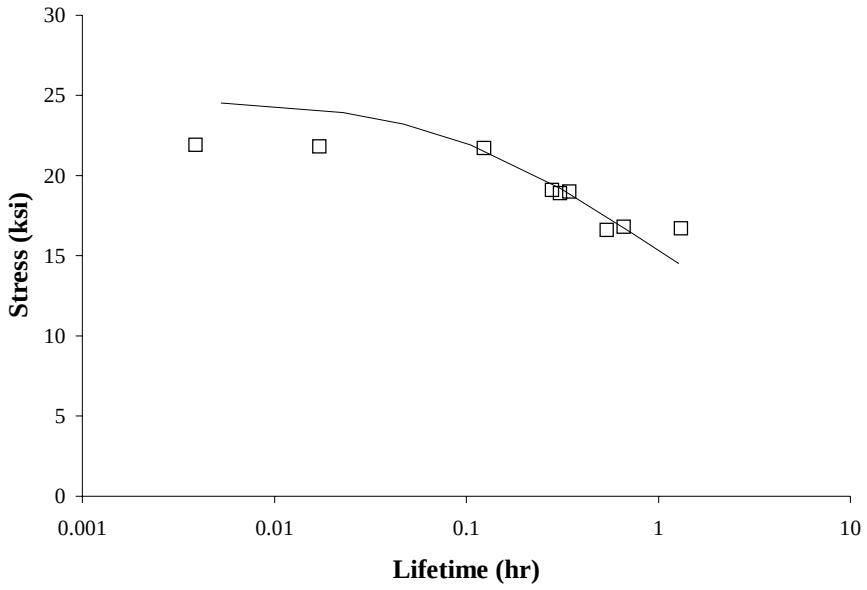

Figure 93. Rupture life for unidirectional composites at 1093°C

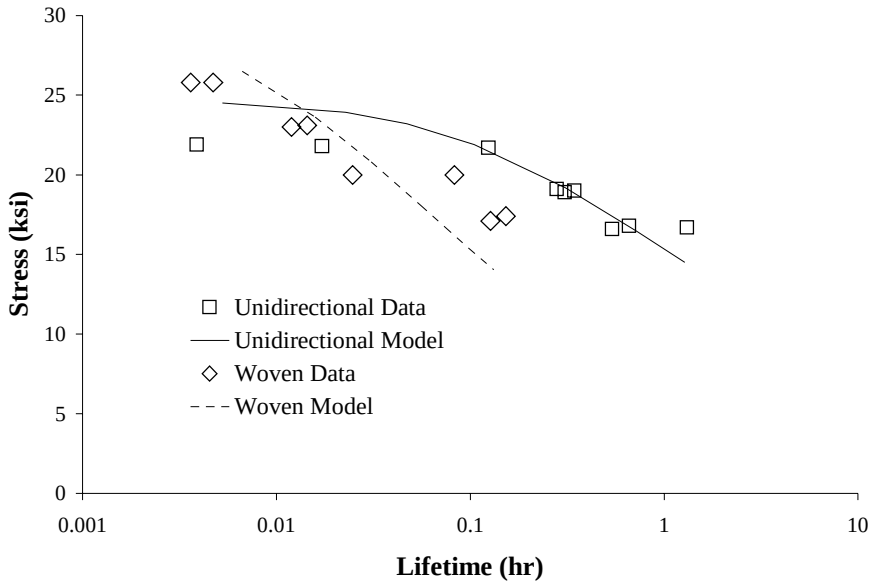

Figure 94. Stress-rupture of the woven materials derived from the behavior of the unidirectional materials

Chapter 7 Combining Damage Mechanisms

Thus far, we have considered only the fiber-dominated behavior in stress-rupture of composites. Although the comparisons to the data were fairly inaccurate in lifetime for the unidirectional materials, the deformation behavior was well matched. This, along with the other experimental evidence discussed in Chapter 4, implies that there are no other significant damage mechanisms in the material studied. However, as other systems are examined, it may be necessary to consider other means of damage in the composite. In this chapter, one possible method of dealing with two damage mechanisms is discussed. The behavior of unidirectional materials is considered, although using the principles discussed in the previous chapter, the behavior of crossply materials could be considered as well.

7.1 Fiber Creep as a Damage Mechanism

To provide a second damage mechanism for examination, a reduction in frictional shear stress at the interface is postulated as a damage mechanism. Evidence exists that asperities on the fiber surface affect the interface frictional stress [e.g. 80]. A simple relationship between asperity height and interface frictional stress has been proposed [81]

$$\tau = \mu A \frac{h_0}{r} \tag{101}$$

where μ is the coefficient of friction, A is a constant involving the elastic properties of the fiber and the matrix, and h_0 is a characteristic asperity height.

Fiber creep under stress-rupture conditions will result in fiber contraction due to volume conservation. As the matrix in a ceramic matrix composite is typically extensively cracked, it carries little load and thus does not creep. This implies that the contact between the fibers and the matrix will be reduced as the fiber creeps, reducing the

interface frictional stress. A similar effect can arise due to matrix shear creep, or, in fatigue loading conditions, wear at the interface [82]. It must be stated that no direct evidence exists to either confirm or deny the existence of this second mechanism under stress-rupture in oxide/oxide composites, it is merely representative of a second damage mechanism that could be present within the composite.

Given volume conservation, and a fiber creep rate governed by the power law

$$\dot{\varepsilon} = B\sigma_f^n, \tag{102}$$

the asperities on the fiber surface will be carried inward, leading to a reduction in the shear stress as a function of time and stress, using Equation (101) as a guide

$$\tau = \frac{\mu A}{r}\left[h_0 - \frac{1}{2}B\sigma_f^n t\left(r + h_0\right)\right]. \tag{103}$$

This has the effect of increasing the fiber slip length, and therefore the interaction between fiber breaks. This will thus also reduce the strength of the composite. Equation (12) for tensile strength can then be expressed as a function of time

$$\sigma_{ult} = f\left(\sigma_0^m l_0 \mu A\left[h_0 - \frac{1}{2}B\sigma_f^n t\left(r + h_0\right)\right]\right)^{\frac{1}{m+1}}\left(\frac{2}{m+2}\right)^{\frac{1}{m+1}}\left(\frac{m+1}{m+2}\right). \tag{104}$$

Thus, given an applied stress on the fibers, σ_f, the time to failure can be found by equating the applied stress to the ultimate stress.

7.2 Simulations and Analysis

Initially, the stress rupture lifetimes for slow crack growth and fiber creep acting independently at 1050°C were determined through the analytic representations of the previous sections. The constants required are given in Table XIV. Although the creep deformation properties of Nextel 610 fibers are well established, the value of the coefficient *B* was increased by approximately three orders of magnitude over the known

behavior at 1050°C. This was done to allow the damage modes to interact on similar time scales. If this action were not to be taken, failure of the composite would occur long before any changes in τ due to fiber creep (a situation which does appear to exist experimentally).

Table XIV. Parameters used for analysis and simulation

Parameter	Value
τ_0	3.6 ksi
z_0	20 μm
σ_c	133 ksi
m	5
α	0.75
β	2.4
$CY^2K_{Ic}{}^2$	2.5 x 10^{10} (psi^2 / s)
n	3
B	1.9 x 10^{-8} (1/ ksi^3)

Two stress levels were chosen, 50% and 60% of the ultimate tensile strength. These values were chosen in order that the lifetimes for each individual mechanism would be comparable and would thus yield the maximum interaction. The analytically determined residual strength curves are shown in Figure 95.

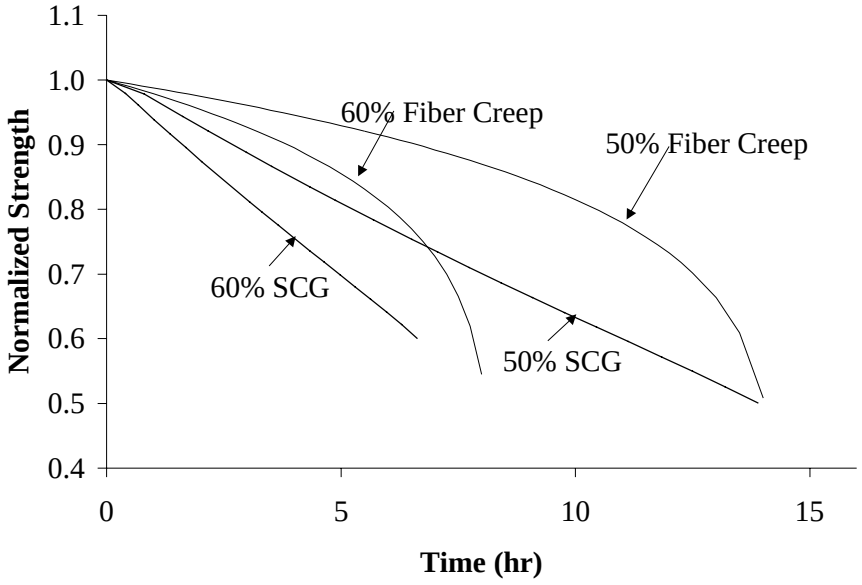

Figure 95. Remaining strength for two damage mechanisms at two stress levels.

We would like to be able to use the results from these micromechanical analyses as inputs to a phenomenological residual strength approach. To aid in this task, we fit the numerically calculated residual strength data for each mechanism (i.e. Figure 95) to an assumed form for a residual strength evolution law. A number of such evolution laws have been postulated (e.g. [83, 84]). Based upon the form of the residual strength curves resulting from the simulations, we assume that the residual strength evolution for the case of slow crack growth may be represented by a form of the so-called "wear-out" model, where

$$\frac{d\sigma_r}{dt} = -\frac{1}{\gamma_1 \hat{\tau}_1} \sigma_r^{1-\gamma_1} \left[1 - \left(\frac{\sigma_{app}}{\sigma_{uts}} \right)^{\gamma_1} \right], \tag{105}$$

where $\hat{\tau}_1$ is the average time to failure at an applied stress σ_{app}, σ_r is the current remaining strength, and γ_1 is a curve-fitting parameter. An identical expression is used for the fiber creep, with different values for the corresponding constants $\hat{\tau}_2$ and γ_2. The

results of curve-fitting Equation (105) to the numeric data in Figure 95 are given in Table XV.

Table XV. Wear-out model parameters

Mechanism	Stress Level	$\hat{\tau}_{1,2}$	$\gamma_{1,2}$
Slow Crack Growth	50%	14.0	0.76
Slow Crack Growth	60%	6.6	0.87
Interface Creep	50%	14.0	5.91
Interface Creep	60%	7.8	5.97

Strictly, it is not necessary at all to 'fit' the predicted degradation data to an analytic model. This is done merely as a convenience. All that is really required is the change in residual strength with time as a function of current strength. This information can be presented either as an equation, as is the case here, or as a tabulated list of data stemming from the previous micromechanical models from which degradation rates may be calculated numerically.

We now consider the effect of changing stress levels on the lifetimes by using the wear-out model parameters in Table XV. At a time of four hours, the stress was changed (from 50% UTS to 60% UTS (low-high)or the reverse (high-low)). The predictions from the wear-out model as compared to the analytical results are shown in Figure 96. The agreement is excellent.

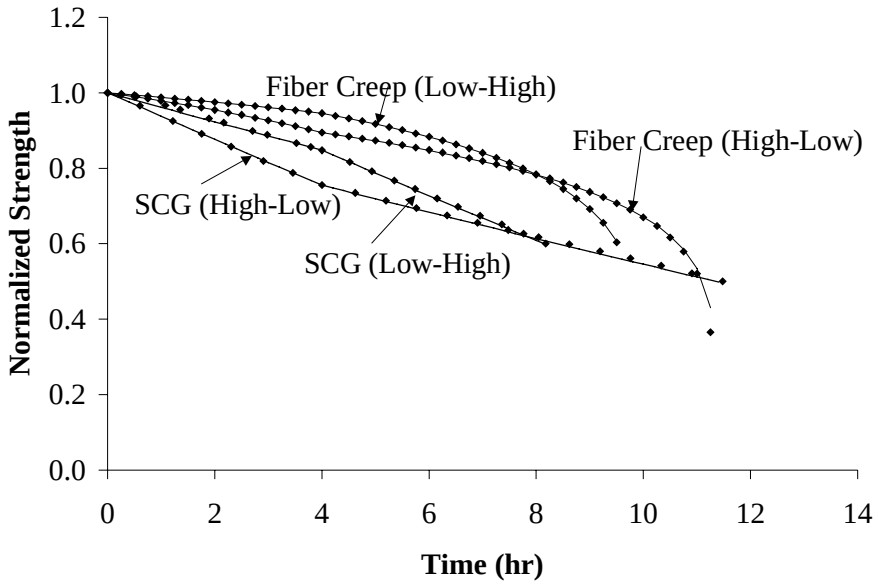

Figure 96. Sequence effects in stress-rupture

The main objective is to predict the composite lifetime when both mechanisms operate. To combine the damage mechanisms at the micromechanical level, we turn to Monte Carlo simulations, as there is no analytic model which does so. The technique used for the simulation is very similar to that of Curtin [85]. Briefly, the system is composed of an array of fibers running in the z-direction which have been discretized along their length into fiber elements. Each element is assigned a tensile strength according to the Weibull strength statistics of the fiber and a random number generation routine. A fiber element breaks when the stress it carries exceeds its strength. When this occurs, the load the element carries is reduced to zero and the load is shared equally among all intact fibers in the plane (i.e. global load sharing is used). The load-carrying capacity of the matrix is neglected. Fiber strength degradation is governed by Equation (56) and the strength of each fiber element is tracked individually as a function of the stress applied to that element. The change in τ will affect the recovery of stress from broken fibers through Equation (3).

The Monte Carlo simulation is then run for a 625 fiber composite with 160 elements in the z-direction. The physical composite length in the z-direction was set to be $4\delta c$ where δ_c is given by Equation (15).

We wish to predict the results from the combined simulation using only the fits to the simulation results from the individual mechanisms. To do so, we assume that the rate of change of residual strength for the multiple mechanism case may be written as the sum of the individual rates of change. For the specific case of the two wear-out models for strength degradation (i.e. slow crack growth and fiber creep), this implies that

$$\frac{d\sigma_r}{dt} = -\frac{1}{\gamma_1 \hat{\tau}_1} \sigma_r^{1-\gamma_1} \left[1 - \left(\frac{\sigma_{app}}{\sigma_{uts}} \right)^{\gamma_1} \right] - \frac{1}{\gamma_2 \hat{\tau}_2} \sigma_r^{1-\gamma_2} \left[1 - \left(\frac{\sigma_{app}}{\sigma_{uts}} \right)^{\gamma_2} \right]. \tag{106}$$

The results of such a prediction for the combined mechanisms is shown in Figure 97. As indicated, the model overpredicts the lifetime by approximately 30% at both stress levels. Similar overpredictions exist for the sequence effect with combined damage mechanisms as shown in Figure 98. The general trend in residual strength as generated by the simulations is not matched by Equation (106).

We also wish to compare the results from the wear-out model, despite its deficiencies, to the predictions using a linear damage accumulation rule, which states that the sum of the life fractions governs failure. When the normalized time for the two mechanisms sum to unity, the composite fails:

$$1 = \frac{t}{t_{SCG}} + \frac{t}{t_{Fiber\,Creep}}. \tag{107}$$

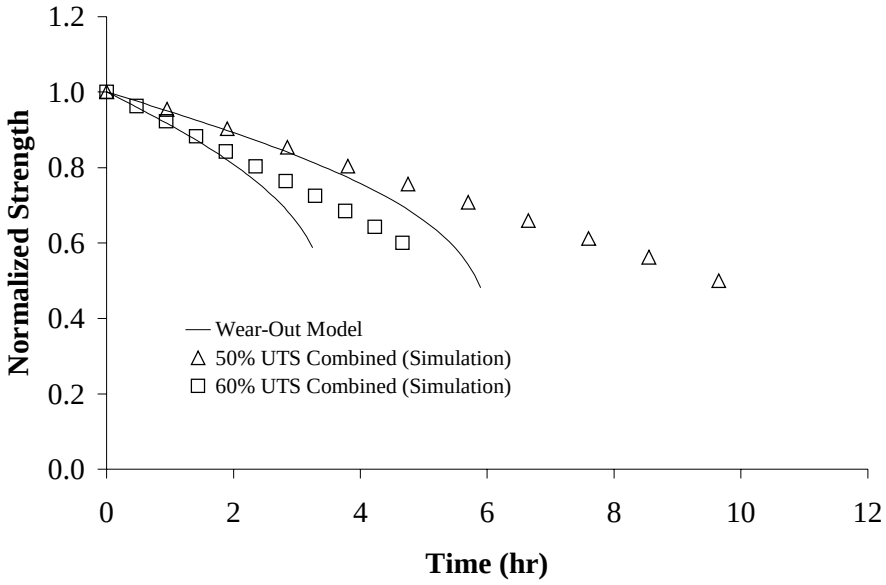

Figure 97. Wear-out model for combined damage mechanisms at constant stress level

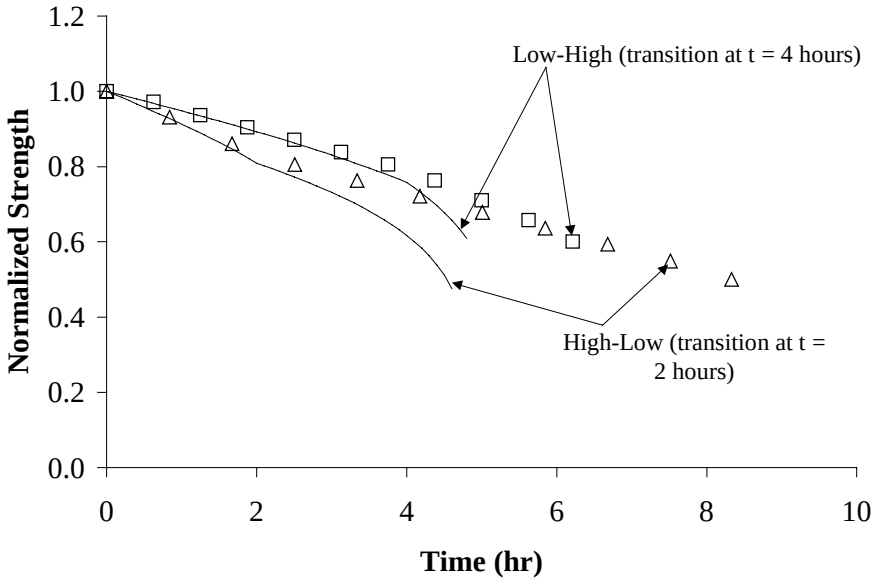

Figure 98. Wear-out model for combined damage mechanisms with sequence effect

As the linear damage accumulation rule makes no statement about the strength of the material during stress-rupture, only the predicted lifetimes can be compared. This is done in Table XVI. As is evident, the wear-out model more closely predicts the stress-rupture lifetimes than linear damage accumulation for the individual mechanisms under sequence effects, but linear damage accumulation is slightly more accurate when the mechanisms are combined.

In an attempt to quantify the applicability of the model, similar analyses were performed for a variety of slow crack growth exponents. The lifetime under this mechanism was kept constant at approximately 14 hours for the 50% UTS condition, equivalent to the lifetime due to fiber creep at that stress level, by changing the parameter C. The wear-out exponent, γ, was then determined for each value of β and used in a similar set of load conditions. The exponents are listed as a function of slow crack growth exponent, β, in Table XVII. The relative error between the phenomenological model and the simulations for the combined damage mechanisms at 50% UTS is shown in Figure 99. This figure indicates that the accuracy of the wear-out model is dependent on how similar the exponents for the two mechanisms are. The residual strengths obtained during some of the simulations are shown in Figure 100.

Table XVI. Comparison of wear-out model to Miner's Rule

Stress-Rupture Condition	Simulation Lifetime	Wear-out Lifetime	Linear Damage Accumulation
Slow Crack Growth (High-Low)	11.2	11.4	10.8
Slow Crack Growth (Low-High)	7.9	8.2	9.6
Interface Creep (Low-High)	9.5	9.5	8.7
Interface Creep (High-Low)	11.2	11.0	9.5
Combined Mechanisms (High)	4.7	3.5	3.6
Combined Mechanisms (Low)	9.7	5.9	7.0
Combined Mechanisms (Low-High)	6.2	4.9	5.5
Combined Mechanisms (High-Low)	8.3	3.3	3.6

Table XVII. Wear-out model exponent, γ, as a function of slow crack growth exponent, β

Slow Crack Growth Exponent, β	Wear-out Model Exponent, γ
2.4	0.763
3.5	1.794
5	3.127
7.5	4.944
10	6.260
12.5	7.230
15	7.343

7.3 Summary

A wear-out model has been proposed to represent degradation in strength during stress-rupture. The model accurately matches the sequence effects caused by changing stress levels for two separate damage mechanisms. For the effect of damage mechanisms acting simultaneously, the accuracy of the model is dependent on the relative values of the exponents of each mechanism acting individually. The model is most accurate when the two exponents are identical.

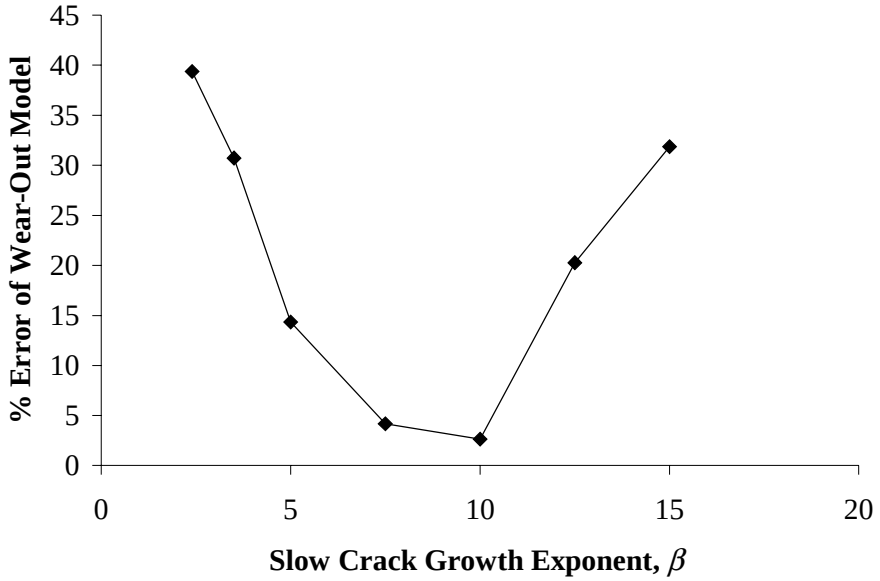

Figure 99. Accuracy of wear-out model as a function of slow crack growth exponent, β

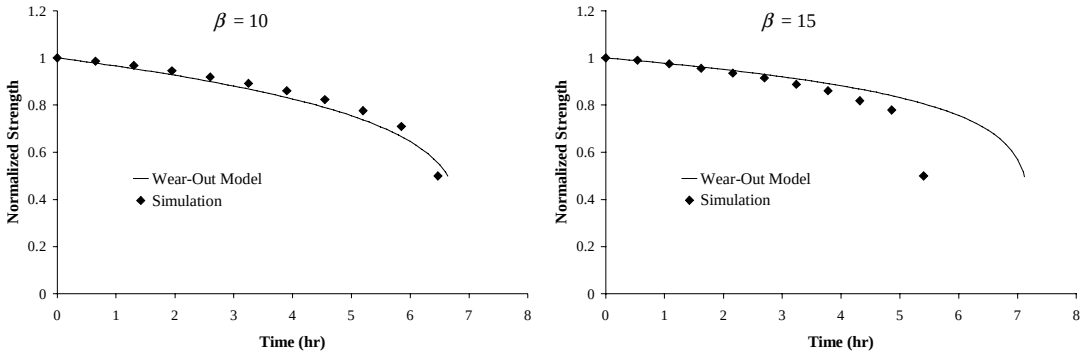

Figure 100. Residual strength from both model and numeric simulation

Chapter 8 Conclusions and Future Work

8.1 Conclusions

In this work, the stress rupture behavior of an oxide/oxide ceramic matrix composite system was studied both experimentally and analytically. A rupture model which incorporates fiber degradation and matrix damage in a unidirectional composite was derived and the model predictions compared to the results of an extensive experimental program. The model was further extended to the behavior of cross-ply or woven materials and again compared to experimental results. Finally, an empirical method for predicting the durability of materials which exhibit multiple damage modes is examined and compared to results of Monte Carlo simulations. The conclusions for the three main analytic aspects of this work will first be discussed in detail. Then, some important questions raised by this work will be posed and some future work which may serve to answer some of these questions will be proposed.

8.1.1 Stress-Rupture Modeling

The stress-rupture model derived in this work incorporates many experimentally observed phenomenon in ceramic matrix composites:

- Fiber statistical strength distribution as described by Weibull statistics
- Matrix cracking and the resulting fiber stress profile
- Fiber pullout and global load transfer from broken fibers

Although the model predictions are rather different from the experimentally observed stress-rupture lifetimes, the model does correctly predict the magnitude of secondary creep. With a single fitting parameter, the model can be used to correctly describe the

stress-rupture lifetimes of the composite, and also correctly predicts the transition from secondary to tertiary creep.

8.1.2 Woven and Cross-ply Composites

Although unidirectional materials are preferred in analytical work, more complex geometries, such as cross-ply materials, will be preferred in service. The behavior of a cross-ply composite was examined through the use of a bridging law which represents the fibers bridging a matrix crack as crack surface tractions. The cross-ply material was found to exhibit a stress concentration on the fibers at the interface between the 0° and 90° ply. This stress concentration was found to be a function of the globally applied stress. The stress-rupture lifetimes observed in woven composites was shown to be directly related to the behavior of unidirectional composites when the applied stress is scaled by the stress concentration.

8.1.3 Analytic Representations of Stress-Rupture Under Combined Damage Mechanisms

The system examined experimentally in this work appears to exhibit only fiber degradation as a damage mechanism. Other systems may experience additional damage mechanisms. Analytic representations of their combined effect may be difficult to derive or require extensive computations. A need exists for simple methods which are accurate enough to be used with confidence and straightforward enough to be used for finite element schemes. A second damage mechanism was introduced for purposes of examining such a method. The simple method proposed was to simply use an analytic form to represent the change in remaining strength of each individual damage mechanism, and combine the changes in remaining strength analytically when both

mechanisms are operative. It was shown that such a method is generally not sufficiently accurate save for the case when the two mechanisms produce similar changes in remaining strength (i.e. the simple analytic representations are similar in magnitude). However, the method was sufficient for representing the durability under a single damage mechanism where the applied stress was changed during the rupture test.

8.2 Questions Raised and Future Work

8.2.1 Stress-Rupture Modeling

While the proposed stress-rupture model can be fit to the experimental data, a need exists for a truly predictive model, where the stress-rupture behavior of a composite can be determined solely from experiments on the constituents and quasi-static tension tests on the composite. The reason for the failure of the model to accurately predict the lifetime of the composite is troubling. Several potential difficulties in obtaining the requisite micromechanical data were pointed out, chief among which is: *What is the true degradation behavior of the fibers in the composite?* The single fiber stress-rupture lives used in the model predictions are much shorter than the composite predictions. There appears to be no way to increase the predicted lives through changing the parameters of the model. Obtaining an understanding of how the fibers degrade and the changes in fiber strength with time is crucial for improving the accuracy of the model.

Single fiber testing should be performed on Nextel 610 fibers at a variety of stresses and temperatures. Ideally, the residual strength during the stress-rupture test should be found as well. Residual strength tests will provide information about the degradation mechanism which cannot be found from lifetime alone.

8.2.2 Woven and Cross-ply Composites

To produce the predictions for the cross-ply materials, the stress on the node adjacent to the 0°/90° ply interface was used in either a strength or stress-rupture model. This ignores the behavior of the other fibers in the ply. The degradation of these other fibers would increase the stress on the critical node, affecting the stress-rupture life. Additionally, this model does not consider the large-scale bridging effect, which has been shown to affect the stress concentration at the ply interface. Both large-scale bridging and a more complete treatment of fiber degradation and failure is necessary. Finite element models incorporating large-scale bridging and fiber degradation should be created and examined.

8.2.3 Analytic Representations of Stress-Rupture Under Combined Damage Mechanisms

In order to use micromechanical models in structural-level durability analyses, the extensive computation time must be reduced. It has been shown that the proposed degradation relationship is sufficient to describe the single mechanism, it cannot describe the degradation under multiple mechanisms except in specific cases. Given the relatively straightforward nature of the two mechanisms used in this work, it should be possible to produce an accurate analytic representation of the two mechanisms acting simultaneously. The results of such an analysis should provide guidance for combining the mechanisms through the simpler method proposed here.

References

1. CFCC Program Overview, Oak Ridge National Laboratory (1988) http://www.ms.ornl.gov/cfcc/brochure/cfccbroch.pdf
2. He, M. –Y., Hutchinson, J. W., "Crack Deflection at an Interface Between Dissimilar Elastic Materials" *Int. J. Solids Struct.*, Vol. 25 (1989) pp. 1053-1067.
3. Ahn, B. K., Curtin, W. A., Parthasarathy, T. A., Dutton, R. E., "Criteria for Crack Deflection/Penetration for Fiber-Reinforced Ceramic Matrix Composites", *Comp. Sci. Tech*, Vol. 58 (1998) pp. 1775-1784.
4. Ahn, B. K., Unpublished Work
5. Hutchinson, J. W., Jensen, H. M., "Models of Fiber Debonding and Pullout in Brittle Composites with Friction" *Mech. Matl.*, Vol. 9, pp. 139-163 (1990).
6. Aveston, J., Cooper, G. A., Kelly, A., "Single and Multiple Fracture" The Properties of Fibre Composites, Conference Proceedings, National Physical Laboratory, Guilford, U.K., pp. 15-26, (1971).
7. Marshall, D. B., Cox, B. N., Evans, A. G., "The Mechanics of Matrix Cracking in Brittle-Matrix Fiber Composites", *Acta metall.*, Vol 33, pp. 2013-2021 (1985).
8. Daniel, I. M., Anastassapoulous, G., Lee J.-W., "The Behavior of Ceramic Matrix Fiber Composites Under Longitudinal Loading," *Comp. Sci. Tech.*, Vol. 46, pp. 105-113 (1993).
9. Beyerle, D. S., Spearing, S. M., Zok, F. W., Evans, A. G., "Damage and Failure in Unidirectional Ceramic-Matrix Composites," *J. Am. Ceram. Soc.*, Vol. 75, pp. 2719-2725 (1992).
10. Curtin, W. A., "Multiple Matrix Cracking in Brittle Matrix Composites", *Acta metall. mater.*, Vol. 41, pp. 1369-1377 (1993).
11. Ahn, B. K., Curtin, W. A., "Strain and Hysteresis by Stochastic Matrix Cracking in Ceramic Matrix Composites", *J. Mech. Phys. Solids*, Vol. 45, pp. 177-209 (1997).

12. Kuo, W. –S., Chou, T. –W., “Multiple Cracking of Unidirectional and Cross-Ply Ceramic Matrix Composites”, *J. Am. Ceram. Soc.*, Vol. 78, pp. 745-755 (1995).
13. He, M. Y., Wu, B. –X., Evans, A. G., Hutchinson, J. W., “Inelastic Strains due to Matrix Cracking in Unidirectional Fiber-Reinforced Composites”, *Mech. Matl.*, Vol. 18, pp. 213-229 (1994).
14. Marshall, D. B., “Analysis of Fiber Debonding and Sliding Experiments in Brittle Matrix Composites”, *Acta metall. mater.*, Vol. 40, pp. 427-441 (1992).
15. Evans, A. G., Domergue, J. –M., Vagaggini, E., “Methodology for Relating the Tensile Constitutive Behavior of Ceramic-Matrix Composites to Constituent Properties”, *J. Am. Ceram. Soc.*, Vol. 77, pp. 1425-1435 (1994).
16. Vagaggini, E., Domergue, J. –M., Evans, A. G., “Relationships Between Hysteresis Measurements and the Constituent Properties of Ceramic Matrix Composites: I, Theory”, *J. Am. Ceram. Soc.*, Vol. 78, pp. 2709-2720 (1995).
17. Domergue, J. –M., Vagaggini, E., Evans, A. G., “Relationships Between Hysteresis Measurements and the Constituent Properties of Ceramic Matrix Composites: II, Experimental Studies on Unidirectional Materials”, *J. Am. Ceram. Soc.*, Vol. 78, pp. 2721-2731 (1995).
18. Curtin, W. A., "Theory of Mechanical Properties of Ceramic-Matrix Composites", *J. Amer. Ceram. Soc.*, Vol. 74, pp. 2837-2845 (1991).
19. Curtin, W. A., "Ultimate Strengths of Fibre-Reinforced Ceramics and Metals", *Composites*, Vol. 24, pp. 98-102 (1993).
20. Curtin, W. A., Zhou, S. J., “Influence of Processing Damage on Performance of Fiber-Reinforced Composites”, *J. Mech. Phys. Sol.*, Vol. 43, pp. 343-363 (1995).
21. Thouless, M. D., Evans, A. G., “Effects of Pull-out on the Mechanical Properties of Ceramic-Matrix Composites”, *Acta metall.*, Vol. 36, pp. 517-522 (1988).
22. Curtin, W. A., “The Tough to Brittle Transition in Brittle Matrix Composites”, *J. Mech. Phys. Sol.*, Vol. 41, pp. 217-245 (1993).

23. Weitsman, Y., Zhu, H., “Multi-Fracture of Ceramic Composites”, *J. Mech. Phys. Sol.*, Vol. 41, pp. 351-388 (1993).
24. Zhu, H., Weitsman, Y., “The Progression of Failure Mechanisms in Unidirectionally Reinforced Ceramic Composites”, *J. Mech. Phys. Sol.*, Vol. 42, pp. 1601-1632 (1994).
25. Curtin, W. A., Ahn, B. K., Takeda, N., “Modeling of Brittle and Tough Stress-Strain Behavior in Unidirectional Ceramic Matrix Composites”, *Acta mater.*, Vol. 46, pp. 3409-3420 (1998).
26. Xia, Z. C., Carr, R. R., Hutchinson, J. W., “Transverse Cracking in Fiber-Reinforced Brittle Matrix Cross-Ply Laminates”, *Acta metall. mater.* Vol. 41, pp. 2365-2376 (1993).
27. Xia, Z. C., Hutchinson, J. W., Evans, A. G., Budiansky, B. “On Large Scale Sliding in Fiber-Reinforced Composites”, *J. Mech. Phys. Sol.*, Vol. 42, pp. 1139-1158 (1994).
28. Danchaivijit, S., Shetty, D. K., “Matrix Cracking in Ceramic-Matrix Composites”, *J. Am. Ceram. Soc.*, Vol. 76, pp. 2497-2504 (1993).
29. Danchaivijit, S., Shetty, D. K., Eldridge, J., “Critical Stresses for Extension of Filament-Bridged Matrix Cracks in Ceramic Matrix Composites: An Assessment with a Model Composite with Tailored Interfaces,” *J. Amer. Ceram. Soc.*, Vol. 78, pp. 1139-1146 (1995).
30. Dowling, N. E., “Mechanical Behavior of Materials”, Prentice-Hall, USA (1993).
31. McLean, M., *Directionally Solidified Materials for High Temperature Service*, The Metals Society, (1989).
32. Du, Z. Z., McMeeking, R. M., “Creep Models for Metal Matrix Composites with Long Brittle Fibers”, *J. Mech. Phys. Sol.*, Vol. 43, pp. 701-726 (1995).
33. Fabeny, B., Curtin, W. A., “Damage Enhanced Creep and Rupture in Fiber-Reinforced Composites”, *Acta mater.*, Vol. 44, pp. 3439-3451 (1996).

34. Iyengar, N. I., Curtin, W. A., "Time-Dependent failure in Fiber-Reinforced Composites by Matrix and Interface Shear Creep", *Acta mater.*, Vol. 45, pp. 3419-3429, 1997.

35. Begley, M. R., Evans, A. G., McMeeking, R. M., "Creep Rupture in Ceramic Matrix Composites with Creeping Fibers", *J. Mech. Phys. Sol.*, Vol. 43, pp. 727-740 (1995).

36. Evans, A. G., Blumenthal, W., "High Temperature Failure in Ceramics" *Fracture Mechanics in Ceramics*, Vol. 6, pp. 423-448 (1977).

37. Wilkinson, D. W., "Creep Damage Mechanisms in Structural Ceramics" *Fracture Mechanics of Ceramics*, Vol. 10, pp. 349-366 (1992).

38. Wang, J. S., Stephens, J. J., Nix, W. D., "A Statistical Analysis of Cavity Nucleation at Particles in Grain Boundaries", *Acta metall.*, Vol. 33, pp. 1009-1021 (1985).

39. Evans, A. G., Rana, A., "High Temperature Failure Mechanisms in Ceramics" *Acta metall.*, Vol. 28, pp. 129-141 (1980).

40. Iyengar, N. I., Curtin, W. A., "Time-Dependent Failure in Fiber-Reinforced Composites by Fiber Degradation", *Acta metall. mater.*, Vol. 45, pp. 1489-1502 (1997).

41. Experimental Product Data Sheet, 3M Corporation, "1500 Denier 170 Sized 12 µm Nextel ™ 610 Roving"

42. Wilson, D. M., "Statistical Tensile Strength of Nextel™ 610 and Nextel™ 720 Fibres", *J. Mat. Sci.*, Vol. 32, pp. 2535-2542 (1997).

43. Xu, Z. R., Chawla, K. K., Li, X., "Effect of High Temperature Exposure on the Tensile Strength of Alumina Fiber Nextel 610", *Mat. Sci. Eng. A*, Vol. 171, pp 249-256 (1993).

44. Das, G., "Thermal Stability of Single Crystal and Polycrystalline Alumina Fibers and 85 Al_2O_3 - 15% SiO_2 Fibers", *Cer. Eng. Sci. Proc.*, Vol. 16, pp. 977-986 (1995).

45. Das, G., "Stability of Polycrystalline Nextel 720 Fiber", *Cer. Eng. Sci. Proc.*, Vol. 17, No. 4, pp. 25-34 (1996)

46. Goldsby, J. C., Morscher, G. N., "Thermomechanical and Microstructural Stability of Nextel 610 Polycrystalline Alumina Fiber", in *Proceedings of the 17th Conference on Ceramic and Metal Matrix Composites*, pp. 437-447 (1993).

47. Wilson, D. M., Lieder, S. L., Lueneburg, D. C., "Microstructure and High Temperature Properties of 85% Al_2O_3 - 15% SiO_2 Fibers", *Mat. Res. Soc. Symp*, Vol. 350, pp. 89-98 (1994).

48. Wilson, D. M., Lueneburg, D. C., Lieder, S. L., "High Temperature Properties of Nextel 610 and Alumina-Based Nanocomposite Fibers", *Cer. Eng. Sci. Proc.*, Vol. 14, pp. 609-621 (1993).

49. Yun, H. M., Goldsby, J. C., DiCarlo, J. A., "Stress-Rupture Behavior of Small Diameter Polycrystalline Alumina Fibers", *Advances in Ceramic Matrix Composites*, Ceramic Transactions, Vol. 34, pp. 713-725 (1994).

50. Yun, H. M., DiCarlo, J. A., "Time/Temperature Dependent Tensile Strength of SiC and Al_2O_3-Based Fibers", *Advances in Ceramic Matrix Composites III*, Ceramic Transactions, Vol. 74, pp. 17-25 (1996).

51. Weiderhorn, S.M., French, J.D., Luecke, W.E., "A Comparison of Fracture Mechanism Maps with the Larson-Miller Method of Predicting Lifetime", *Cer. Eng. Sci. Proc.*, Vol. 16, pp. 691-698 (1995).

52. Fareed, A. S., Schiroky, G. H., "Microstructure and Properties of Nextel™ 610 Fiber Reinforced Ceramic and Metal Matrix Composites", *Cer. Eng. Sci. Proc.*, Vol. 15, pp. 344-352 (1994).

53. Jenkins, M. G., Kohles, S. S., "High-Temperature Performance and Retained Strength of an Oxide/Oxide Continuous Fiber Ceramic Composite" *Cer. Eng. Sci. Proc.*, Vol. 19, pp. 317-325 (1998).

54. Campbell, C. X., Jenkins, M. G., "Use of Unload/Reload Methodologies to Determine the Effect of Thermal Degradation on *In Situ* Constituent Properties and Performance of an Oxide/Oxide CMC" *To Appear in* Environmental, Mechanical,

and Thermal Properties of Continuous Fiber Ceramic Composite (CFCC) Materials and Components, ASTM STP 1392, (2000).

55. Lu, T. -J., "Crack Branching in All-Oxide Ceramic Composites" *J. Amer. Ceram. Soc*., Vol. 79, pp. 266-274 (1996).
56. Tu, W. -C., Lange, F. F., Evans, A. G., "Concept for a Damage-Tolerant Ceramic Composite with "Strong" Interfaces" *J. Amer. Ceram. Soc.*, Vol. 79, pp. 417-424 (1996).
57. Lee, S. S., Zawada, L. P., Hay, R. S., Staehler, J., "High Temperature Mechanical Behavior and Characterization of an Oxide/Oxide Composite" Submitted *J. Amer. Ceram. Soc.*
58. Kramb, V. A., John, R., Zawada, L. P., "Fracture Behavior of an Oxide/Oxide Ceramic Matrix Composite" Submitted *J. Amer. Ceram. Soc.*
59. Zawada, L. P., "Longitudinal and Transthickness Tensile Behavior of Several Oxide/Oxide Composites", *Cer. Eng. Sci. Proc.*, Vol. 19, pp. 327-339 (1998).
60. Zuiker, J. R. "A Model for the Creep Response of Oxide-Oxide Ceramic Matrix Composites", Thermal and Mechanical Test Methods and Behavior of Continuous Fiber Ceramic Composites, ASTM STP 1309, pp. 250-263 (1997).
61. Pabst, R. F., Popp, G., "Critical and Subcritical Crack Extension in Al_2O_3 and SiC as Functions of Temperature, Environment, and Loading Rate" *Fracture Mechanics in Ceramics*, Vol. 5, pp. 305-316 (1977).
62. Dalgleish, B. J., Slamovich, E. B., Evans, A. G., "Duality in the Creep Rupture of a Polycrystalline Alumina," *J. Am. Ceram. Soc.*, Vol. 68, pp. 575-581 (1985).
63. Robertson, A. G., Wilkinson, D. S., Cáceres, C. H., "Creep and Creep Fracture in Hot Pressed Alumina," *J. Am. Ceram. Soc.*, Vol. 74, pp. 915-921 (1991).
64. Curtin, W. A., "In Situ Fiber Strengths in Ceramic-Matrix Composites from Fracture Mirrors," *J. Amer. Ceram. Soc.*, Vol. 77, pp. 1075-1078 (1994).
65. Goettler, R. W., McDermott Technologies, Inc., Private Communication.

66. Ishikawa, T., Chou, T.-W., "Stiffness and Strength Behavior of Woven Fabric Composites", *J. Mat. Sci.*, Vol. 17, pp. 3211-3220 (1982).

67. Knudsen, F. P., "Effect of porosity on Young's Modulus of Alumina" *J. Amer. Ceram. Soc.*, Vol. 45, pp. 94-95 (1962).

68. Eshelby, J. D., "The determination of the Elastic Field of an Ellipsoidal Inclusion, and Related Problems," *Proc. Roy. Soc. A*, Vol. 241, pp. 376-396 (1957).

69. Munro, R. G., "Evaluated Material Properties for a Sintered α-Alumina", *J. Am. Ceram. Soc.*, Vol. 80, pp. 1919-1928 (1997).

70. Crandall, W. B., Chung, D. H., Gray, T. J., "The Mechanical Properties of Ultra-Fine Hot-Pressed Alumina" in Kriegel, W. W., Palmour III, H., (Eds.) Mechanical Properties of Engineering Ceramics (1961).

71. DiCarlo, J. M., Yun, H. M., "Factors Controlling Stress Rupture of Fiber-Reinforced Cearmic Composites," *To Appear in* Environmental, Mechanical, and Thermal Properties of Continuous Fiber Ceramic Composite (CFCC) Materials and Components, ASTM STP 1392, (2000).

72. Goldsby, J. C., Yun, H. M., Morscher, G. N., DiCarlo, J. A. "Annealing Effects on Creep and Rupture of Polycrystalline Alumina-Based Fibers" NASA TM 1998-208841 (1998).

73. Nisitani, H., Chen, D. H. "Stress Intensity Factor for a Semi-Ellipti Surface Crack in a Shaft Under Tension," *Trans. Jap. Soc. Mech. Engrs.*, Vol. 453, pp. 1077-1082 (1984).

74. Sneddon, I.N., Lowengrub, M, *Crack Problems in the Theory of Elasticity*, New York, Wiley (1969).

75. Rice, J. W., "Microstructure Dependence of Mechanical Behavior of Ceramics", in Treatise on Materials Science and Technology, Vol. 11, MacCrone, R. K., (ed.), pp. 199-381 (1977).

76. Dorre, E., *Alumina: Processing, Properties, and Applications*, Berlin; New York, Springer-Verlag, (1984).

77. Pabst, R. F., "Determination of K_{Ic}-Factors with Diamond-Saw-Cuts in Ceramic Materials" *Fracture Mechanics of Ceramics*, Vol. 2, pp. 555-565 (1973).

78. Greg Morscher, Personal Communication.

79. Morscher, G. N., "Rupture of Woven Hi-Nicalon, Boron Nitride (BN), Silicon Carbide (SiC) Matrix Composites in Air" Paper 43, *HITEMP Review 1999* Vol. 2, NASA CP-1999-208915-2.

80. Kakisawa, H., Kagawa, Y., "A New Approach for Interface Sliding Shear Resistance in Al2O3 Fiber-Reinforced Al2O3 Matrix Composite," Ceramic Engineering and Science Proceedings, Vol. 20, pp. 435-443 (1999).

81. Kerans, R. J., Parthasarathy, T. A., "Theoretical Analysis of the Fiber Pullout and Pushout Tests," Journal of the American Ceramic Society, Volume 74, pp. 1585-1596 (1991).

82. Kotil, T., Holmes, J. W., Comninou, M., "Origin of Hysteresis Observed During Fatigue of Ceramic-Matrix Composites," *J. Am. Ceram. Soc.*, Vol. 73, pp. 1879-1883 (1990).

83. Reifsnider, K. L., "Critical Element Concepts for Residual Strength and Life Prediction", *Proc. Amer. Ceram. Soc.*, Vol. 6, pp. 387-403 (1986).

84. Halpin, J. C., Jerina, K. L., Johnson, T. A., "Characterization of Composites for the Purpose of Reliability Evaluation", *Analysis of Test Methods for High Modulus Fibers and Composites*, ASTM STP 521, pp. 5-64 (1973).

85. Curtin, W. A., "Fiber Pull-Out and Strain Localization in Ceramic Matrix Composites," Journal of the Mechanics and Physics of Solids, Volume 41, pp. 35-53 (1993).

Vita

Howard Gerhard Halverson

Howard Gerhard Halverson was born on September 7, 1971 to Howard and Evelyn Halverson in Danville, California. He grew up in State College, Pennsylvania, then moved to Berea, Kentucky. He graduated from Berea Community High School in 1989. He then attended Penn State, graduating in 1993 with a B.S. degree in Engineering Science. After graduation he attended the Virginia Polytechnic Institute and State University, taking a position as a graduate research assisstant. In 1996 he received an M.S. in Engineering Mechanics.